Scuola Dottorale di Ingegneria
Sezione di Ingegneria dell'Elettronica Biomedica,
dell'Elettromagnetismo e delle Telecomunicazioni

Design of Metamaterial-Inspired Electrically Small Active Radiating Elements

Progettazione di Elementi Radianti Attivi Elettricamente Corti
Ispirati ai Metamateriali

Fabrizio Trotta
(XXVII Ciclo della formazione Dottorale)

Docente-guida *Prof. Filiberto Bilotti*

This page is intentionally left blank.

Abstract

In this thesis, we present the a detailed description of the work and the results achieved on the research for the study of innovative active electromagnetic components and radiating microwave components metamaterial-inspired, which can be easily integrated in practically realizable systems for industrial application .

First, we analyze the use of non-Foster active circuits to obtain a widening of the operating bandwidth of devices based on metamaterials (MTMs); in particular we present study and realization of a demonstrator NIC (*Negative Impedance Converter*) compact, high integration and low cost, made of printed circuit with discrete components in SMD (*Surface Mount Technology*). The non-Foster circuit is designed by using only real components and the stability of the entire system is properly evaluated.

Then we explore the possibility to generate an electromagnetic field with a non-zero orbital angular momentum (OAM) using a single patch antenna. In particular, we report an analytical study of a circular patch antenna in order to show that a circular polarized TM_{nm} mode generates an OAM of order n-1. Then, we design an elliptical patch antenna that radiates a circular polarized electromagnetic field with OAM of the first order.

Third, we propose a new class of horn antennas with integrated MTM-inspired filtering modules. In particular, we present some horn antennas that, depending on the used resonant inclusion, show a band-pass or band-stop filtering and polarization transformer behavior.

Afterward, we present some radiating elements based on the use of MTM-inspired resonant inclusions. As an example, we propose a compact antenna for Wi-Fi application consisting of two orthogonal parasitic meandered monopoles and a driven bow-tie.

Finally, we show that properly designed mantle cloaks, consisting of patterned metallic sheets placed around cylindrical monopoles, allow tightly packing the same antennas together in a highly dense telecommunication platform. Our experimental demonstration is applied to the relevant example of two cylindrical monopole radiators operating for 3G and 4G mobile communications.

Acknowledgements

The completion of my dissertation has been a long journey in which many people have scientifically and humanly contributed. In the next few lines, I will try to thank all the people who supported me, without whose help I could not have made this journey.

I want to express my deeply-felt thanks to my supervisor, Prof. Filiberto Bilotti, Head of the Antennas & Special Materials Research Laboratory, who, starting from my B.S. degree, has always tried to bring me on the frontier of metamaterials science. I sincerely thank also Prof. Alessandro Toscano, Head of the Electromagnetic Diagnostic Laboratory, for his warm encouragement and thoughtful guidance during my research activities. They deserve my heartfelt gratitude for giving me the opportunity to enter the world of higher education and research, and for their valuable advice, constructive criticism and extensive discussions around my work.

My gratitude is also extended to all members of the Department of Engineering at "Roma Tre" University, for the excellent and pleasant working environment. I express my special thanks to my friends and colleagues Dr. Mirko Barbuto, Dr. Alessio Monti and Dr. Davide Ramaccia, with whom I have enjoyed many useful and entertaining moments.

I would like to thank Elettronica S.p.A for the use of their near-field measurement system and for support in measurements.

Last but not least, I want to reserve a special word of gratitude to my family, my wife Francesca and my fabulous sons Flavio and Alessio, who have brought great joy to my life. They deserve thanks for their love and a huge variety of other reasons.

Fabrizio Trotta
"Roma Tre" University
April 2016

This page is intentionally left blank.

Table of Contents

List of Figures

List of Tables

This page is intentionally left blank.

Esteso Sommario

(Italiano)

Il termime “metamateriale” (MTM) è nesso ad un esteso insieme di materiali sintetici, sintetizzati, introducendo ad esempio delle strutture metalliche di particolare forma e dimensione all’interno di un mezzo dielettrico ospitante [1]-[4]. I parametri costituzionali di tali inclusioni sono progettati per modificare la risposta del materiale ospitante ed ottenere proprietà inconsuete non riscontrabili nei materiali convenzionali alle frequenze di interesse. Benché alcuni materiali naturali mostrano su alcune bande di frequenza dello spettro elettromagnetico (infrarosso, visibile e ultravioletto [5]-[6]), valori anomali negativi o nulli della permittività elettrica, alle frequenze delle microonde non sono noti in natura materiali con caratteristiche simili. Anche le proprietà magnetiche dei materiali naturali sono limitate alle frequenze radio ed alle basse microonde [7] e valori anomali di permeabilità magnetica non sono naturalmente disponibili nel dominio visibile, infrarosso e ultravioletto. Tuttavia, quando la natura non ci fornisce i valori necessari dei parametri elettromagnetici, i MTM possono essere utilizzati con successo per ottenere i valori anomali desiderati.

Ad esempio, come anticipato teoricamente in [8] e dimostrato sperimentalmente in [9], è possibile ottenere un MTM caratterizzato da un indice di rifrazione negativo alle frequenze delle microonde combinando opportunamente sottili fili metallici [10] e split-ring resonator (SRR). Infatti, poiché in tale materiale le inclusioni e la distanza tra di esse sono inferiori rispetto alla lunghezza d’onda operativa, è possibile introdurre valori efficaci di permettività, permeabilità e indice di rifrazione, i quali possono assumere valori anomali. La loro sintesi prende spunto dall’idea introdotta da Pendry [9], secondo la quale una serie di dipoli elettrici orientati causa un comportamento risonante della permittività elettrica efficace del mezzo. In modo simile, un insieme di dipoli magnetici genera un’analoga risonanza della permeabilità magnetica efficace associata al MTM. Se le due risonanze si verificano nello stesso intervallo di frequenze, siamo in grado di sintetizzare un materiale con un indice di rifrazione negativo in un determinato intervallo di frequenze.

L'elemento fondamentale per la realizzazione del primo MTM è stato quindi lo SRR, il quale è un risonatore miniaturizzato utile per ottenere il magnetismo artificiale alle frequenze delle microonde. Un singolo SRR è costituito da due anelli aperti concentrici di materiale metallico, le cui aperture sono poste a lati opposti della struttura. Tale configurazione permette di aumentare la capacità totale del risonatore rispetto a quella di una struttura a singolo anello, aggiungendo una capacità distribuita tra i due anelli concentrici. In questo modo, la frequenza di risonanza del risonatore può essere significativamente ridotta per raggiungere una dimensione elettrica dell'ordine di $\lambda/10$. Dopo quanto proposto in [9], sono state introdotte molte inclusioni magnetiche differenti per ottenere un maggiore grado di miniaturizzazione, rimuovere la bi-anisotropia intrinseca che caratterizza il comportamento di uno SRR [11]-[14], e ottenere una risposta isotropa [15]-[18].

Accanto a questi sforzi modellistici, sono state investigate molte proprietà innovative dei MTM. In particolare, l'effetto di super-risoluzione di un MTM con indice di rifrazione negativo ha mostrato come sia possibile superare il limite fisico della diffrazione. Una lente convenzionale, infatti, è in grado di focalizzare un dettaglio con un limite ben noto in ottica: fissata la frequenza operativa, tale dettaglio non può essere inferiore alla corrispondente lunghezza d'onda di lavoro. Una lamina opportunamente progettata di MTM può invece andare idealmente al di sotto del limite fisico della diffrazione, focalizzando dettagli con dimensioni inferiori alla lunghezza d'onda. Altre applicazioni interessanti dei MTM derivano dall'idea che, se utilizziamo insieme una coppia di materiali artificiali coniugati, possiamo progettare cavità risonanti di dimensioni trasversali molto inferiori alla lunghezza d'onda. A partire da questa idea di base, sono stati proposti numerosi componenti e dispositivi innovativi basati sulle propietà dei MTM, come ad esempio super-lenti [19]-[20], iper-lenti [21], rivestimenti per l'invisibilità elettromagentica [22]-[24], componenti radianti compatti [25]-[29], dispositivi per l'aumento della trasmissione da foro elettricamente piccolo [30]-[36], filtri [37], assorbitori [38], ecc. Inoltre, negli ultimi anni, sfruttando le potenzialità offerte dalla nano-fabricazione, il range operativo in frequenza dei MTM è stato esteso fino alle frequenze ottiche [39]-[43]. In questo caso, tuttavia, i risonatori magnetici usati alle microonde non possono essere facilmente impiegati [44] e, di conseguenza, sono stati introdotti design alternativi con un minore grado di miniaturizzazione [45]-[46], o basati su approcci concettualmente differenti [47]-[48].

Tuttavia, qualunque sia la gamma di frequenze di interesse, i materiali magnetici artificiali o più in generale i MTM presentano alcune limitazioni intrinseche. A causa di considerazioni energetiche, infatti, ogni MTM passivo deve essere necessariamente un mezzo dispersivo [49]. I valori desiderati dei parametri elettromagnetici sono quindi ottenuti soltanto in un ristretto intervallo di frequenze e, di conseguenza, la banda operativa dei componenti basati su MTM è tipicamente a sua volta limitata. Inoltre, come risulta chiaro dalle relazioni di causalità di Kramers-Kronig, il fenomeno di dispersione è sempre legato a meccanismi di perdita [49], i quali riducono ulteriormente le potenzialità dei MTM.

Per ovviare all'inconveniente della limitazione in banda, alcuni lavori allo stato dell'arte hanno suggerito che, nella costruzione della cella elementare costituente il MTM, sia inserito un elemento attivo che possa aumentare la banda, compensando i fenomeni di risonanza associati al MTM. Questo può essere realizzato abbastanza facilmente nel dominio delle frequenze RF mentre è assai difficile per frequenze più alte.

Nella tecnica dei sistemi riceventi, la tecnologia *non-Foster Matching* ha la capacità di raggiungere maggiori larghezze di banda istantanea e/o adattamento d'impedenza mediante l'utilizzo di dispositivi *Negative Impedance Converter* (NIC). Quest'ultimi sono particolari dispositivi attivi elettronici in grado di comportarsi come carichi negativi che iniettano energia nei circuiti, a differenza dei carichi ordinari che la dissipano.

Il vantaggio ottenibile utilizzando la tecnologia non-Foster congiunta a quella *metamaterial-based* sull'elemento radiante, può allo stato dell'arte svolgere un ruolo strategico fondamentale nella ricerca della soluzione più adatta, innovativa e prestazionale nel campo della progettazione di dispositivi radianti attivi a larga banda ispirati ai MTM.

Il **Capitolo 1** di questa tesi è, quindi, dedicato all'impiego di elementi attivi NIC per applicazioni *Non-Foster impedance Matching* su *Electrically small metamaterial-based* *antennas* per applicazioni UWB in banda VHF/UHF. Innanzitutto, partendo da una breve descrizione teorica della tecnologia Non-Foster, determineremo la tipologia circuitale del carico attivo richiesta per compensare la reattanza intrinseca dell’elemento elettricamente corto ed ottenere un adattamento di impedenza a banda larga mediante un dispositivo NIC. Verrà poi presentato il lavoro di scouting tecnologico che, associato all’analisi di alcuni lavori sperimentali, ci consentirà di individuare la soluzione circuitale e tecnologica prescelta per il progetto del NIC a componenti discreti. E’ stata quindi riportata la ricerca sulla componentistica attiva e passiva necessaria all'implementazione della soluzione circuitale prescelta. In particolare, partendo dai DS forniti dai principali fornitori, sono stati individuati i componenti passivi e attivi a basso costo disponibili sul mercato per applicazioni di tipo civile. Con il simulatore circuitale ADS è stata compiuta un’analisi qualitativa delle componenti circuitali parassitiche dei elementi attivi; l’analisi ha permesso di definire lo schema elettrico del NIC con i valori nominali dei componenti SMD selezionati. Lo schema è stato successivamente implementato nel modello circuitale sul simulatore ADS e tramite questo sono state effettuate le simulazioni per la verifica di fattibilità del dispositivo. Per un’analisi quantitativa delle componenti circuitali parassitiche è stato realizzato un modello 3D mediante il simulatore CST MWS.

Il Capitolo 2 di questa tesi sarà invece dedicato ad una particolare manipolazione che può essere eseguita su un segnale elettromagnetico ovvero la generazione del momento angolare orbitale (OAM). In particolare, la recente estensione del concetto di OAM dalle frequenze ottiche a quelle delle microonde ha portato alcuni ricercatori ad esplorare come le tecniche radiative a microonde possano essere utilizzate per irradiare un campo elettromagnetico con OAM non nullo. A tal riguardo, il lavoro svolto mira a presentare un nuovo approccio per generare un campo con OAM non nullo attraverso l’utilizzo di una singola antenna a patch. Utilizzando il modello a cavità, per prima cosa analizzeremo il campo irradiato da un patch circolare standard e mostreremo che un modo TM_{nm} a polarizzazione circolare eccitato mediante due cavi coassiali è in grado di generare un campo elettromagnetico con OAM di ordine $\pm(n-1)$. Successivamente, al fine di ottenere una struttura più semplice con un singolo feed, progetteremo un’antenna a patch ellittico in grado di irradiare un modo TM_{21} a polarizzazione circolare destra. Utilizzando simulazioni full-wave ed esperimenti su un prototipo fabbricato, mostreremo che l’antenna proposta è in grado di irradiare efficacemente un campo elettromagnetico con un OAM del primo ordine.

Nel **Capitolo 3**, focalizzeremo invece la nostra attenzione sul progetto di antenne ad horn con moduli filtranti integrati ispirati ai MTM. A tale scopo, proporremo l’utilizzo di un trasformatore di polarizzazione realizzato mediante una struttura laminare integrata in guida d’onda. La lamina metallica circolare realizza un trasformatore di polarizzazione costituito da un risonatore complementare elettricamente piccolo intagliato su uno schermo metallico. Mostreremo prima che tale componente è in grado di trasformare la polarizzazione lineare di una guida d’onda rettangolare operante nel suo modo fondamentale in una circolare. Successivamente, integrando tale convertitore di polarizzazione in un horn conico, mostreremo come sia possibile ottenere un’antenna ad horn filtrante in polarizzazione circolare. Il comportamento della struttura proposta sarà validato tramite simulazioni numeriche e misurazioni effettuate su un prototipo.

Si noti, tuttavia, che tale approccio prevede l’inserimento di uno schermo metallico ortogonale alla direzione di propagazione del campo elettromagnetico; di conseguenza, esso può essere utilizzato soltanto per componenti a microonde che debbano mostrare un comportamento di tipo passa-banda. Al fine di progettare antenne ad horn filtranti o componenti a microonde con una carratteristica di tipo notch (elimina banda), dobbiamo quindi rimuovere lo schermo metallico e progettare un’inclusione risonante che sia in grado di immagazzinare/dissipare energia ad una data frequenza, ottenendo così una banda proibita in uno stretto intervallo di frequenze. A tale scopo, presenteremo quindi il progetto di antenne ad horn filtranti con un comportamento elemina banda ottenuto attraverso l’utilizzo di risonatori magnetici elettricamente piccoli. In particolare, uno SRR realizzato su un substrato dielettrico Rogers Duroid$^{\text{TM}}$ RT5870 sarà inserito all’interno di un’antenna ad horn ad una opportuna distanza dalla sua apertura. Intorno alla frequenza di risonanza dello SRR la trasmissione sarà quindi fortemente ridotta ottenendo così un comportamento di tipo notch. Al fine di estendere tale risultato al caso di operatività dual-band, proporremo inoltre il progetto di un modulo filtrante costituito da due SRR con dimensioni differenti. Anche in questo caso, la validità dell’approccio proposto sarà verificata attraverso un opportuno set di simulazioni full-wave e esperimenti condotti su prototipi.

Il Capitolo 4 di questa tesi sarà invece dedicato al progetto di nuovi elementi radianti compatti e multifunzione ispirati ai concetti dei MTM. Presenteremo un’antenna compatta costituita da due monopoli a meandro ortogonali che agiscono come elementi parassiti di un bow-tie alimentato. In particolare, mostreremo che utilizzando due monopoli con dimensioni leggermente differenti è possibile ottenere una maggiore larghezza di banda di impedenza. Utilizzando tale approccio, presenteremo un’antenna compatta operante nella banda del Wi-Fi a 2.4 GHz con dimensioni elettriche complessive pari a $\lambda_0/6\times\lambda_0/12\times\lambda_0/75$.

Infine nel **Capitolo 5** mostreremo come sia possibile progettare e realizzare, con delle semplici lastre metalliche, mantelli cilindrici su dei monopoli cilindrici in grado di rendere invisibili i monopoli alla radiazione elettromagnetica su piattaforme di telecomunicazioni ad alta densità (tipo stazioni di antenne per cellulari o sulle navi). In queste applicazioni molte antenne operano a breve distanza, diminuendo l’efficienza dell’insieme. Avvolgendo queste antenne con il meta-materiale, si possono isolare EM diventano invisibili una all’altra. In questo modo è stato possibile rendere invisibile un’antenna a banda limitata a vantaggio di un’altra antenna che opera su differenti frequenze. La dimostrazione sperimentale verrà applicata all'esempio pertinente di due radiatori monopoli cilindrici operativi per comunicazioni mobili su standard 3G e 4G

Introduction

The term “metamaterial” (MTM) refers to the wide range of artificially engineered materials, typically synthesized by arranging conductive structures of particular shape and size in a host dielectric medium [1]-[4]. The electromagnetic parameters and geometry of such inclusions are designed to change the response of the host material and obtain special properties that are not achievable by conventional materials at the frequencies of interest. Just to cite an example, though some natural materials (e.g. noble metals and some semiconductors) exhibit unconventional values (i.e. negative or near zero) of the electric permittivity at IR, visible, and UV frequencies [5]-[6], a natural material with similar characteristics in the microwave regime was not known. In the same way, magnetism of natural materials is limited to radio and low-microwave frequencies [7] and, consequently, anomalous permeability values are not naturally available in the IR, visible, and UV domains. When nature does not provide us with the needed values of the material parameters, MTMs can be successfully used to obtain such anomalous values.

For instance, as anticipated in [8] and experimentally demonstrated in [9], it is possible to obtain a MTM characterized by a negative index of refraction at microwave frequencies combining metal thin wires [10] and split-ring resonators (SRRs). In fact, since in such material the inclusions and the distance between them are reduced in size when compared with the operating wavelength, it is possible to introduce effective permittivity, permeability and refractive index of the medium, which can assume anomalous values. Its synthesis starts from the idea introduced by Pendry [9], that a series of electric dipoles properly oriented causes a resonant behavior for the effective electrical permittivity of the medium. Similarly, a set of magnetic dipoles causes a similar resonance of the effective magnetic permeability associated with the MTM. If the two resonances occur at the same frequency range, we are able to synthesize a material with negative refractive index in a specific frequency range.

The key element to the realization of the first MTM was then the SRR, which is a miniaturized resonator useful to obtain artificial magnetism at microwave frequencies. A single SRR consists of two concentric metallic broken rings with the two gaps placed at the opposite sides of the structure. This ingenious design permits to increase the overall capacitance of the resonator with respect to a single ring structure, by adding a distributed capacitance between the two concentric rings. In this way, the resonant frequency can be significantly lowered to reach an electrical size of the order of $\lambda/10$. After the work [9], several different magnetic inclusions have been introduced to achieve a higher degree of miniaturization, remove the inherent bi-anisotropy characterizing the electromagnetic behavior of the SRR [11]-[14], and obtain an isotropic response [15]-[18].

Besides these modeling efforts, several innovative properties of MTMs have been investigated. In particular, the effect of super-resolution of a MTM with a negative index of refraction has shown how one can overcome the physical limit of diffraction. A conventional lens, in fact, is able to focus on a detail with a well-known limit in optics:

fixed the working frequency, this detail can not be less than the corresponding operating wavelength. A flat plate of properly designed MTM can instead ideally go below the physical limit of diffraction, focusing details with dimensions smaller than the wavelength. Other interesting applications of MTMs result from the idea that, if we couple together a pairs of conjugated artificial materials, we can design resonant cavities of transverse dimensions much smaller than the wavelength. Starting from these ideas, several innovative components and devices based on MTMs properties have been proposed, such as super-lenses [19]-[20], hyper-lenses [21], cloaking covers [22]-[24], compact radiating components [25]-[29], enhanced transmission devices [30]-[36], filters [37], absorbers [38], etc. Moreover, in the last years, exploiting the potentials offered by nano-fabrication, the operation frequency range of MTMs has been extended up to optical frequencies [39]-[43]. In this case, however, the magnetic resonators used at microwave frequencies cannot be straightforwardly applied [44], and alternative designs with a lower rate of miniaturization [45]-[46], or based on conceptually different approaches [47]-[48] have been introduced.

Whatever the frequency range of interest is, however, artificial magnetic materials exhibit some intrinsic limitations. Due to energy considerations, in fact, any passive MTM is necessarily a dispersive medium [49], meaning that the desired values of the electromagnetic parameters are typically reached only in a narrow frequency range and, consequently, the operation bandwidth of MTM-based components is limited. Moreover, as it is clear from Kramers-Kronig causality relationships, the dispersion phenomenon is always related to loss mechanisms [49] that further reduce the potentials of the designed MTMs.

To get around this problem, some state of art works have suggested that, in the unit cell constituting the MTM, is inserted an active element that can increase the bandwidth, offsetting the resonance phenomena associated with MTM. This can be easily realized in the domain of RF frequencies band, while it is very difficult for higher frequencies

In the technique of receiving systems, the non-Foster Matching technology has the ability to achieve higher instantaneous bandwidths and / or impedance matching using *Negative Impedance Converter* (NIC) *devices*. NIC are particular active electronic devices able to behave as negative loads that inject energy in the circuits, unlike ordinary loads that dissipate.

The advantage achieved by using the non-Foster technology with that metamaterial-based radiating element, can play a key strategic role in the search for the most innovative and high-performance solution in the design of wideband active radiating element devices MTM-inspired.

Chapter 1 of this thesis is, thus, dedicated to the investigation on the use NIC active element for *Non-Foster impedance UWB Matching of Electrically small metamaterial-based antenna* application (VHF/UHF band). First, we starting from a short theoretical description of non-Foster technology and we will determine the type of the active load required to compensate the reactance (capacitive) of electrically small radiating element, with the aim of obtaining a broadband impedance matching by means of a NIC device. We will present the work of NIC technology scouting, associated to the analysis of some experimental works, which will allow us to identify the circuit and technology solution for the discrete components NIC project. It 'was then reported research on active and passive circuit components necessary to the implementation of the chosen solution. In particular, starting from Datasheet provided by the suppliers, the passive and active low cost components have identified. Through the ADS circuit simulators, we performed a qualitative parasitic components elements analysis of the active circuit; the analysis allowed defining NIC circuit diagram solution with the nominal values of the selected SMD components. The circuit diagram has been implemented in ADS model and simulations carried out to verify the device feasibility. For a quantitative analysis of circuit components parasites, a full wave 3D model with CST MWS simulator has been created.

Chapter 2 of this thesis will be instead to another possible manipulation that may be performed on an electromagnetic signal is the generation of orbital angular momentum (OAM). In particular, the recent extension of the OAM concept from optical to microwave frequencies has led some researchers to explore how well established antenna techniques can be used to radiate a non-zero OAM electromagnetic field. In this frame, this chapter is aimed to present a new approach to generate a non-zero OAM field through a single patch antenna. Using the cavity model, we first analyze the radiated field by a standard circular patch and show that a circular polarized (CP) TM_{nm} mode excited by using two coaxial cables generates an electromagnetic field with an OAM of order ±(n-1). Then, in order to obtain a simpler structure with a single feed, we design an elliptical patch antenna working on the right-handed CP TM_{21} mode. Using full-wave simulations and experiments on a fabricated prototype, we show that the proposed antenna effectively radiates an electromagnetic field with a first order OAM. Such results prove that properly designed patch antennas can be used as compact and low-cost generators of electromagnetic fields carrying OAM.

In **Chapter 3**, we focus our attention on the design of horn antennas with integrated MTM-inspired filtering module. We propose the use of a polarization transformer achieved through integrated laminar structure in the waveguide. The circular metal foil, realizes a polarization transformer constituted by an electrically small complementary resonator impressed on a metal screen. We will show that this first component is able to transform the linear polarization of a rectangular waveguide (operating in its fundamental mode) in a circular polarization. Then, integrating this polarization transformer in a conical horn, we show how it is possible to obtain a circularly polarized filtering horn antenna (horn filtenna). However, this setup is not planar, consists of different and geometrically orthogonal structures, involves the use of dielectric materials leading to an efficiency reduction, and can handle only low-power signals (i.e. the operation is limited to the receiving mode only). In order to overcome these issues, we then propose a new linear-to-circular polarization transformer that consists of a complementary electrically small resonator etched on a metallic screen. We first show that this component is able to transform the linear polarization of a regular rectangular waveguide working on the fundamental mode into a circular one. Then, integrating this polarization transformer in a conical horn, we show how it is possible to obtain a filtering horn antenna working for circularly polarized signals. The numerical simulations and the measurements performed on a prototype prove the effectiveness of the proposed structure.

Please note, however, that this approach involves the insertion of a metallic screen orthogonal to the propagation direction of the electromagnetic field; therefore, it can be used only for microwave components exhibiting a band-pass behavior. In order to design horn filtennas or microwave components with band-stop characteristic, thus, we need to remove the metallic screen and design a proper resonant inclusion that stores/dissipates energy at a given frequency, leading to a band-notch in a narrow frequency range. For this purpose, we then present the design of filtering horn antennas with band-stop characteristics obtained through the use of electrically small magnetic resonators. In particular, a SRR etched on a Rogers Duroid^{TM} RT5870 dielectric substrate is inserted within the metallic flare of the horn at a proper distance from the throat. At around the resonant frequency of the SRR transmission is highly reduced and a single notched-band is obtained. In order to extend the result to dual-band operation, we also present the design of the filtering module made by two SRRs with different dimensions. The validity of the proposed approach is verified through proper sets of full-wave simulations and experiments on fabricated prototypes.

Chapter 4 of this thesis will be dedicated to the project of new compact radiating elements and multifunction inspired by the concepts of the MTM. We will present a compact antenna consisting of two orthogonal meandered monopoles that act as parasitic elements of a driven bow-tie. In particular, we show that by using two monopoles with slightly different dimensions, a greater impedance bandwidth can be obtained. Using this approach, we present a compact antenna operating in the 2.4 GHz Wi-Fi band with overall dimensions of $\lambda_0/6\times\lambda_0/12\times\lambda_0/75$.

Finally, in **Chapter 5** show how it is possible to design and implement, with the simple metal plates, cylindrical mantle on cylindrical monopoles able to make invisible the monopoles to electromagnetic radiation (on telecommunications stations platforms with high density antennas for mobile devices or on ships)

For these applications, many antennas operate at a short distance, decreasing the efficiency of the radiating element. Load the external surface of these antennas with the MTM cover, it is possible to isolate each other. In this way it was possible to make invisible one antenna to the benefit of another antenna that operates on different frequencies. The experimental demonstration will be applied to the example of two cylindrical monopole antennas for mobile communications on 3G and 4G standards

References

[1] G.V. Eleftheriades, and K.G. Balmain, *Negative Refraction Metamaterials: Fundamental Principles and Applications*. Hoboken, NJ: Wiley-IEEE Press, 2005.

[2] N. Engheta, and R.W. Ziolkowski, *Electromagnetic Metamaterials: Physics and Engineering Explorations*. Hoboken, NJ: Wiley-IEEE Press, 2006.

[3] R. Marqués, F. Martín, M. Sorolla, and F. Capolino, *Metamaterials with Negative Parameters: Theory, Design and Microwave Applications*. Hoboken, NJ: Wiley-Interscience, 2008.

[4] S. Zouhdi, A. Sihvola, and A. P. Vinogradov, *Metamaterials and Plasmonics: Fundamentals, Modelling, Applications*. Dordrecht, NL: Springer-Verlag GmbH, 2008.

[5] P.B. Johnson, R. W. Christy, “Optical constants of the noble metals,” *Phys. Rev. B*, Vol. 6, pp. 4370-4379, 1972.

[6] E.D. Palik, *Handbook of Optical Constants of Solids*, Boston, NE: Academic Press, 1998.

[7] L.D. Landau, L.P. Pitaevskii, and E.M. Lifshitz, *Electrodynamics of Continuous Media, Second Edition*: Volume 8. Oxford, EN: Pergamon Press, 1984.

[8] V.G. Veselago, “The electrodynamics of substances with simultaneously negative values of ε and μ,”, *Sov. Phys. Uspekhi*, Vol. 10, pp. 509–514, 1968.

[9] D.R. Smith, W.J. Padilla, D.C. Vier, S.C. Nemat-Nasser, and S. Schultz, “Composite medium with simultaneously negative permeability and permittivity,” *Phys. Rev. Lett.*, Vol. 84, pp. 4184-4187, 2000.

[10] W. Rotman, “Plasma simulation by artificial dielectrics and parallel-plate media,” *IRE Trans. Antennas Propagat.*, Vol. 10, pp. 82-25, 1962.

[11] R. Marqués, F. Medinaand, and R. Rafii-El-Idrissi, “Role of bi-anisotropy in negative permeability and left handed metamaterials,” *Phys. Rev. B*, Vol. 65, 144441, 2002.

[12] R. Marqués, F. Mesa, J. Martel, and F. Medina, “Comparative analysis of edge and broadside coupled split ring resonators for metamaterial design. Theory and experiment,” *IEEE Trans. Antennas Propagat.*, Vol. 51, pp. 2572–2581, 2003.

[13] R. Marqués, J. D. Baena, J. Martel, F. Medina, F. Falcone, M. Sorolla, and F. Martin, “Novel small resonant electromagnetic particles for metamaterial and filter design,” *Proc. ICEAA’03*, pp. 439–442, Torino, Italy, 2003.

[14] J. D. Baena. R. Marqués, F. Medina, and J. Martel, “Artificial magnetic metamaterial design by using spiral resonators,” *Phys. Rev. B*, Vol. 69, 014402, 2004.

[15] Ph. Gay-Balmaz, and O. J. F. Martin, “Efficient isotropic magnetic resonator,” *Appl. Phys. Lett.*, Vol. 81, pp. 939–941, 2002.

[16] C. R. Simovski, and B. Sauviac, “Towards creating isotropic microwave composites with negative refraction,” *Radio Sci.*, Vol. 39, RS2014, 2004.

[17] C. R. Simovski, and S. He, “Frequency range and explicit expressions for negative permittivity and permeability for an isotropic medium formed by a lattice of perfectly conducting Ω particles,” *Phys. Lett. A*, Vol. 311, pp. 254–263, 2003.

[18] M.M. I. Saadoun, and N. Engheta “A reciprocal phase shifter using a novel pseudochiral or Ω medium,” *Microwave Opt. Tech. Lett.*, Vol. 5, pp. 184–188, April 1992.

[19] J.B. Pendry, “Negative refraction makes a perfect lens,” *Phys. Rev. Lett.*, Vol. 85, pp. 3966-3969, 2000.

[20] P. Belov, R. Marques, S. Maslovski, I. Nefedov, M. Silverinha, C. Simovski, and S. Tretyakov, “Experimental study of the subwavelength imaging by a wire medium slab,” *Phys. Rev. B*, Vol. 67, 113103, 2003.

[21] W. Zhang, H. Chen, and H.O. Moser, “Subwavelength imaging in a cylindrical hyperlens based on S-string resonators,” *Appl. Phys. Lett.*, Vol. 98, 073501, 2011.

[22] A. Alù and N. Engheta, “Achieving transparency with plasmonic and metamaterial coatings,” *Phys. Rev. E*, Vol. 72, 016623, 2005.

[23] M. G. Silveirinha, A. Alu, and N. Engheta, “Parallel-plate metamaterials for cloaking structures,” *Phys. Rev. E*, Vol. 75, 036603, 2007.

[24] B. Edwards, A. Alu, M. Silveirinha, and N. Engheta, “Experimental verification of plasmonic cloaking at microwave frequencies with metamaterials,” *Phys. Rev. Lett.*, Vol. 103, 153901, 2009.

[25] R.W. Ziolkowski and A.D. Kipple, “Application of double negative materials to increase the power radiated by electrically small antennas,” *IEEE Trans. Antennas Propagat.*, Vol. 52, pp. 2626-2640, 2003.

[26] F. Qureshi, M.A. Antoniades, and G. V. Eleftheriades, “A compact and low-profile metamaterial ring antenna with vertical polarization,” *IEEE Antennas Wireless Propag. Lett.*, Vol. 4, pp. 333-336, 2005.

[27] A. Alù, F. Bilotti, N. Engheta, and L. Vegni, “Sub-wavelength planar leaky-wave components with metamaterial bilayers,” *IEEE Trans. Antennas Propagat.*, Vol. 55, pp. 882-891, 2007.

[28] A. Alù, F. Bilotti, N. Engheta, and L. Vegni, “Subwavelength, Compact, Resonant Patch Antennas Loaded With Metamaterials,” *IEEE Trans. Antennas Propagat.*, Vol. 55, pp. 13-15, 2007.

[29] F. Bilotti, A. Alù, and L. Vegni, “Design of miniaturized metamaterial patch antennas with μ-negative loading,” *IEEE Trans. Antennas Propagat.*, Vol. 56, pp. 1640-1647, 2008.

[30] D. E. Grupp, H. J. Lezec, T. Thio, and T. W. Ebbesen, “Beyond the Bethe limit: tunable enhanced light transmission through a single sub-wavelength aperture,” *Adv. Mat.*, Vol. 11, pp. 860–862, 1999.

[31] A. Alù, F. Bilotti, N. Engheta, and L. Vegni, “Metamaterial covers over a small aperture,” *IEEE Trans. Antennas Propagat.*, Vol. 54, pp. 1632-1643, 2006.

[32] A. Alù, F. Bilotti, N. Engheta, and L. Vegni, "A review on the potential use of metamaterial layers for increasing the transmission through a single sub-wavelength aperture in a flat opaque screen," in *Periodic Structures*, ed. by M. Bozzi and L. Perregrini, Kerala, India, 2006, ch. 10, pp. 271-291.

[33] F. Bilotti, L. Scorrano, E. Ozbay, and L. Vegni, "Enhanced transmission through a sub-wavelength aperture: Resonant approaches employing metamaterials," *J. Opt. A*, Vol.11, 114029, 2009

[34] K. Aydin, A.O. Cakmak, L. Sahin, Z. Li, F. Bilotti, L. Vegni, and E. Ozbay, "Split-ring-resonator-coupled enhanced transmission through a single subwavelength aperture," *Phys. Rev. Lett.*, Vol. 102, pp. 013904, 2009.

[35] K.B. Alici, F. Bilotti, L. Vegni, and E. Ozbay, "Optimization and tunability of deep subwavelength resonators for metamaterial applications: complete enhanced transmission through a subwavelength aperture," *Opt. Expr.*, Vol. 17, pp. 5933-5943, 2009.

[36] A.O. Cakmak, K. Aydin, E. Colak, Z. Li, F. Bilotti, L. Vegni, and E. Ozbay, "Enhanced transmission through a sub-wavelength aperture using metamaterials," *Appl. Phys. Lett.*, Vol. 95, 052103, 2009.

[37] J. Martel, R. Marques, F. Falcone, J.D. Baena, F. Medina, F. Martin, and M. Sorolla, "A new LC series element for compact bandpass filter design," *IEEE Microwave Wireless Compon. Lett.*, Vol. 14, pp. 210-212, 2004.

[38] F. Bilotti, L. Nucci, and L. Vegni, "An SRR based microwave absorber," *Microw. Opt. Technol. Lett.*, Vol. 48, pp. 2171-2175, 2006.

[39] N. Fang, H. Lee, C. Sun, and X. Zhang, "Sub–diffraction-limited optical imaging with a silver superlens," *Sci.*, Vol. 308, pp. 534-537, 2005.

[40] A. Salandrino, and N. Engheta, "Far-field subdiffraction optical microscopy using metamaterial crystals: Theory and simulations," *Phys. Rev. B*, Vol. 74, 075103, 2006.

[41] Z. Liu, H. Lee, Y. Xiong, C. Sun, and X. Zhang, "Far-field optical hyperlens magnify-ing sub-diffraction-limited objects," *Sci.*, Vol. 315, pp. 1686, 2007.

[42] M. Silveirinha, A. Alu and N. Engheta, "Infrared and optical invisibility cloak with plasmonic implants based on scattering cancellation," *Phys. Rev. B*, 78, 075107, 2008.

[43] N. Engheta, "Circuits with light at nanoscales: Optical nanocircuits inspired by metamaterials," *Sci.*, Vol. 317, pp. 1698-1702, 2007.

[44] J. Zhou, T. Koschny, M. Kafesaki, E.N. Economou, J.B. Pendry, and C.M. Soukoulis, "Saturation of the magnetic response of split-ring resonators at optical frequencies," *Phys. Rev. Lett.*, Vol. 95, 223902, 2005.

[45] G. Dolling, C. Enkrich, M. Wegener, J. F. Zhou, C. M. Soukoulis, and S. Linden, "Cut-wire pairs and plate pairs as magnetic atoms for optical metamaterials," *Opt. Expr.*, Vol. 30, pp. 3198-3200, 2005.

[46] M. Kafesaki, I. Tsiapa, N. Katsarakis, Th. Koschny, C. M. Soukoulis, and E. N. Economou, “Left-handed metamaterials: The fishnet structure and its variations,” *Phys. Rev. B*, Vol. 75, 235114, 2007.

[47] A.N. Grigorenko, A.K. Geim, H.F. Gleeson, Y. Zhang, A.A. Firsov, I.Y. Khrushchev, J. Petrovic, “Nanofabricated media with negative permeability at visible frequencies,” *Nat.*, Vol. 438, pp. 335-338, 2005.

[48] A. Alù, and N. Engheta, “The quest for magnetic plasmons at optical frequencies,” *Opt. Expr.*, Vol. 17, pp. 5723-5730, 2009.

[49] S.A. Tretyakov, and S.I. Maslovski, “Veselago materials: What is possible and impossible about the dispersion of the constitutive parameters,” *IEEE Antennas Propag. Mag.*, Vol. 49, pp. 37-43, 2007.

Chapter 1

Non-Foster actively NIC loaded for electrically-small metamaterial based-antennas

As shown in [1], it is in principle possible to widen the operation bandwidth of a passive MTM by loading it with an active circuit. In particular, in [1] a short dipole (or a small loop) antenna loaded with an ideal two-port electronic circuit has been considered and it has been shown that, in order to get negative and frequency-independent values of the permittivity (or permeability), it is necessary to use a negative capacitance (or inductance). In [1] it has been also suggested that this kind of reactive elements can be obtained using negative impedance converters (NICs), i.e. two-port devices exhibiting at the input port an impedance that is the opposite of the load one [2].

This class of active circuits, violating Foster's theorem [3], has been introduced in the last century to compensate resistive losses [4] and their first transistor-based implementations are due to Linvill [5]. Recently, due to their unique and interesting properties, NIC circuits have been extensively applied to widen the operational bandwidth of electromagnetic components. For instance, as far as antennas are concerned, NICs have been used to design active external matching networks for both microstrip [6] and electrically small dipole/monopole/loop antennas [7]-[9] able to overcome Bode-Fano criterion, while a different conceptual approach, based on internal non-Foster matching circuits, has been proposed in [10]-[11]. Moreover, NICs have been used to synthesize ultra-wideband artificial magnetic conductors (AMCs) and electromagnetic band gap structures [12] and superluminal waveguides for broadband leaky-wave antennas [13]-[14].

In the last few years, some groups have focused their efforts to investigate the possibility of using NICs to overcome the limitations of passive MTMs. In particular, non-Foster elements have been used to increase the bandwidth of several types of broadband and electrically small MTM-inspired antennas [15]-[18] and to obtain an almost dispersionless epsilon-near-zero MTM, useful for cloaking applications [19]-[20]. Finally, in [21] an active broadband effective MTM has been proposed.

It is important to observe that, despite the potentials of such NIC circuits, their practical use is still limited, due to the fact that the design and the proper use of a NIC is not a trivial task. One of the main issues concerns the theoretical evaluation of the NIC stability and the related technological aspects. As clarified in [22], where several circuits including negative lumped elements have been investigated, in fact, the correct evaluation of the stability depends also on the used evaluation approach and the uncritical use of classical stability methods may result in assessment mistakes.

In this Chapter, inspired by the aforementioned papers, we propose to load an electrically-small antennas with a proper NIC-based active circuit, in order to increase its operation bandwidth and make it useful for the application in broadband MTM-inspired components. In order to show the potentials of the proposed broadband matching , we analyze the performance improvement of the SRR-based antenna presented in [23], suitably scaled to work within the RF band, where NIC implementation is not critical by using discrete circuit elements. The main result obtained, was to show that the operating band of the active devices of adaptation, based on non-Foster networks, can be increased considerably through the use of an appropriate NIC circuit, with discrete components on a single layer SMD technology. The Chapter is organized as follows: in Section 1, we introduce the general consideration of frequency band chosen for the project, advantage achieved by using the technology non-Foster matching for UWB applications where the radiating element can be electrically short; in Section 2, we describe a non-Foster technology and in Section 3, we introduce a technological scouting concentrated for possible NIC solutions circuit, this research was still conditioned and focused of broadband application to the conversion an electrically small radiating element load; in Section 4, we identify the technology and choice of NIC circuit solution; in Section 6 we describe the work to realize the basic support of a simulation model; in Section 7 we introduce the activity regards the PCB design and circuit routing; in Section 8 we describe the industrialization and manufacturing NIC prototypes; in Section 9 we report the first RF characterizations on the two prototypes. Finally, Section 10, we deal with additional experimental test and future research activities

1.1 General consideration of frequency band chosen for the project

The portion of the spectrum up to now used for the radiopropagation has been limited to the range between 30 *kHz* and 300 *GHz* and , in this range , the portion more efficiently , and economically usable, is that of the 30 *MHz* to 3 *GHz* . In particular , within this range of frequencies they operate the most modern communication technologies (Digital Audio Broadcasting DAB , DVB - T Digital Video Broadcasting Terrestrial , mobile 2G and 3G , Wi - Max , etc ...) .

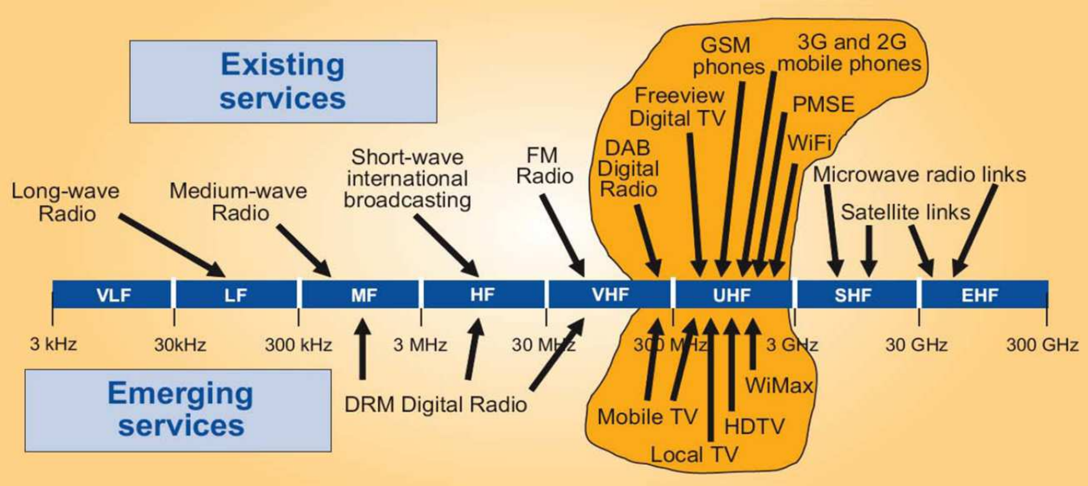

Fig. 1: Radio spectrum for modern broadcast communications technologies.

In order to design the best way a radio communication , on a more or less wide band of frequencies , it is necessary to take into account the antenna radiation characteristics used and the type of service that the antenna must support . In practice it may be employed to type *omniband* (Wide Band or Ultra-Wide Band antennas) such as to operate on a very wide band of frequencies by the use of non-resonant radiating elements , or alternatively it is possible to use *multi-band antennas* , realized with suitably loaded resonant radiating elements, such as to generate multiple resonance frequency bands.

The arrangement and the physical dimensions of the conductors that constitute and characterize the types of radiating element, are related to the practical use which is intended for the radio-link and the frequency band in which it is employed. One of the difficulties that have in practice is the realization of broadband radiating elements, compact and efficient, also operating in the extreme lower of the VHF band. Given the considerable size that would be to assume the resonant dipole in these frequency bands, generally are used antennas electrically very short ($L/\lambda << 1$), where the height L of the radiant element is generally reduced with the integration of lumped elements, creating current distribution discontinuities (by mean capacity or inductances along the antenna conductors).

In the technique of receiving systems, the non-Foster Matching technology has the ability to achieve higher instantaneous bandwidths and/or impedance matching of short antenna (than the wavelength of the signal wave taken as reference [24]-[25]. The usefulness of being able to work with a larger instantaneous bandwidth, is the ability to simultaneously and effectively receive signals on a wide frequency range, without antenna reconfiguration mode or changing tuning within the receiver.

Based on previous considerations, the advantage achieved by using non-Foster technology matching with radiating element metamaterial-based, can play a key strategic role in the search for the most suitable innovative solution [24] in the field of broadband receivers systems, characterized by innovative electrically short radiating elements, efficient in the *Low-VHF*- frequency band (30 - 50 *MHz*).-

In order to realize an industrial product with non-Foster matching technology at low cost and easily reproducible, it is necessary to explore all practical requirements of an industrialized *NIC* solution, trying to estimate all possible unbalance associate at the nominal values of commercially discrete *SMD (Surface Mount Technology*) components and to delimit the inevitable parasitic effects associated with the circuit.

The parasitic components are associate to the proposed circuit solution, both to the process used for the realization of the product. It is therefore fundamental support of a *simulation model* throughout the cycle development product, reliable and robust, able to analyse and demonstrate the feasibility of the proposed circuit solution, and to verify and optimize the functional parameters of the final solution, showing the expected performance.

The research was therefore focus on the study and the realization of a *printed circuit NIC demonstrator* realized in SMD discrete components with the following characteristics: compact, high integration and low cost production. Objective of this research is the design, realization and industrialization of an active NIC demonstrator, for *Non-Foster Impedance Matching of Electrically small metamaterial-based antennas* application.

The demonstrator has been design to be use in VHF / UHF broadband applications, for systems operating in the frequency band ranging from about 30 *MHz* to 3000 *MHz* (COMM band).

Starting from a technological scouting and some experimental work, it was identified a circuit and technological solution for the NIC discrete design. It ' was then carried out a search on the active and passive components required to implement the chosen circuit solution. In particular for this activity, starting from the Data Sheet from leading suppliers, it was necessary to check on the market, passive and active available component at low cost for civil applications.

For the active component identification was performed a detailed analysis and verification of the *DC* electrical characteristics (polarization working point and absorptions…) RF, (broadband matching, noise figure, stability...) and packaging.

In particular, with the *ADS circuit simulator,* it was made a qualitative analysis of the active circuit components and parasitic elements, and it was defined therefore to the circuit diagram of the NIC with the nominal values of selected SMD components.

The circuit model has obtained with using *ADS simulator* and through this, to verify the feasibility of the device.

For a quantitative analysis of the parasitic circuit components, the PCB model was realised using 3D full wave model CST MWS simulator.

Finally, it was report the work done for the project and the PCB realisation, by the experimental results obtained on the two realized prototypes

1.2 Non-Foster Technology

Foster's theorem is an important theorem for the analysis and synthesis of electrical networks. The theorem states that the *reactance* (imaginary part of complex electrical impedance) *of a passive device with no losses to two terminals* (or equivalently a passive network to a port) *always has a monotonic behaviour with increasing frequency.*

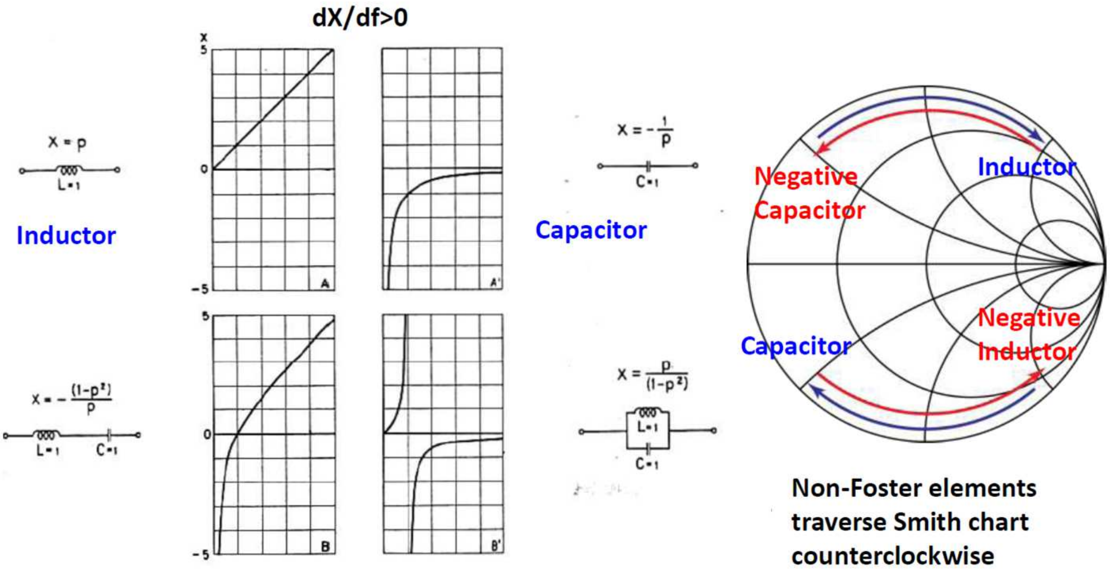

Non-Foster elements traverse Smith chart counterclockwise

Fig. 2: Reactance behavior of Foster and Non-Foster networks type

The hypothesis that the network should be passive and lossless, implies that, in the network, there are no dissipative elements such as resistors, amplifiers or power sources.

The network must therefore consist entirely of inductors and capacitors devices, where the impedance of the equivalent circuit will be purely an imaginary number.

Not all networks obey the th Foster theorem. For example networks containing amplifiers capable of creating negative capacitors and inductors by means of impedance conversion circuits NIC. These circuits are characterize by a positive reactance but with a negative slope trend in frequency.

1.3 Technology scouting for NIC solution

In the first phase of the research has been carried out a *technological scouting* concentrated for possible NIC solutions circuit. This research was still conditioned and focused application of broadband type but especially to the conversion of a "atypical load": the broadband impedance of the Electrically Small radiating element.

Electrically short antennas, in practice, have reactances capacitive with radiation resistance values very small and variable with the frequency.

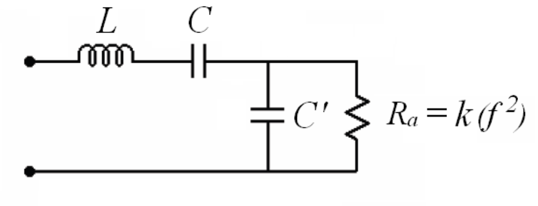

Fig. 3: Equivalent circuit of an ideal electrically short dipole

For matching antenna, the classical approach provides the annulment of the negative reactance by the insertion of a tuned inductive network, while the resistive part of the network, transforms and adapts the output impedance characteristic of the receiver.

This approach can provide a single frequency adaptation condition and also implementing more complex passive networks, to R, L elements, and C, it is however very complicated - if not impossible - to cancel the reactive behavior of the electrically short radiant element impedance.

To solve the problem of adaptation and thus improve the radiation characteristics, two possible techniques have been designed to be integrated with each other.

- First approach is to use a negative impedance converter (NIC) formed by few discrete elements active and passive, so as to adjust the antenna reactance (with the parasitic components of the circuit itself), by means of specific components in the circuit monitored in voltage;
- Second method is to design the antenna in the same printed circuit board of the receiver and possibly exploit the properties of artificial materials or metamaterials to increase both radiative efficiency and to facilitate the mutual adaptation broadband between the two devices.

The research activities of an industrial solution for the NIC device takes as a reference the work of Linvill [26] which was the first to demonstrate a practical realization of the negative impedance converter. In Figure 4 it is shown the circuit model, that is a quadrupole realized with two active elements, where the NIC conversion factor depends mainly on the current gain - approximately unitary - of the transistors.

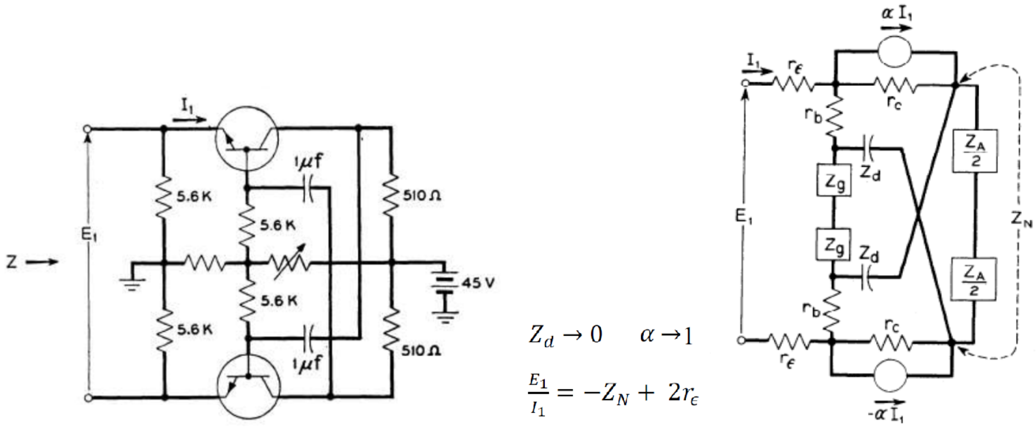

$$Z_d \to 0 \qquad \alpha \to 1$$

$$\frac{E_1}{I_1} = -Z_N + 2r_\epsilon$$

Fig. 4: Linvill circuit for the NIC device.

Recent experimental work using this circuit configuration to realize the inverter devices dedicated to modern RF applications (up to the L-band) [27]-[28]. In addition, we can create a NIC device using simple Operational Amps [29]-[30]. With modern *UWB Monolithic Operation Amplifiers* (OPA of Texas Instruments standard or CLC comLinear series) we can extend the performance to the RF bands). Finally some interesting configurations of CNIC devices (Current -inversion type NIC) have been developed in CMOS technology in the solid state for MMIC applications on analog filters [31].

1.4 Identification of technology and choice of NIC circuit solution

In most of the work reported in the literature, they are analysed several critical aspects linked to the project of a NIC (network power, stability, noise figure, intermodulation ...) and in any case dealt with theoretical methodologies supported by circuit simulators.

State of the art, we can say that there are no effective design methodology that synthesise a NIC broadband solutions to discrete components characterized by:

- Flexibility;

- Frequency scalability from the UHF / VHF band to the L-band;
- Low cost realization;
- High reproducibility of the processes;
- Stability and reliability.

To this aim challenger is necessary to choose a "*simple*" circuit solution, which minimizes the number of discrete components needed to the required function, and therefore also the number of parasitic variables that will need to balance (with calibration procedures or through the implementation of voltage control components).

Using the modern techniques for the realization of electronic PCBs is possible to stabilize the effect of the intrinsic parasitic components to the chosen circuit solution (e.g. welds, mutual position components ...), minimize production costs and to obtain a high integration of device (NIC + radiating element). Also, a correct search of components and low losses laminates selection, are fundamental choices for the project feasibility.

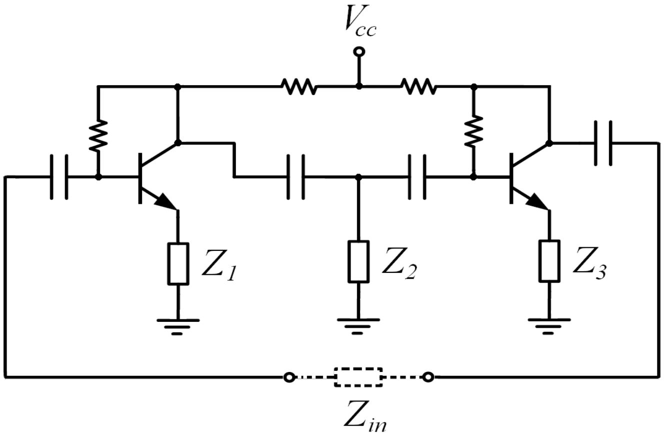

Fig. 5: Linvill SCS circuit in Short Circuit Stable configuration.

Figure 5 shown the circuit diagram chosen solution for our demonstrator: *Linvill SCS* configuration (*Short Circuit Stable*). The input impedance is proportional to the following quantities

$$Z_{in} \propto -Z_1 \frac{Z_3}{Z_2}$$

it can be shown that the stability of the circuit is affected by the theorems Brownlie - Hoskins [32]-[33] where considering the quadrupole device model.

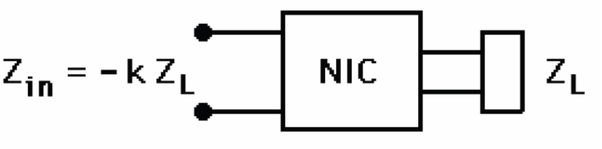

Fig. 6: Input impedance of the NIC quadrupole model

The NICs devices can be define as stable open circuits at one port of the quadrupole and stable short circuits to the other ports. More precisely, for each of the passive Z_L load impedance (port 2), the equivalent input network to port 1 is a stable open circuit, while for each passive impedance Z_L load (port 1, the equivalent input network to port 2 is a short- circuit stable.

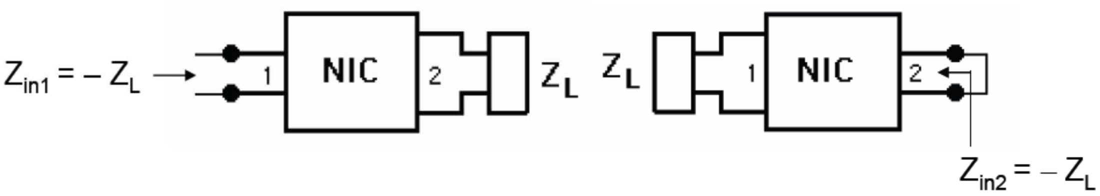

Fig. 7: NICs Open and Short Circuit Stable configuration

In general, the intrinsic stability condition of a NIC , poses constraints to the impedances of the modules connected to the port of stable open circuit *OCS* (*Open Circuit Stable*) with those of the port short circuit stable *SCS* (*Short Circuit Stable*). The stability condition can be expressed analytically as follows

$$|Z_{L1}| > |Z_{in1}| \quad \text{e} \quad |Z_{L2}| < |Z_{in2}|$$

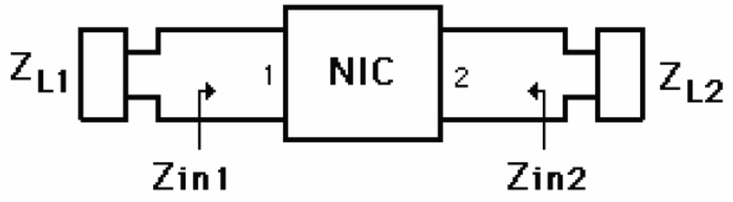

Fig. 8: NIC Stability Condictions

Regards the definition of the margins of stability, it is always possible to apply the feedback systems technique [34].

1.5 Implementation selected NIC circuital solution.

The realization of high-frequency circuit with discrete active components is generally problematic because we need to isolate the DC signals (power supply of the network) with RF signals.

Parasitic impedance associated with the power network, in presence of RF signal transients, may create feedback paths not provided, with no expected performance from what you would expect from simulation model

Manufacturers of active components have now standardized the format two-port S-parameter files, compatible with various RF simulation software on the market (*s2p* format). This data can be downloaded free of manufacturers' websites in text file format. Some manufacturers also provide the non-linear behavior device, using *Spice parameters*.

The latter type format is very useful in the case where the chosen circuit configuration does not coincide with that characterized reported in the Data Sheet or in the "application notes".

Generally , in order to verify the feasibility of the proposed circuit design , the qualitative performance of the active RF circuit are determined starting from the S-parameters of active two-port devices supplied by the manufacturer. All remaining connecting lines between active and passive devices are considered as perfect conductors, while the concentrated passive devices are considered ideal without parasitic reactive components. The problem has high frequency, where to ensure the feasibility, it is necessary to consider electrical lengths of the connections than physical ones provided PCB and insulation between signals. The correct choice of components and the most critical of the project activities.

For the active device of the circuit (see Figure 4) has chosen a wideband transistors for applications *Low Noise Amplifier* (LNA) in *NPN* technology. The choice and fall on a broadband amplifier with a high dynamic, with the possibility of use in transmission and reception equipment operating in V/UHF, easily commercially available. The typical initial specifications are as follows

- 3 dB bandwidth: 50 ÷ 2.500 *MHz*
- Input and Output Impedance 50 *Ohm*
- Low Cost
- Absorption: V_{DC} typ 5 V; I_{DC} max 100 *mA*
- Max. Input Power W/O Compression: -20 dBm
- Output P1dB: +5 dBm
- TOI (third order intercept point): +10 dBm
- Noise Figure: < 3

The choice of possible manufacturer was also performed on the quality and reliability of the documentation provided. Among the usable devices, the model *BFG520* of *NXP* , mounted in an inexpensive plastic container has been selected (*SOT343*) with very reduced overall dimensions , characterized by pin 4 as shown in the following figure:

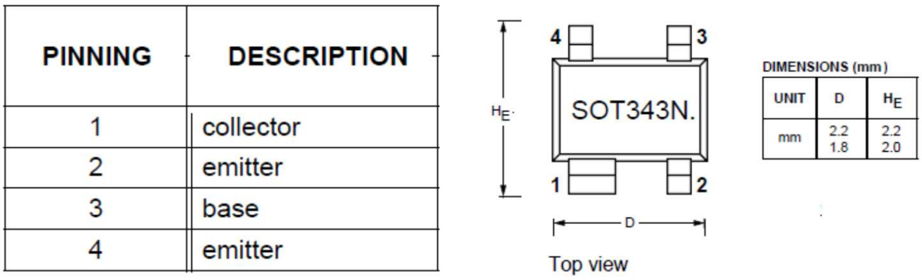

PINNING	DESCRIPTION
1	collector
2	emitter
3	base
4	emitter

DIMENSIONS (mm)

UNIT	D	H_E
mm	2.2 1.8	2.2 2.0

Fig. 9: Packaging and description of BJT

More or less similar features can however also be obtain from other manufacturers in the same category (e.g. MRF559 and NE46735/2SC2954) but the BFG520 presents a good cost/performance but also has extensive documentation on the S-parameters and parameters SPICE.

For passive components (Resistors, Capacitors and Inductors) the choice fell on SMD components *Murata* (www.murata.com) using standard size (0805) or (0603) to achieve the high integration of the circuit and minimize the parasitic components.

The laminate used for the NIC PCB is a classic *FR4* material , with a thickness *h* = 0.8 *mm* double-sided , with the copper metallization thickness *t* = 0.035 *mm*.

1.6 NIC model on ADS circuit simulator.

As mentioned in the introduction, the research work proposed is the basic support of a simulation model throughout the cycle development product, which is reliable and robust, able to analyse/demonstrate the feasibility of the proposed circuit arrangement, showing the expected performance. The simulations were performed (first step) with the simulator Agilent ADS, based on circuit analysis in S-parameters and then verified by the most accurate SPICE parameters.

Objective of this activity is define a complete RF circuit diagram with the network DC for the NIC and the identification nominal values for the SMD elements available. In summary, the work done in this phase has been structure as below:

1) A first ADS model was created for testing S-parameters provided by the manufacturer (.s2p in file format) in the band of interest , and at the point of polarization as shown on the Data- Sheet (DS) of the device

S-Parameters con S2P Block

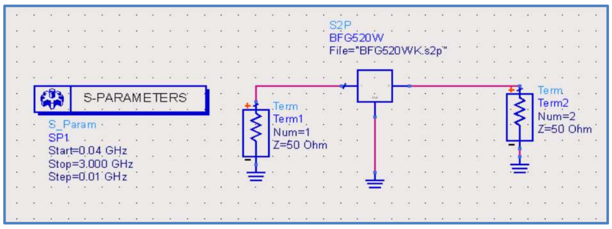

S_Param
SP1
Start=0.04 GHz
Stop=3.000 GHz
Step=0.01 GHz

Term
Term1
Num=1
Z=50 Ohm

S2P
BFG520W
File="BFG520WK.s2p"

Term
Term2
Num=2
Z=50 Ohm

Fig. 10: S2P linear model of the active two-port BJT device

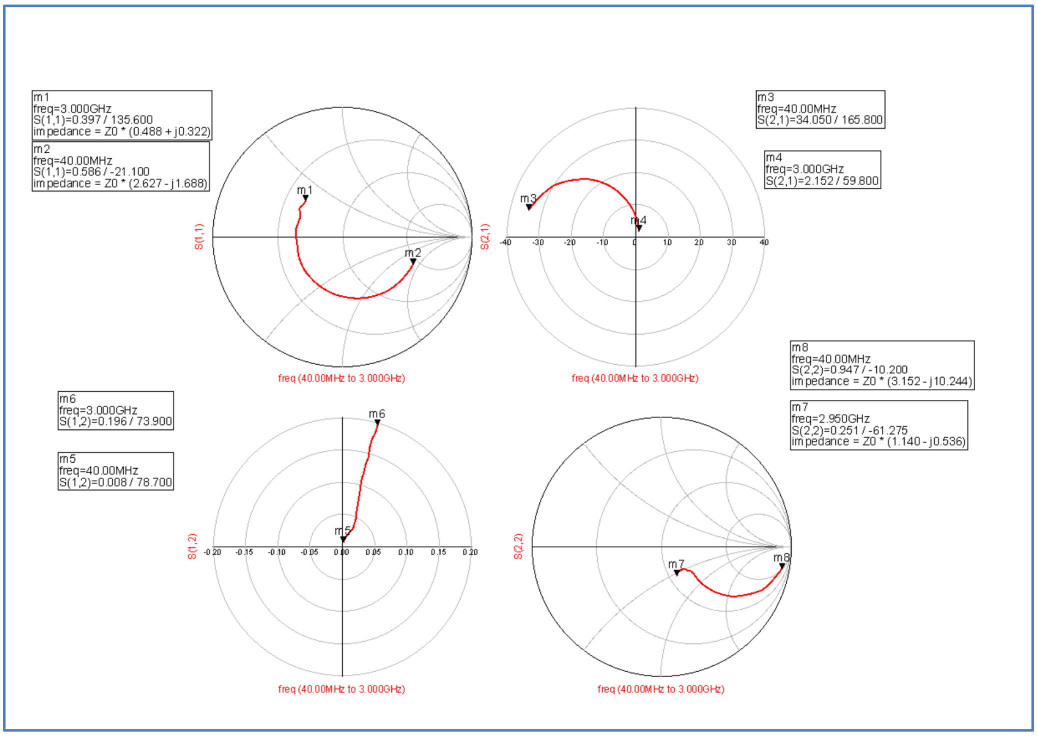

Fig. 11: Results obtained from linear model S2P active two-port device with ADS

S-Parameters BFG520W @ Vce = 6V Ic = 20mA

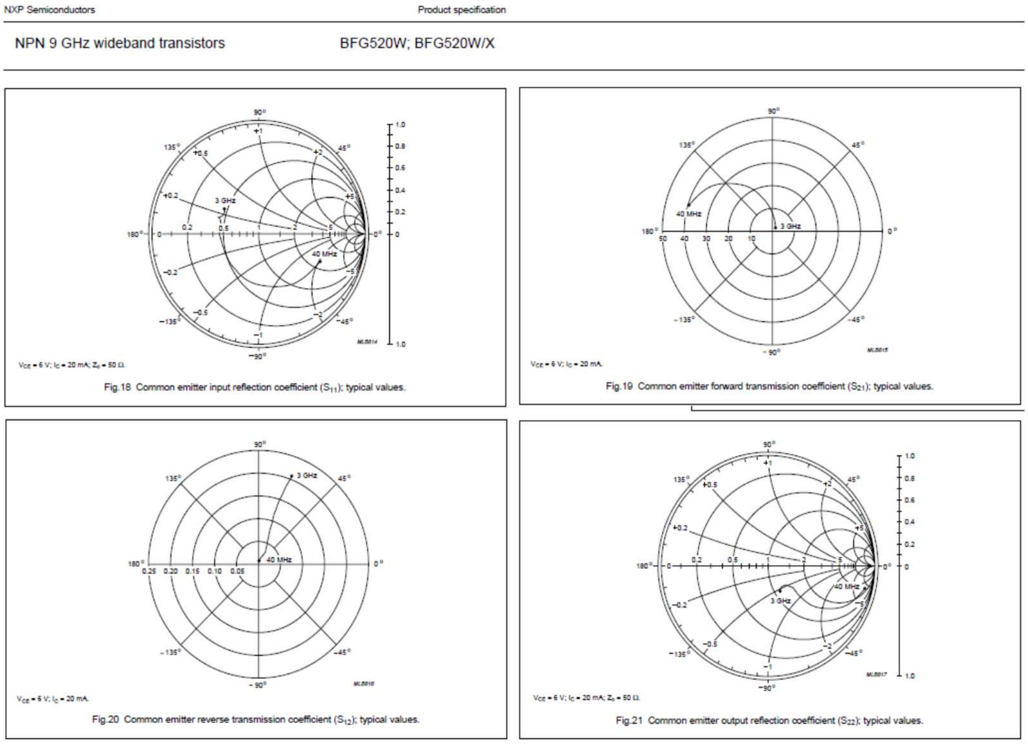
NXP Semiconductors Product specification

NPN 9 GHz wideband transistors BFG520W; BFG520W/X

V_{CE} = 6 V; I_C = 20 mA; Z_o = 50 Ω.

Fig.18 Common emitter input reflection coefficient (S_{11}); typical values.

V_{CE} = 6 V; I_C = 20 mA.

Fig.19 Common emitter forward transmission coefficient (S_{21}); typical values.

V_{CE} = 6 V; I_C = 20 mA.

Fig.20 Common emitter reverse transmission coefficient (S_{12}); typical values.

V_{CE} = 6 V; I_C = 20 mA; Z_o = 50 Ω.

Fig.21 Common emitter output reflection coefficient (S_{22}); typical values.

Fig. 12: DS BFG520: *S-Parameters*

2) Subsequently it is made of the nonlinear component of the device , by means of implementation of SPICE parameters + the parasitic components of the package provided by the manufacturer (Figure 13-14)

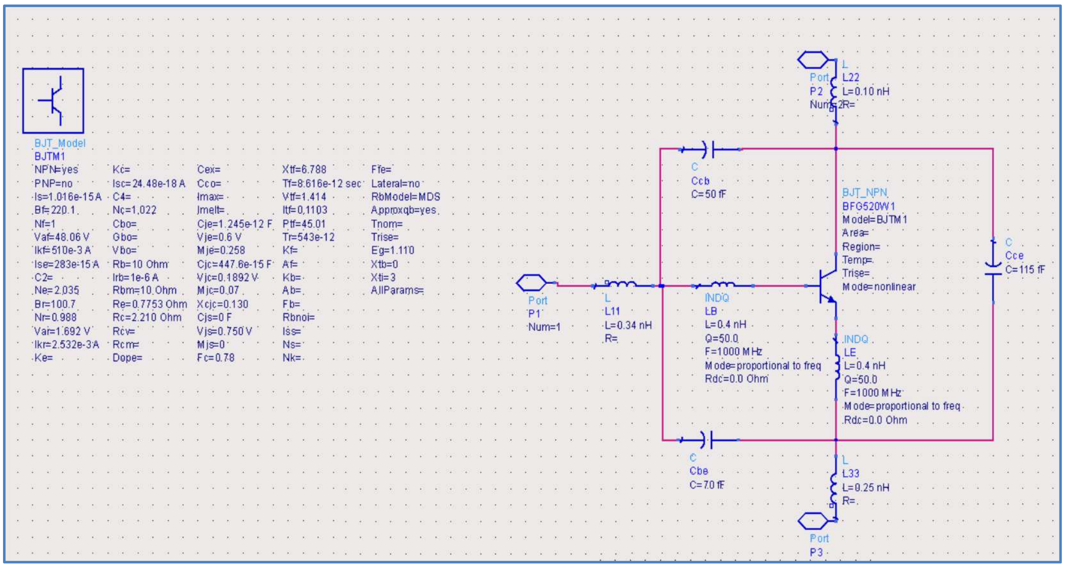

BJT_Model
BJTM1
NPN=yes
PNP=no
Is=1.016e-15 A
Bf=220.1
Nf=1
Vaf=48.06 V
Ikf=510e-3 A
Ise=283e-15 A
C2=
Ne=2.035
Br=100.7
Nr=0.988
Var=1.692 V
Ikr=2.532e-3 A
Ke=

Kc=
Isc=24.48e-18 A
C4=
Nc=1.022
Cbo=
Gbo=
Vbo=
Rb=10 Ohm
Irb=1e-6 A
Rbm=10 Ohm
Re=0.7753 Ohm
Rc=2.210 Ohm
Rcv=
Rcm=
Dope=

Cex=
Cco=
Imax=
Imelt=
Cje=1.245e-12 F
Vje=0.6 V
Mje=0.258
Cjc=447.6e-15 F
Vjc=0.1892 V
Mjc=0.07
Xcjc=0.130
Cjs=0 F
Vjs=0.750 V
Mjs=0
Fc=0.78

Xtf=6.788
Tf=8.616e-12 sec
Vtf=1.414
Itf=0.1103
Ptf=45.01
Tr=543e-12
Kf=
Af=
Kb=
Ab=
Fb=
Rbnoi=
Iss=
Ns=
Nk=

Ffe=
Lateral=no
RbModel=MDS
Approxqb=yes
Tnom=
Trise=
Eg=1.110
Xtb=0
Xti=3
AllParams=

Port
P2
Num=2

L
L22
L=0.10 nH
R=

C
Ccb
C=50 fF

BJT_NPN
BFG520W1
Model=BJTM1
Area=
Region=
Temp=
Trise=
Mode=nonlinear

C
Cce
C=115 fF

Port
P1
Num=1

L
L11
L=0.34 nH
R=

INDQ
LB
L=0.4 nH
Q=50.0
F=1000 MHz
Mode=proportional to freq
Rdc=0.0 Ohm

INDQ
LE
L=0.4 nH
Q=50.0
F=1000 MHz
Mode=proportional to freq
Rdc=0.0 Ohm

C
Cbe
C=70 fF

L
L33
L=0.25 nH
R=

Port
P3

Fig. 13: BJT SPICE Model with Packaging

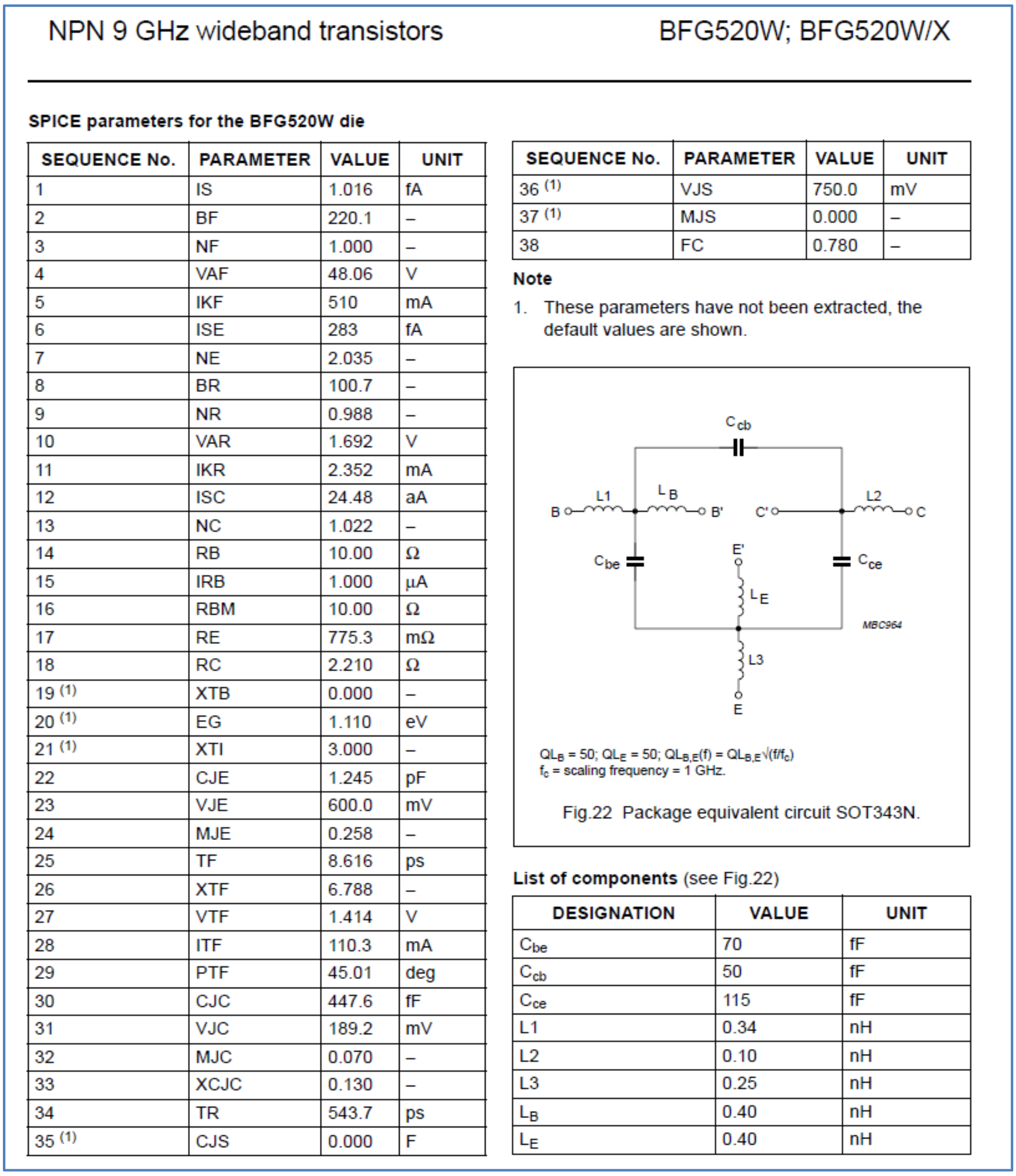

NPN 9 GHz wideband transistors BFG520W; BFG520W/X

SPICE parameters for the BFG520W die

SEQUENCE No.	PARAMETER	VALUE	UNIT
1	IS	1.016	fA
2	BF	220.1	–
3	NF	1.000	–
4	VAF	48.06	V
5	IKF	510	mA
6	ISE	283	fA
7	NE	2.035	–
8	BR	100.7	–
9	NR	0.988	–
10	VAR	1.692	V
11	IKR	2.352	mA
12	ISC	24.48	aA
13	NC	1.022	–
14	RB	10.00	Ω
15	IRB	1.000	μA
16	RBM	10.00	Ω
17	RE	775.3	mΩ
18	RC	2.210	Ω
19 (1)	XTB	0.000	–
20 (1)	EG	1.110	eV
21 (1)	XTI	3.000	–
22	CJE	1.245	pF
23	VJE	600.0	mV
24	MJE	0.258	–
25	TF	8.616	ps
26	XTF	6.788	–
27	VTF	1.414	V
28	ITF	110.3	mA
29	PTF	45.01	deg
30	CJC	447.6	fF
31	VJC	189.2	mV
32	MJC	0.070	–
33	XCJC	0.130	–
34	TR	543.7	ps
35 (1)	CJS	0.000	F
36 (1)	VJS	750.0	mV
37 (1)	MJS	0.000	–
38	FC	0.780	–

Note

1. These parameters have not been extracted, the default values are shown.

$QL_B = 50$; $QL_E = 50$; $QL_{B,E}(f) = QL_{B,E}\sqrt{(f/f_c)}$
f_c = scaling frequency = 1 GHz.

Fig.22 Package equivalent circuit SOT343N.

List of components (see Fig.22)

DESIGNATION	VALUE	UNIT
C_{be}	70	fF
C_{cb}	50	fF
C_{ce}	115	fF
L1	0.34	nH
L2	0.10	nH
L3	0.25	nH
L_B	0.40	nH
L_E	0.40	nH

Fig. 14: Equivalent Circuit BFG520: SPICE Parameters+ package SOT343N

3) Using the previous non-linear model with three ports, the simulations were performed to verify the convergence with the S-parameters Vs polarization of the transistor.

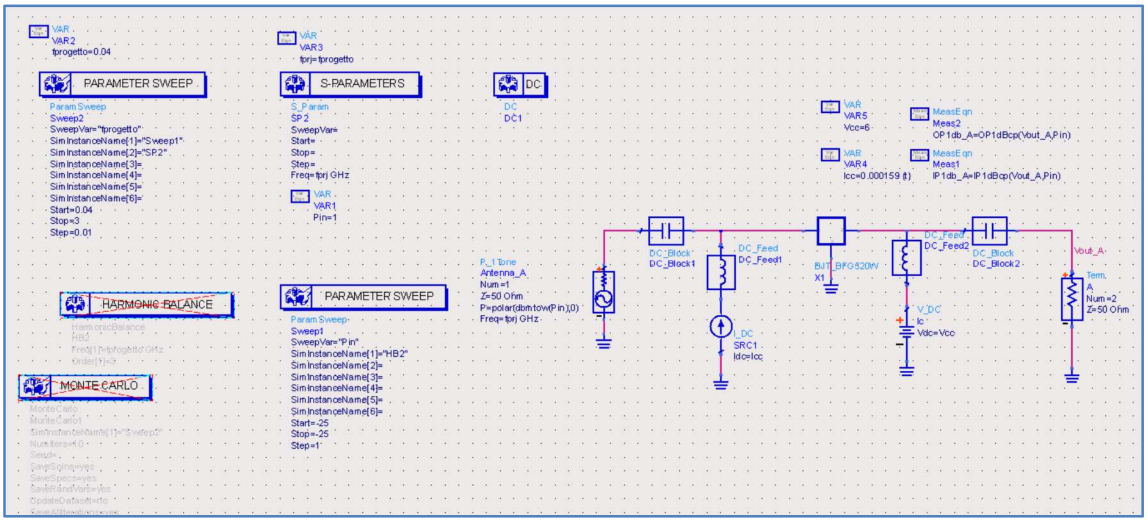

Fig. 15: Non-linear three ports transistor ADS model with DC bias

Well in this case it was found convergence on linear behavior with S-parameters. As an example have been reported simulation results obtained polarizing the SPICE model parameters in the working point discussed above ($Vce = 6\ V$; $Ic = 20\ mA$)

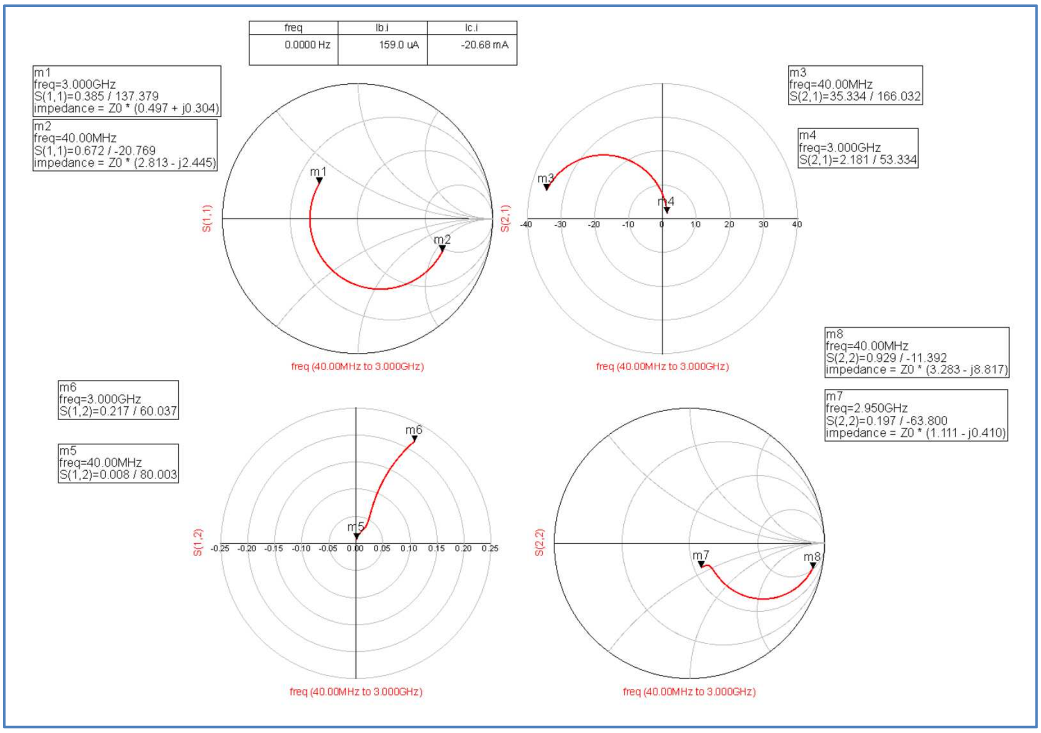

freq	Ib.i	Ic.i
0.0000 Hz	159.0 uA	-20.68 mA

Fig. 16: Results obtained with the non-linear model @ $Vce = 6\ V$ $Ic = 20.6\ mA$

4) The next step was to provide a first schematic of ADS NIC , using the non-linear model of the transistor, with SMD components required for biasing the active devices and to ensure the stability of the circuit.

With reference to the diagram in Figure 4 it is easily demonstrates that considering impedances Z_1 and Z_3 capacitive and Z_2 inductive, we can build a solution *NCI* (*Negative Capacitor Inverter*) with Z_{IN} capacitive *with negative value*.

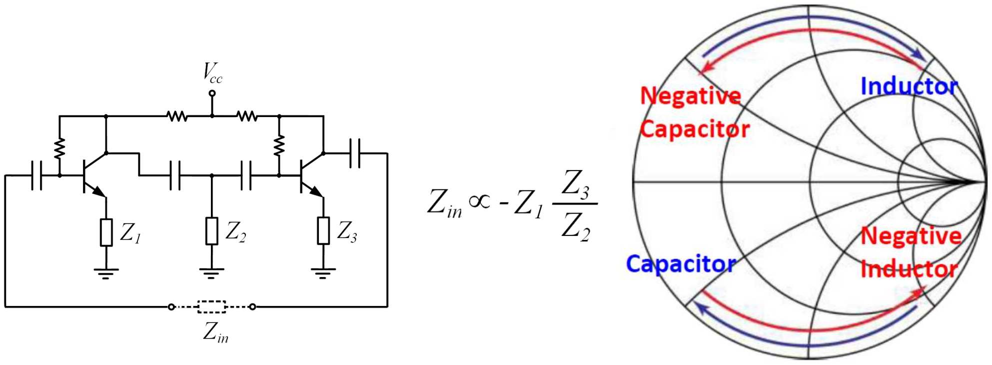

Fig. 17: Frequency behavior performance of NCI/NII device

Following figure shows the ADS circuit solution NCI model.

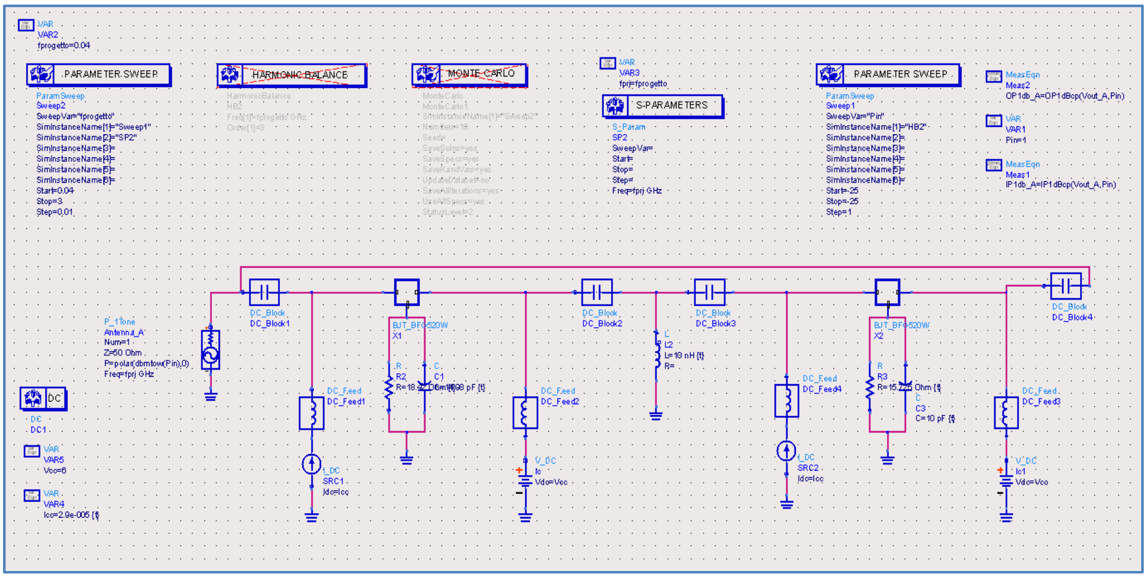

Fig. 18: ADS NCI model

By a manual optimization of the feedback resistor values, we get the following result

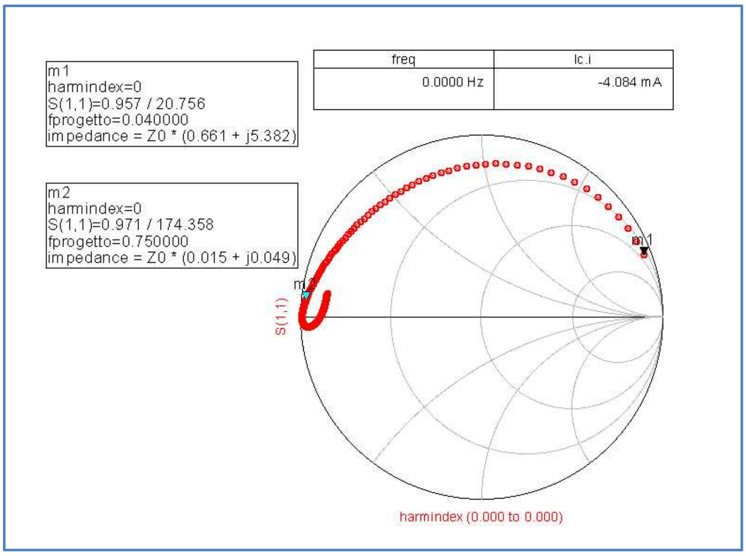

```
m1
harmindex=0
S(1,1)=0.957 / 20.756
fprogetto=0.040000
impedance = Z0 * (0.661 + j5.382)
```

```
m2
harmindex=0
S(1,1)=0.971 / 174.358
fprogetto=0.750000
impedance = Z0 * (0.015 + j0.049)
```

freq	Ic.i
0.0000 Hz	-4.084 mA

Fig. 19 Return loss of the NIC model in NCI configuration

as we can see from the previous figure, we find the typical capacitive negative impedance behaviour.

Obviously, the simulation model does not include all the parasitic elements introduced by the printed circuit board and for only frequencies involved are not too high such effects are negligible. It is therefore not appropriate to introduce ADS optimization processes for the calculation the optimal nominal SMD values of the circuit, but it is appropriate to perform Monte Carlo analyses to quantify the feasibility according to:

- tolerance selected passive and active components;
- verification the stability margins Vs operating point of active components;
- discretization of the nominal values available from the manufacturer;

At higher frequencies, it is more suitable to introduce full-wave 3D methods and take into account the distributed impedances associated with the PCB with any mutual coupling between the elements. The final PCB solution should also be possible to integrate - if necessary - SMD Voltage Controlled (Varicap). In this way, the final optimization of the parasitic elements will be partially compensated by a slight experimental adjustment, acting on such components.

After optimization process, we report in the following figure the circuit diagram chosen for the NIC PCB solution:

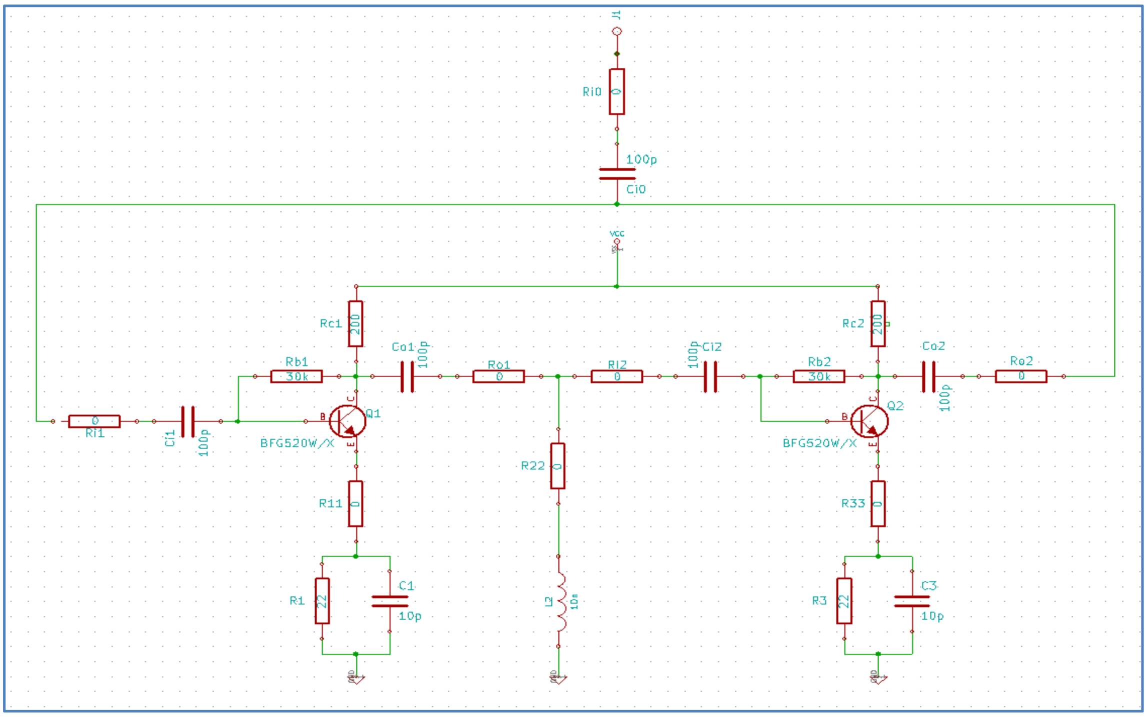

Fig. 20 Electrical Scheme drawing of the PCB NCI solution

Component	**Nominal Value**	**Package**	**Builder**
C1	10 pF	SMD 0603	Murata
C3	10 pF	SMD 0603	
Ci0	100 pF ÷ 470pF	SMD 0603	
Ci1	100 pF ÷ 470pF	SMD 0603	
Ci2	100 pF ÷ 470pF	SMD 0603	
Co1	100 pF ÷ 470pF	SMD 0603	
Co2	100 pF ÷ 470pF	SMD 0603	
L2	10 nH	SMD 0805	
Q1	BFG520W/X	SOT343N	NXP
Q2	BFG520W/X	SOT343N	
R1	22 ÷ 100 Ω	SMD 0805	Murata
R3	22 ÷ 100 Ω	SMD 0805	
R11	0 ÷ 10 Ω	SMD 0603	
R22	0 ÷ 10 Ω	SMD 0603	
R33	0 ÷ 10 Ω	SMD 0603	
Rb1	30 k Ω	SMD 0603	
Rb2	30 k Ω	SMD 0603	
Rc1	200 Ω	SMD 0805	
Rc2	200 Ω	SMD 0805	
Ri0	0 ÷ 10 Ω	SMD 0603	
Ri1	0 ÷ 10 Ω	SMD 0603	
Ri2	0 ÷ 10 Ω	SMD 0603	
Ro1	0 ÷ 10 Ω	SMD 0603	
Ro21	0 ÷ 10 Ω	SMD 0603	

Table 1: Bill Of Material of PCB NIC in NCI configuration

More complex PCB solutions, could get even better results in terms of stability, but the scope for improvement will probably not justify the increased sophistication (increase of cost, PCB dimension, absorption and dissipation reliability).

1.7 PCB design and circuit routing

As previously said, the higher frequencies is appropriate to introduce a full-wave 3D methods and take into consideration the impedances distributed associated to the PCB.

The aim of this activity is the definition of a PCB 3D model, with integrated SMD components in BOM and provided additional ones necessary for the experimental adjustment. In CST MWS linear and non-linear components were considered by inserting lumped port passive and active (SPICE model) available on the simulator. With reference to circuit Figure 20 is shown below the PCB demostrator solution achieved by the CAD of the electromagnetic simulator CST MWS.

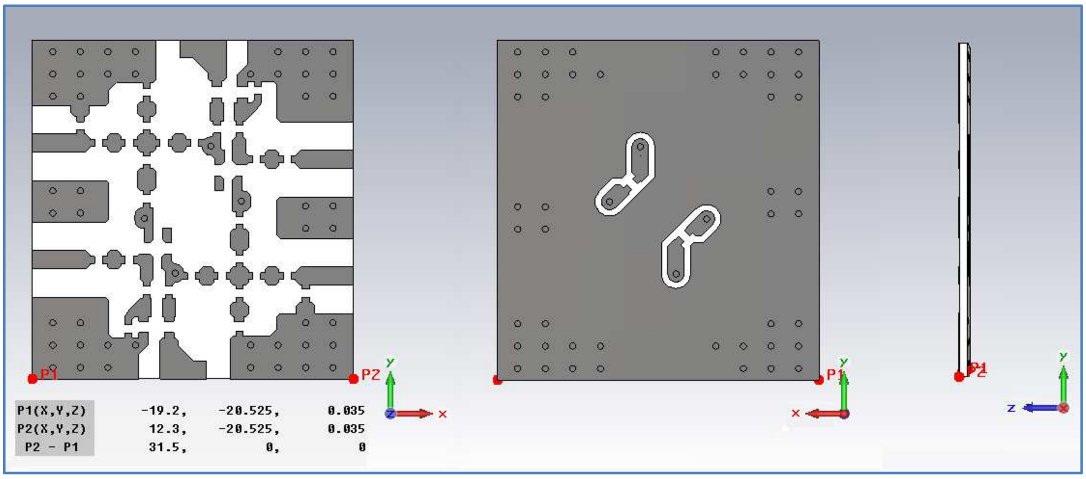

```
P1(X,Y,Z)     -19.2,   -20.525,     0.035
P2(X,Y,Z)      12.3,   -20.525,     0.035
 P2 - P1       31.5,         0,         0
```

Fig. 21 NIC PCB Model Prototype Solution

The laminate used for the printed circuit board is a classic double-side FR4, with thickness $h = 0.8\ mm$, the copper metallization thickness $t = 0.035\ mm$. The geometrical dimensions of the prototype, including SMA or MMCX type RF connector, can be estimated as follows table:

BASE (x)	50	[*mm*]
HEIGHT (y)	30	[*mm*]
DEPTH (z)	5	[*mm*]

Table 2: Bill Of Material of PCB NIC in NCI configuration

Figure 21 shows the CST model. The CAD EM including: 6 lumped active ports (SPICE parameters two transistors); the lumped ports for passive SMD components (the package of components, with its real geometric dimensions, displayed in the model but not considered in the simulation box); RF feed connector it used a Wave Ports. The model not include filters for the isolation in DC and the power supply network.

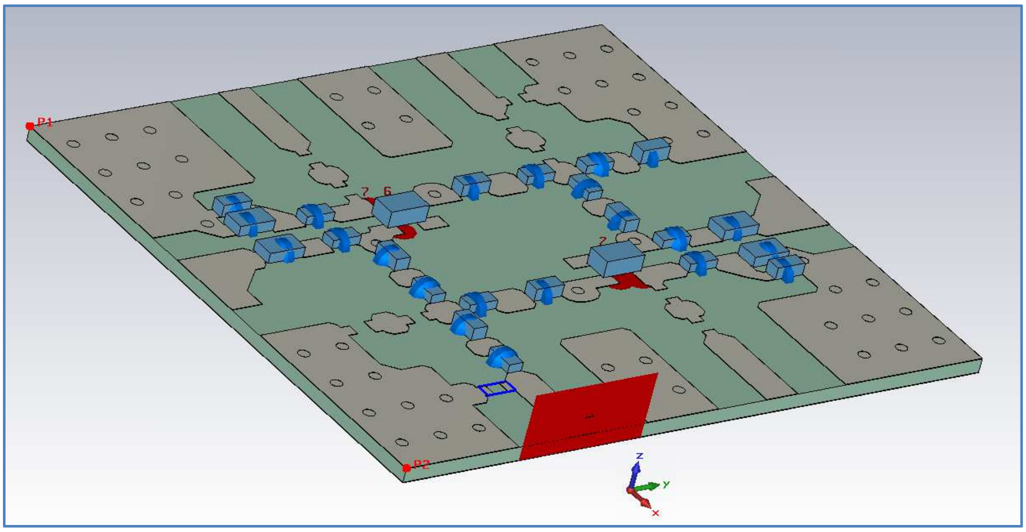

Fig. 22 CST CAD Model for Prototype Solution

Considering the set of nominal SMD values provided in the BOM, the first results of simulations with the CST full-wave model showed divergence phenomena between S11 CST MWS results, in high frequency, Vs the results obtained from the ADS circuit model.

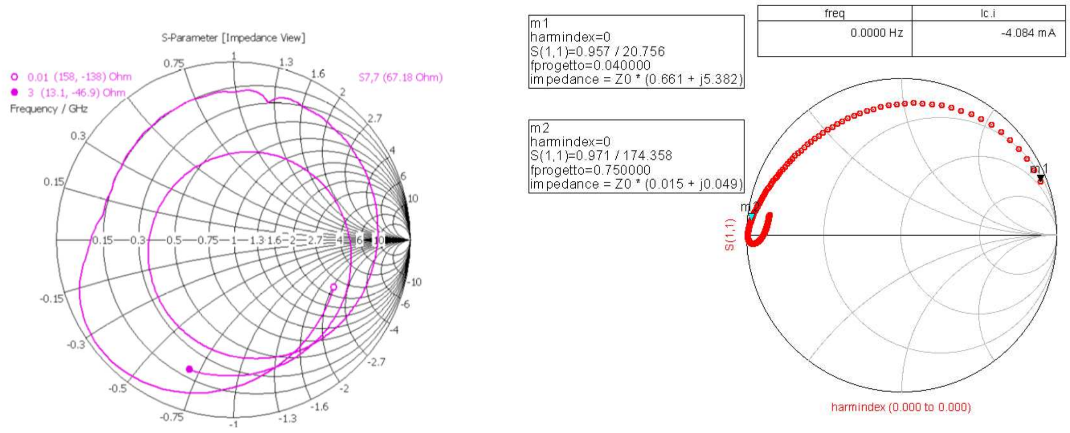

```
m1
harmindex=0
S(1,1)=0.957 / 20.756
fprogetto=0.040000
impedance = Z0 * (0.661 + j5.382)

m2
harmindex=0
S(1,1)=0.971 / 174.358
fprogetto=0.750000
impedance = Z0 * (0.015 + j0.049)
```

freq	Ic.i
0.0000 Hz	-4.084 mA

Fig. 23: S11 Simulation results PCB NCI model: CST MWS Vs ADS

The performance differences are connected to the distributed impedances of the associated parasitic components, which must now be identified and compensated. The activity was then organize proceeding parallel with:

- Tuning the passive components by simulation
- Re-modulate the PCB solution to compensate for the parasitic components.

The first step, may be implemented by parameter sweep simulation of different nominal values of resistance, capacitance and inductance of the lumped port passive (nominal value does not continue but discretized). For the second point, it is necessary at the experimental level analysis, by acting on some SMD components and of a different polarization of the devices.

1.8 Industrialization and manufacturing NIC prototypes

As previously reported, the work performed simulation cannot predict all the parasitic elements present and introduced by the printed circuit board; also the model presented not consider the effect of the supply network on the RF behavior of the active devices.

To get a more complete view of the issues related to the practical realization of the demonstrator, it must be taken into account several factors:

- The realization of the PCB must provide the appropriate *spare components* SMD to operate on a trial basis on compensation of the parasitic components by slight adjustments on the expected ratings.
- It must manage the *potential instability* (tendency to oscillation on circuit under test). The simulation normally does not take account all the couplings parasites due to the real circuit, which can oscillate for external feedback conditions not foreseen at the same circuit. In particular minimize the parasitic capacitance between *collector and base of the transistors*.
- The performance is also related to the *transistor bias* . Consequently it is important to choose a bias circuit, which makes the operating point less depending on temperature or the tolerance of the transistor parameters.

- On the NIC PCB circuit, it is necessary to introduce a isolation broadband network for DC component from the power supply.

With reference to the Figure 20, in the PCB scheme we have nevertheless been provided for some spare components (Resistors 0 Ohm), able to adjust and modulate the impedance of the NIC, or to allow the addition of damping resistors series, suitable in size to avoid any oscillation conditions. In particular, as regards the isolation in DC, in Figure 22 has been report the updated circuit diagram, modified with some addition components for the broadband RF decoupling with the power supply network (*choke*).

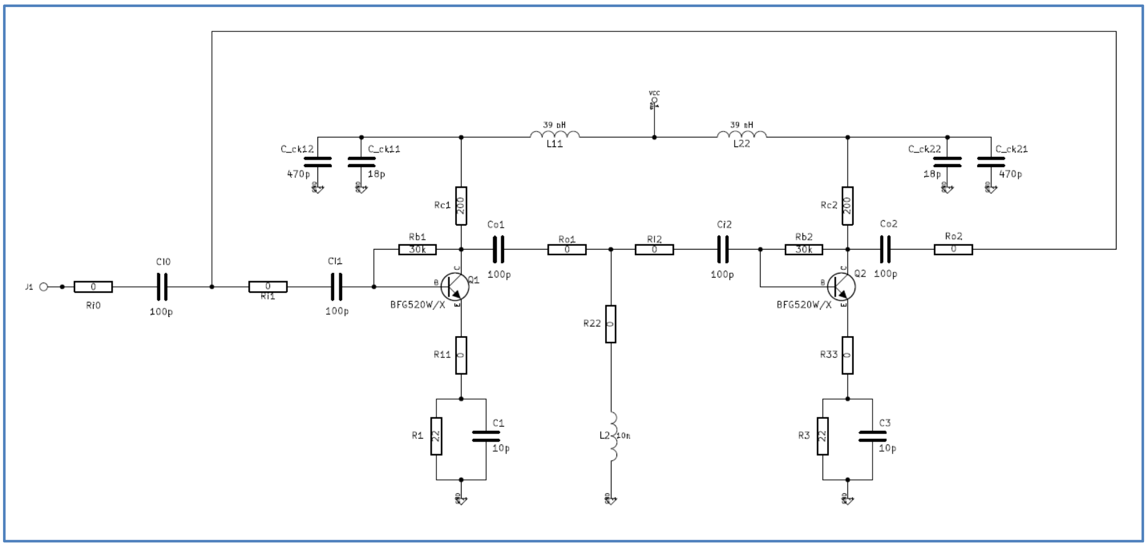

Fig. 24: NIC circuit diagram including choke for isolation network in DC.

More specifically, the DC isolation is obtained by inserting the circuit two additional inductor (L_{11} and L_{22}) and four additional capacitor ($C_{ck11,12,21,22}$), The additional component realize two low-pass filters that can close the RF current to ground using the four capacitor. Simultaneously provide, through the two inductors, the current supply to the two transistors. The nominal values chosen for the two filter were select to obtain a DC isolation band not less than 10 dB. For the filter analysis was used ADS simulator and in the following figure shows the simulated performance:

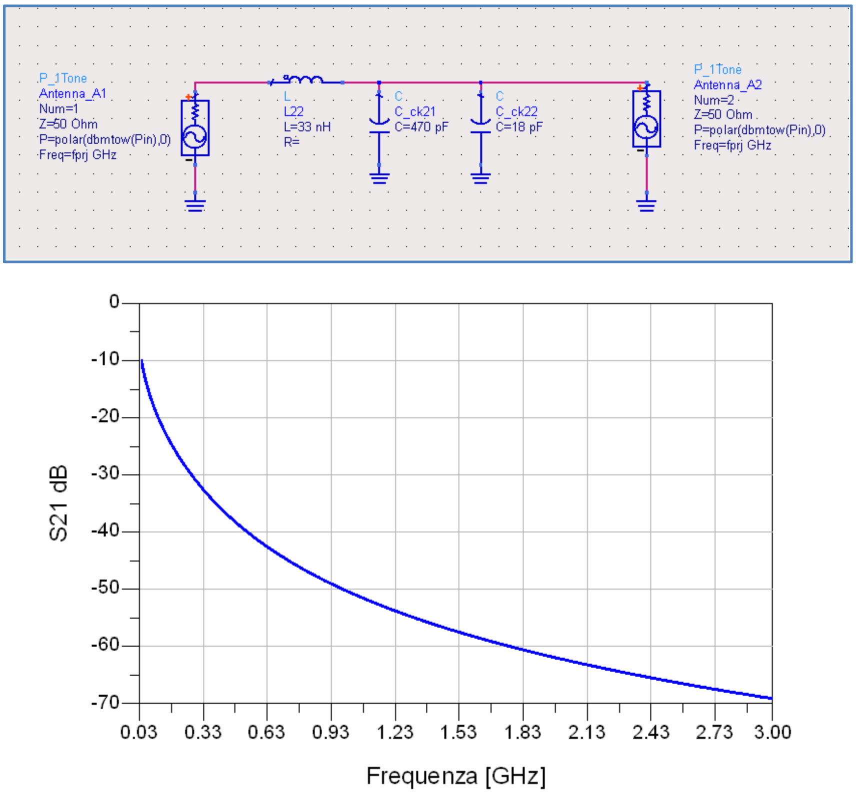

Fig. 25: Choke circuit diagram for the isolation in DC and the RF signal attenuation.

The circuit model of the complete NIC was then upgraded, inputting, on the simulator , the circuit variants introduced for the biasing network and power filters.

In Figure 26 it is possible to find the final ADS model, while Figure 24 show results obtained from the simulation taking into account the nominal values of the components used and considering the parasitic components of the PCB.

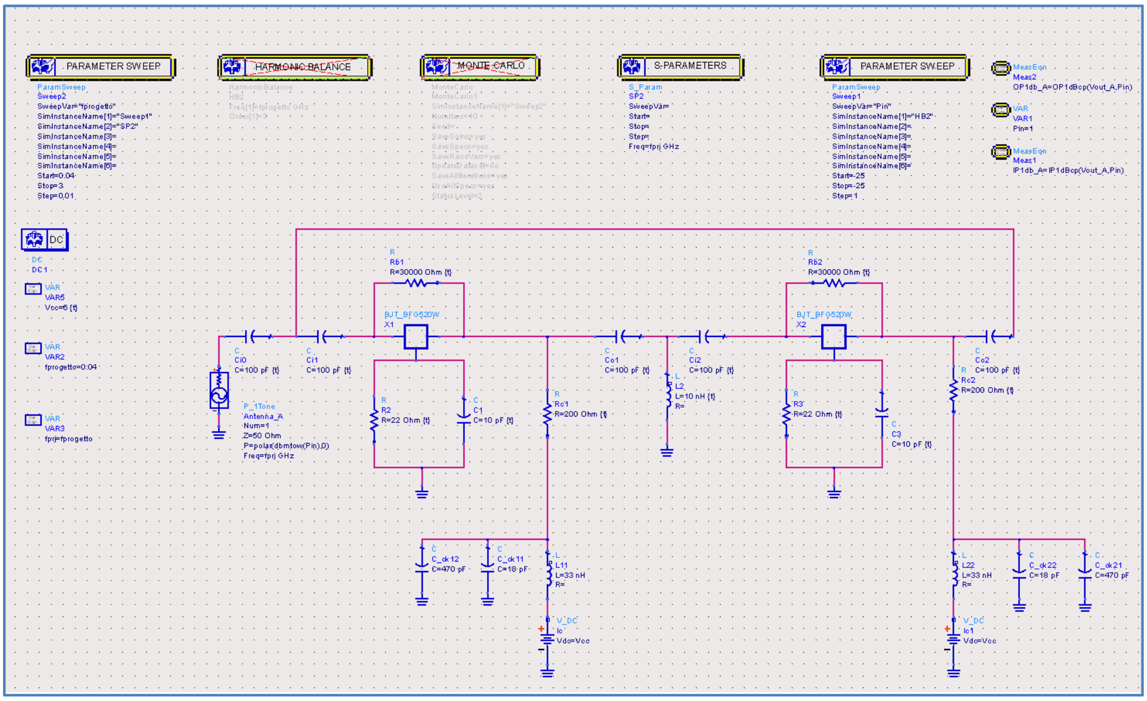

Fig. 26: ADS circuit model with the biasing and isolation network

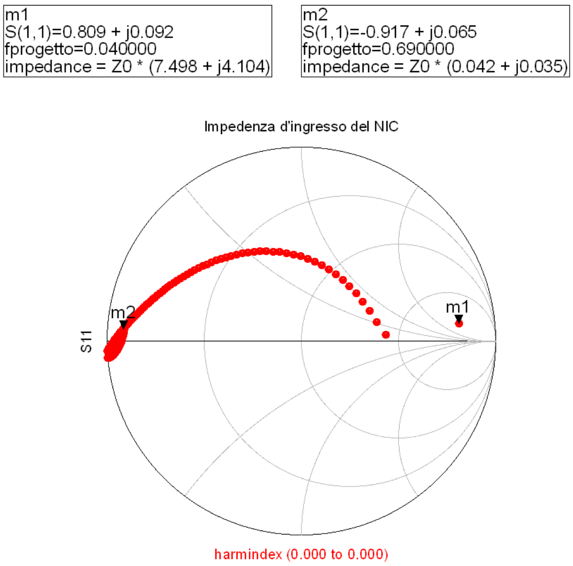

freq	Ic.i
0.0000 Hz	11.27 mA

Fig. 27: ADS Simulation results: Broadband S11 impedance and DC absorption

As we can see from the previous figure, the new change on the circuit have altered the performance of the NIC, generating an equivalent impedance with strong resistive component (which still decreases with increasing to frequency). Some parametric analyzes performed on the bias network, was observed that the resistive component introduced can be compensated by decreasing the bias current of the active device. For example, by varying the nominal values of resistors R_{c1} and R_{c2} of the two collector transistors, from 200 Ω to 2 $k\Omega$, it is possible to be able to obtain a behavior of the negative capacitive NIC with a better *Q* factor:

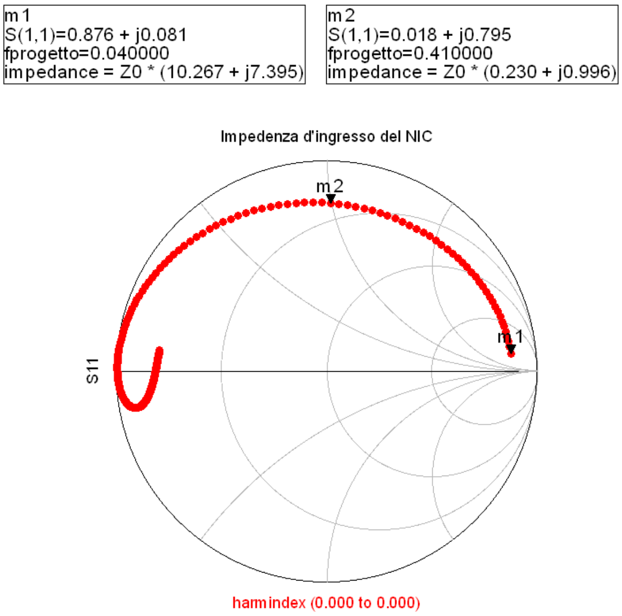

```
m1
S(1,1)=0.876 + j0.081
fprogetto=0.040000
impedance = Z0 * (10.267 + j7.395)
```

```
m2
S(1,1)=0.018 + j0.795
fprogetto=0.410000
impedance = Z0 * (0.230 + j0.996)
```

Fig. 28: ADS Simulation results: Broadband S11 input impedance with a better *Q* factor

As regards the potential *instability* (oscillation circuit), normally, it is sufficient to analyze the *stability factor k* of the element BJT active employed in the NCI in the chosen load conditions. The following figure shows the single amplifier circuit used for this NIC:

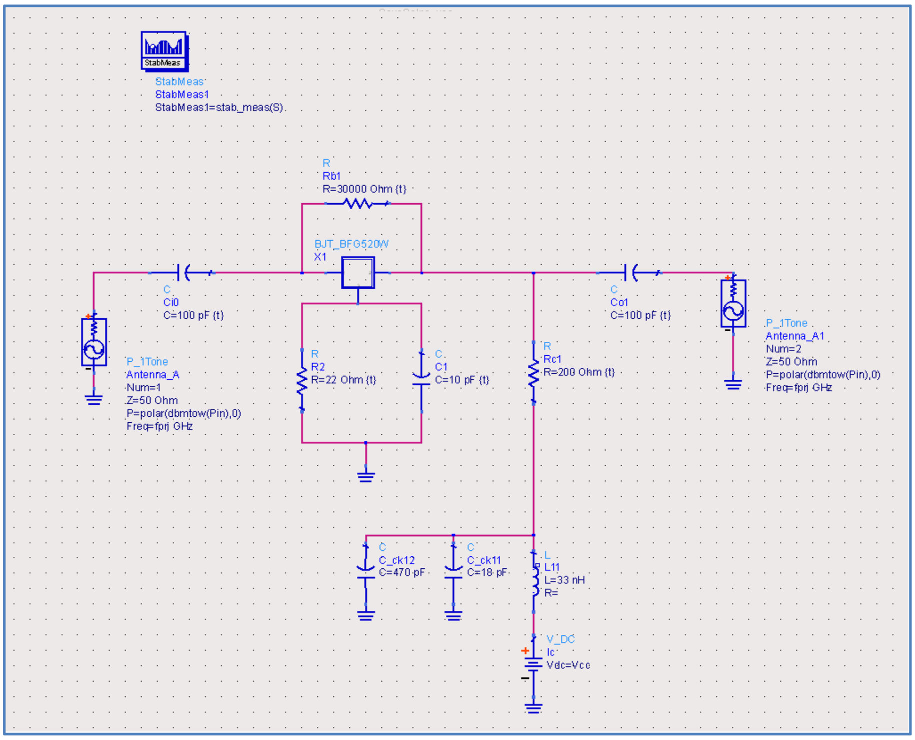

Fig. 29: ADS Circuit model for the unconditional stability analysis

Necessary and sufficient condition for the unconditional amplifier stability is that the *stability factor k* is *positive and greater than un*ity $k > 1$ defined as follows:

$$k = 1 + |S_{11}|^2 - |S_{22}|^2 - |S_{11}S_{22} - S_{12}S_{21}|^2$$

The k stability factor can be analyzed on ADS by function *StabMeas(S)* with *S* scattering matrix of the two-port network.

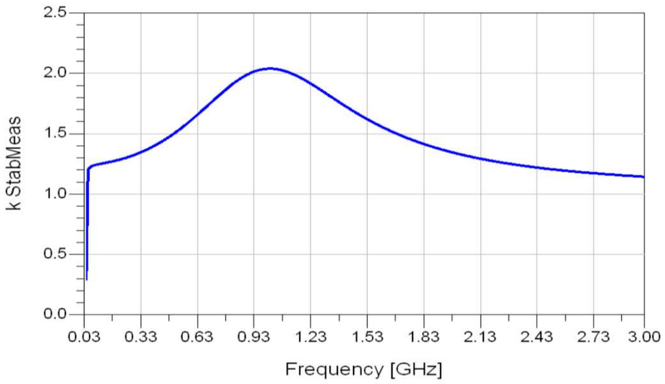

Fig. 30: Simulation of the unconditional stability factor for the active device.

As we can see from the previous Figure, the simulation of the parameter *k*, takes positive values greater the unit. It should however be mentioned that the simulation does not consider any parasites components present in the real PCB or external feedback conditions not foreseen at the same circuit.

The prediction of the parasitic components is the most complex and critical activities of the project NIC. Two prototypes were then realized to verify the functionality of the NIC; the repeatability of the performance and to identify possible unwanted parasitic components associated with the circuit solution.

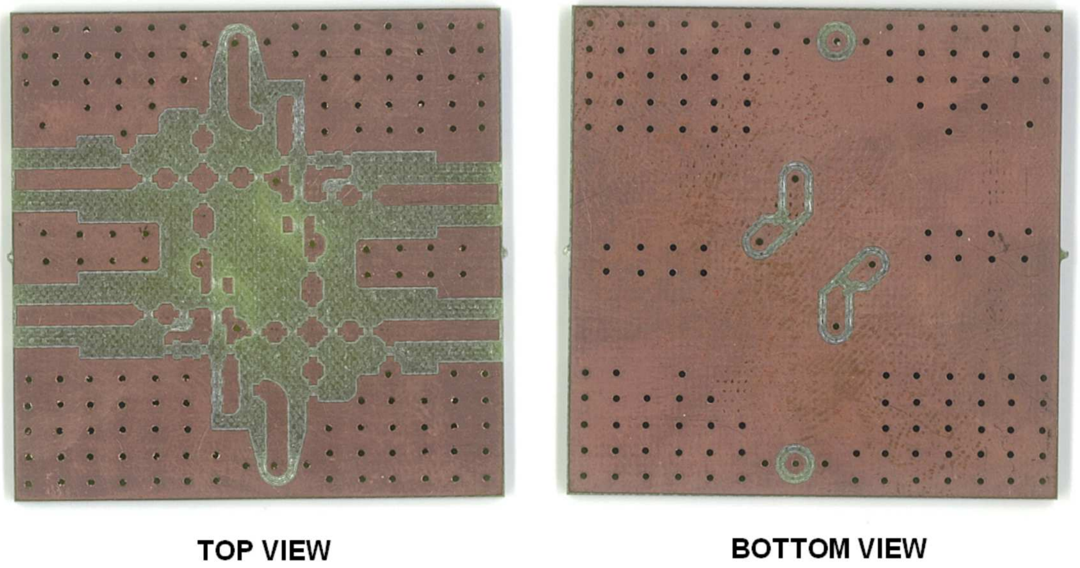

Fig. 31: Industrialized NIC PCB solution for experimental testing

The PCB was realize using a milling cutter machine. A FR-4 laminate material is well suited for the processing to removal of the conductive layer. The critical issues associated with this type of processing counts geometric alignment of the PCB layout (top and bottom) and in electrical continuity between the two layers . The electrical continuity of the RF signal (and proper reclosing of the earth currents) can be ensured appropriately metal process for the necessary via holes on the PCB.

For metallized via holes, particular care must be given to the welding of electrical connection between the two layers *near the collectors and the base* of the two transistors (four vias)

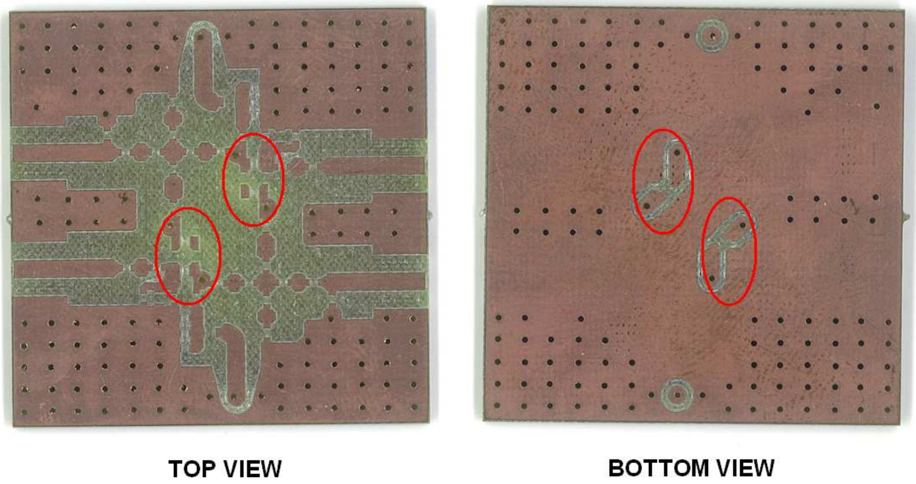

Fig. 32: Critical via holes on the chosen PCB solution.

More precisely, in this area, not a suitable welding can introduce significant parasitic components on the RF signal, localized in a very sensitive point in the network, where a capacitive or inductive component between the collector and the base of the two transistors, may limit the operating band the device or create instability of the circuit.

In the following Figures have been reported, the two prototypes integrated with the SMD components (nominal values shown on the electric diagram Figure 20).

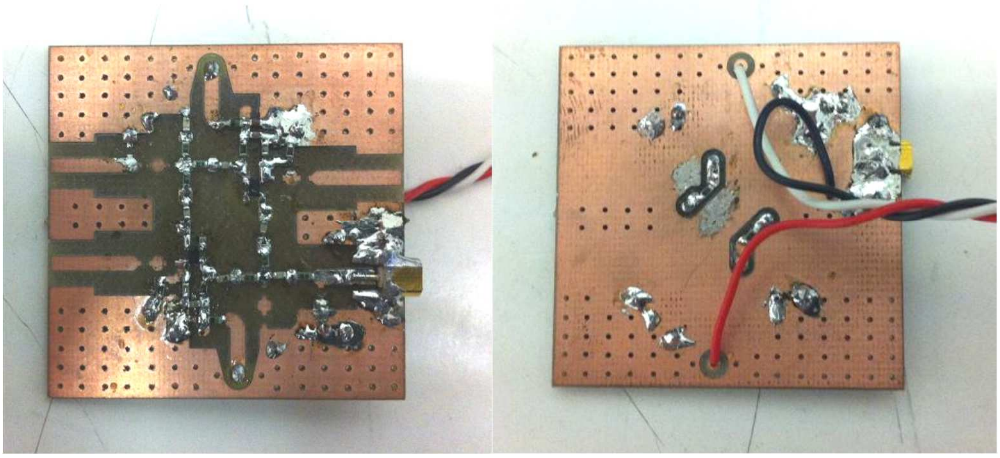

Fig. 33: NIC prototype SN01.

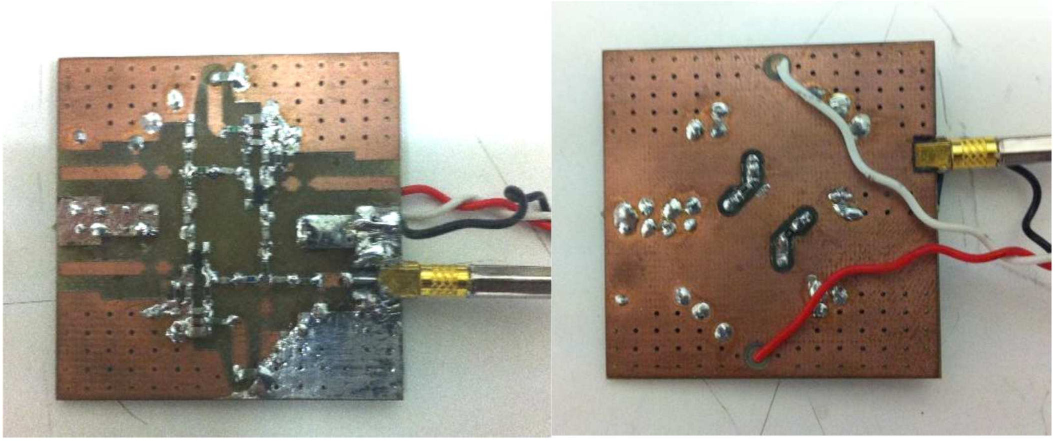

Fig. 34: NIC prototype SN02.

1.9 Performance Measurement NIC Prototypes

The first RF characterizations on the two prototypes were made by feeding the devices with a voltage V_{cc} between 5 *V* and 7 *V*. The power supply voltage was varied to obtain the total absorption expected for the chosen bias point. For a voltage $V_{cc} = 6.5\ V$, the total absorption of the device is $I_{cc} = 22\ mA$, as estimate on ADS model.

As we can see from Figure 33-34, to the RF interface it has been employed a coaxial connector MMCX male.

The input impedance measurements were carried out using a Vector Network Analyzer **dell'Anritsu MS2028C** (5 *kHz* to 20 *GHz*).

Fig. 35: NIC prototype SN02.

In the used measurement set-up, the instrument calibration includes only the coaxial cable terminated in SMA connector. The transition MMCX / SMA is therefore not included in the calibration procedure and in any case - for frequencies below 3 GHz - is not a critical in term of calibration residual error.

By setting the measure in terms of broadband *S-parameters* (Star Frequency = 40 *MHz* ; Stop Frequency = 3 *GHz* ; 1001 points in frequency) and by analyzing the performance of the S_{11} parameter on the Smith Chart, it is found for both the devices prototype an inductive and/or capacitive behavior in high frequency of the selected band. Center frequency band we find both an oscillation device (negative resistance behavior). Only a small portion of the band finds a NIC device behavior (Figure 36).

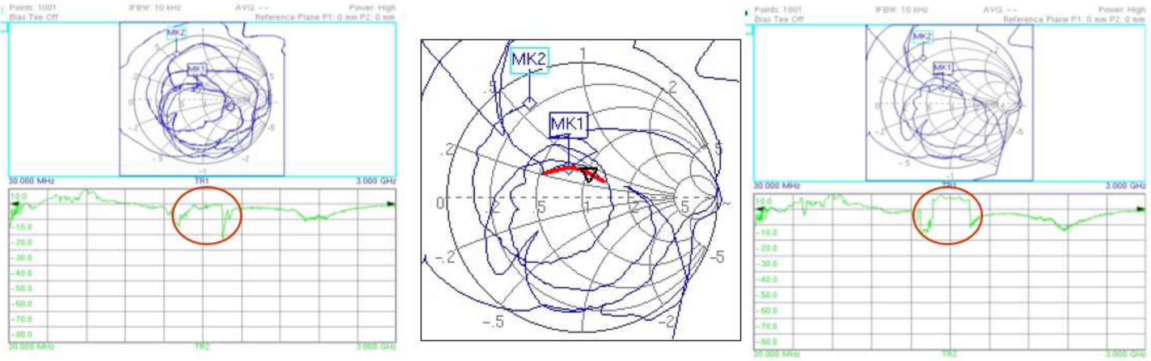

Fig. 36: Broadband characterization of prototypes: S11 Vs Frequency

1.10 Additional experimental tests and future research activities

For the two NIC prototypes, we were conducted additional experimental verification activities. Analyzing the effect of some variants, we have tried to trace the reasons for the lack of convergence on the expected behavior of the simulation model. So they were identified variants as recovery actions, which have provided a second revision of the circuit PCB solution.

After experimentally identified the parasitic components associated with the double-layer PCB solution, was then revised the project NIC to be developed on FR-4 laminate a single-layer. The new solution reduces the critical aspect associated with the parasitic components.

(Both the model and the project will possibly be revised and finalized in the final PCB with the integrated NIC device antenna)

In addition, a Derisking activities, has led to analyzed the possible alternatives NIC circuit solution, more stable and more reliable (but inevitably more expensive with Operational Amplifier).

Additional research activities have been report and summarized as follows (more details see Appendix 1):

- Finalization of an effective and efficient simulation model 3D full-wave nonlinear
- Realization and characterization of the new NIC in single layer PCB with integrated to the electrically small antenna
- Analysis of possible alternative NIC circuit solutions using Operational Amplifier technology

1.11 Summary

This Chapter is dedicated to the investigation on the use NIC active element for Non-Foster impedance UWB Matching of Electrically small metamaterial-based antenna application (VHF/UHF band). First, we starting from a short theoretical description of non-Foster technology and we will determine the type of the active load required to compensate the reactance (capacitive) of electrically small radiating element, with the aim of obtaining a broadband impedance matching by means of a NIC device. We will present the work of NIC technology scouting, associated to the analysis of some experimental works, which will allow us to identify the circuit and technology solution for the discrete components NIC project. It was then reported research on active and passive circuit components necessary to the implementation of the chosen solution. In particular, starting from Datasheet provided by the suppliers, the passive and active low cost components have identified. Through the ADS circuit simulators, we performed a qualitative parasitic components elements analysis of the active circuit; the analysis allowed defining NIC circuit diagram solution with the nominal values of the selected SMD components. The circuit diagram has been implemented in ADS model and simulations carried out to verify the device feasibility. For a quantitative analysis of circuit components parasites, a full wave 3D model with CST MWS simulator has been created. For the two prototypes NIC have not obtained the expected 3D full-wave simulation results. The activity needs additional experimental verification or possible alternative NIC circuit solutions using Operational Amplifier technology

1.12 References

[1] S.A. Tretyakov, “Meta-materials with wideband negative permittivity and permeability,” *Microw. Opt. Technol. Lett.*, vol. 31, no. 3, pp. 163-165, 2001.

[2] W. K. Chen, *The Circuit and Filters Handbook*. Boca Raton, FL: CRC Press, 2005.

[3] R.M. Foster, “A reactance theorem,” *Bell Syst. Tech. J.*, Vol. 3, pp. 259–267, 1924.

[4] J. L. Merill, “Theory of the negative impedance converter,” *Bell Syst. Tech. J.*, Vol. 30, pp. 88–109, 1951.

[5] J. G. Linvill, “Transistor negative impedance converters,” *Proc. IRE*, Vol. 41, pp. 725–729, 1953.

[6] A. Kaya, and E.Y. Yuksel, “Investigation of a compensated rectangular microstrip antenna with negative capacitor and negative inductor for bandwidth enhancement,” *IEEE Trans. Antennas Propagat.*, Vol. 55, pp. 1275-1282, 2007.

[7] G. Skahill, R.M. Rudich, and J. Piero, “Electrically small, efficient, wide-band, low-noise antenna elements,” *1998 Antenna Application Symposium*, pp. 214-231.

[8] S.E. Sussman-Fort, and R.M. Rudish, “Non-Foster Impedance Matching of Electrically-Small Antennas,” *IEEE Trans. Antennas Propagat.*, Vol. 57, pp. 2230-2241, 2009.

[9] J.T. Aberle and R. Loepsinger-Romak, *Active Antennas with Non-Foster Matching Networks*. San Rafael, CA: Morgan and Claypool Publishers, 2007.

[10] C. Di Nallo, G. Bit-Babik, and A. Faraone, “Wideband antenna using non-foster loading elements,” *2007 IEEE AP-S Int. Symp.*, pp. 4501-4504.

[11] G. Bit-Babik, C. Di Nallo, J. Svigelj, A. Faraone, “Small wideband antenna with non-Foster loading elements,” *2007 ICEAA*, pp. 105-107.

[12] J. Kern, D. H. Werner, and M. J. Wilhelm, “Active negative impedance loaded EBG structures for the realization of ultra-wide band artificial magnetic conductors,” *2003 IEEE AP-S Int. Symp.*, Vol. 2, pp. 427-430.

[13] D. F. Sievenpiper, “Superluminal Waveguides Based on Non-Foster Circuits for Broadband Leaky-Wave Antennas,” *IEEE Antennas Wireless Propag. Lett.*, Vol. 10, pp. 231 - 234, 2011.

[14] D. Sievenpiper, M. Jacob, and J. Long, "Active electromagnetic structures, metamaterials, and antennas," *2012 IEEE iWAT*, pp. 289-292.

[15] P. Jin, and R.W. Ziolkowski, "Broadband, efficient, electrically small metamaterial-inspired antennas facilitated by active near-field resonant parasitic elements," *IEEE Trans. Antennas Propagat.*, Vol. 58, pp. 318-327, 2010.

[16] R.W. Ziolkowski, and P. Jin, "Introduction of internal matching circuit to increase the bandwidth of a metamaterial-inspired efficient electrically small antenna," *2008 IEEE AP-S Int. Symp.*, pp. 1-4.

[17] H. Mirzaei, and G.V. Eleftheriades, "A wideband metamaterial-inspired compact antenna using embedded non-Foster matching," *2011 IEEE APS-URSI Int. Sym.*, pp. 1950-1953.

[18] H. Mirzaei, and G.V. Eleftheriades, "Antenna applications of non-Foster elements," *2012 IEEE iWAT*, pp. 281-284.

[19] S. Hrabar, I. Krois, and A. Kiricenko, "Towards active dispersionless ENZ meta-material for cloacking applications," *Metamaterials,* Vol. 4, pp. 89-97, 2010.

[20] S. Hrabar, I. Krois, I. Bonic, and A. Kiricenko, "Negative capacitor paves the way to ultra-broadband metamaterials," *Appl. Phys. Lett.*, Vol. 99, 254103, 2011.

[21] K. Z. Rajab, Y. Hao, D. Bao, C. G. Parini, J. Vazquez, and M. Philippakis, "Stability of active magnetoinductive metamaterials," *J. Appl. Phys.*, Vol. 108, 054904, 2010.

[22] E. Ugarte-Muñoz, S. Hrabar, D. Segovia-Vargas, and A. Kiricenko, "Stability of non-Foster reactive elements for use in active metamaterials and antennas," *IEEE Trans. Antennas Propagat.*, to be published.

[23] K.B. Alici and E. Ozbay "Electrically small split ring resonator antennas," *J. Appl. Phys.*, Vol. 101, pp. 08314, 2007.

[24] L.J. Chu, "Phisical Limitation of Omni-Directional Antennas," Journal of Applied Physics, Vol. 19, December 1948

[25] R.C. Hansen, "Fundamental Limitations in Antenna ," *Proceeding of the IEEE,* Vol. 69, No. 2, February," 1981

[26] J.G. Linvill, "Transistor Negative-Impedance Converters," *Proceedings of the IRE,* Vol. 41, pp. 725-729, 1953

[27] Stephen E. Sussman-Fort, "Matching Network Design Using Non-Foster Impedances," Int. *J. RF Microw. Comput.-Aided Eng.* vol 16, 2 (Mar. 2006), 135-142.

[28] Stephen E. Sussman-Fort, Ron M. Rudish, "Non-Foster Impedance Matching for Transmit Applications," *2006 IEEE International Workshop on Antenna Technology Small Antennas and Novel Metamaterials*, , vol., no.pp. 53- 56, March 6-8, 2006

[29] Cyril Svetoslavov Mechkov, "A heuristic approach to teaching negative impedance phenomenon", *Third International Bulgarian-Turkish Conference -*

Computer Science'06, http://www.circuit- fantasia.com/my_work/conferences/ cs_2006/paper.htm. Non-Foster Reactance Matching for Antennas 5

[30] Alan G. J. Holt and John R. Carey, “A Method of Obtaining Analog Circuits of Impedance Converters,” *IEEE Trans. On Circuit Theory*, Col. CT-15, No. 4, December 1968, 420 – 425

[31] Brennan, R.L. ,“ The CMOS negative impedance converter,” *Solid-State Circuits, IEEE Journal of*, Vol. 23° Issue 5, Oct 1988, 1272 – 1275

[32] J.D. Brownlie, “On the stability properties of a negative impedance converter,” *IEEE Trans. Circuits Theory*, vol. CT-13(1), pp 98-99, Mar. 1966D

[33] R.F. Hoskins, “Stability of negative impedance converter,” *Electron. Lett.*, vol.2, no 9. p 341, Sept. 1966D

[34] R.D. Middlebrook, “Measurements of loop gain in feedback systems,” *Int. J. Electron.*, vol. 38, no. 4, pp. 485-512, Apr 1975.

Chapter 2

Circular polarized patch antenna generating orbital angular momentum

The concept of OAM is well known at optical frequencies, where it has found application in trapping and manipulating of microscopic particles, imaging and communication systems [1]-[4]. Recently, it has been shown that an electromagnetic (EM) field with a non-zero OAM can be also generated in the microwave range using standard antenna systems [5]. Starting from this first demonstration, several systems generating EM fields with non-zero OAM have been proposed [5]-[9]. Such systems are based on two different approaches. The first one consists of a circular antenna array in which the different elements are fed with signals having the same amplitude and a progressive phase shift, such that the total delay between the first and the last element is an integer multiple l of 2π [5]-[6]. A variant of this approach is presented in [7] and makes use of a time-switched array. The second approach consists of using a reflector with a helical phase profile achieved by mechanically modifying a spiral [8] or parabolic [9] reflector.

However, both these approaches have some inherent drawbacks. In fact, the first approach requires the design and the implementation of a transmission line network to properly feed the array elements. On the other hand, the fabrication of a reflector with a helical phase profile is not easily replicable. Moreover, both solutions require considerable space occupancy, weight, and costs.

In contrast, at optical frequencies there are different techniques used to generate OAMs. As an example, the higher order laser modes of a laser cavity, also known as Laguerre-Gauss (LG) laser modes, have a non-zero OAM and can be either directly generated [10] or obtained by properly combining two Hermite-Gauss (HG) laser modes [11]. This means that, for instance, a LG^1_0 laser mode can be generated combining two orthogonal HG_{10} and HG_{01} modes with a $\pi/2$ phase delay between them [1].

Inspired by this technique, we may think of properly combine orthogonal higher order modes of resonant antennas to generate OAMs at microwave frequencies.

In this Chapter, in order to obtain an EM field with a non-zero OAM at microwave frequencies, we propose to use a single patch antenna. In particular, we show that the higher order modes of a circularly polarized patch antenna can be used to generate different OAM states. This solution is clearly cheaper, lighter and more compact compared to the ones already proposed [5]-[9]. Moreover, although OAM cannot be used to improve the performances of a communication system except in very particular cases [12], the proposed solution can be useful to experimentally investigate the properties of the OAM or to extend to microwave frequencies imaging and identification techniques based on OAM and developed in the optical regime [13].

The structure of the Chapter is as follows. In Section 1, we report the analytical study of a circular patch antenna and show that an EM field with non-zero OAM can be generated if we make this component working on higher order circularly polarized (CP) modes. In Section 2, we present the design procedure and the results of the full-wave simulations for an elliptical patch antenna generating a helical far-field radiation pattern with circular polarization. In Section 3, we validate these results through the characterization of the radiating and matching properties of a fabricated prototype. Finally, in Section 4, we summarize the obtained results.

2.1 Analytical Study

A patch antenna, in its general form, consists of a metallic patch placed on a grounded dielectric slab [14]. Over the last decades, patch antennas with different geometries have been proposed to satisfy several design constraints (see, for instance, [15]-[18]). Let’s consider the circular patch antenna depicted in Fig. 90. In some applications, this type of patch antenna is preferred to the rectangular one due to its greater flexibility in terms of achievable radiation patterns.

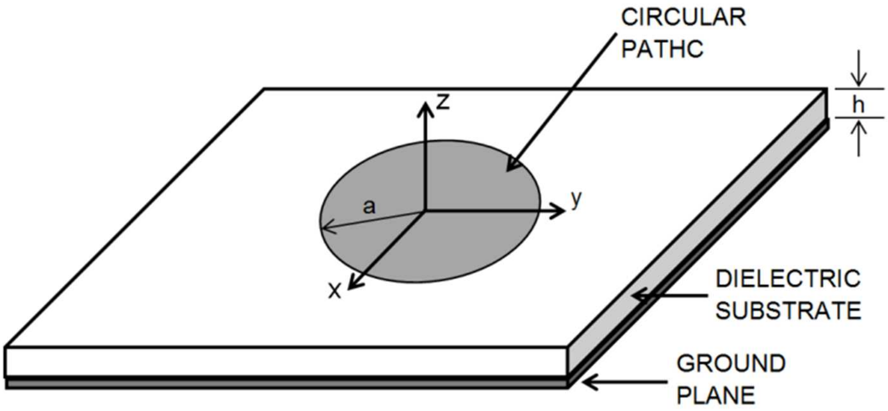

Fig. 37: Geometrical sketch of a circular patch antenna. The main geometrical parameters are the radius of the patch *a* and the thickness of the dielectric substrate *h*.

In order to evaluate the radiating performances of a patch antenna, different analysis methods can be used. In our case, we have chosen the cavity model that is a good compromise between accuracy of the obtained results and complexity of the model. This approximate model is based on considering the antenna to be a dielectric loaded resonant cavity.

In the case of a circular patch antenna, the radiated electric field components by a TM_{nm} mode can be derived by using the cavity model in cylindrical coordinates and are expressed as [19]:

$$\begin{aligned} E_{\theta n} &= j^n \frac{Vk_0 a}{2} \frac{e^{-jk_0 r}}{r} \cos n\varphi \left[J_{n+1}(\gamma) - J_{n-1}(\gamma) \right] \\ E_{\varphi n} &= j^n \frac{Vk_0 a}{2} \frac{e^{-jk_0 r}}{r} \cos\theta \sin n\varphi \left[J_{n+1}(\gamma) + J_{n-1}(\gamma) \right] \end{aligned} \tag{1}$$

where $V = hE_0 J_n(ka)$ is the edge voltage at $\varphi = 0$, *h* is the thickness of the dielectric substrate, E_0 is the value of the electric field at the edge of the patch, $\gamma = k_0 a \sin\theta$, *a* is the radius of the patch, and J_i is the Bessel function of the first kind and order *i*.

As anticipated in the introduction, we now investigate the use of CP higher order modes of a patch antenna in order to produce an EM field with non-zero OAM. Circular polarization can be obtained by using two coaxial cables with proper angular spacing such that two orthogonal modes with a proper phase shift are excited. Therefore, the total radiated field by a CP TM_{nm} mode can be considered as the superposition of the individual electric fields produced by the two orthogonal modes and obtained from (13):

$$\begin{aligned} E^{t}_{\theta n} &= E^{1}_{\theta n}(\phi,\theta) + jE^{2}_{\theta n}(\phi+\alpha,\theta) \\ E^{t}_{\varphi n} &= E^{1}_{\varphi n}(\phi,\theta) + jE^{2}_{\varphi n}(\phi+\alpha,\theta) \end{aligned} \tag{2}$$

where superscripts 1 and 2 correspond to the fields generated by the two coaxial cables, respectively, α is the angular spacing of the probes depending on the mode order [20], while the phase shift has been chosen equal to π/2 in order to obtain a right-handed circular polarized (RHCP) field.

From these expressions, we can derive the x and y components of the total radiated field:

$$\begin{aligned} E_x &= -j^{n}\frac{e^{-jk_0 r}}{2r} ahk_0 J_n(ak_0\sqrt{\varepsilon_r})\left[e^{-j(n\text{-}1)\phi}J_{n-1}(\gamma) - e^{-j(n+1)\phi}J_{n+1}(\gamma)\right]\mathrm{Cos}[\theta] = \\ &= Ae^{-j(n\text{-}1)\phi} - Be^{-j(n+1)\phi} \\ E_y &= j^{n+1}\frac{e^{-jk_0 r}}{2r} ahk_0 J_n(ak_0\sqrt{\varepsilon_r})\left[e^{-j(n\text{-}1)\phi}J_{n-1}(\gamma) + e^{-j(n+1)\phi}J_{n+1}(\gamma)\right]\mathrm{Cos}[\theta] = \\ &-j\left[Ae^{-j(n\text{-}1)\phi} + Be^{-j(n+1)\phi}\right] \end{aligned} \tag{3}$$

where:

$$\begin{aligned} A &= -j^{n}\frac{e^{-jk_0 r}}{2r} ahk_0 J_n(ak_0\sqrt{\varepsilon_r})\mathrm{Cos}[\theta]J_{n-1}(\gamma) \\ B &= -j^{n}\frac{e^{-jk_0 r}}{2r} ahk_0 J_n(ak_0\sqrt{\varepsilon_r})\mathrm{Cos}[\theta]J_{n+1}(\gamma) \end{aligned} \tag{4}$$

From (15) we note that the x-component (y-component) consists of the difference (the sum) of the same two terms, having phase evolutions of the forms $e^{-j(n-1)\varphi}$ and $e^{-j(n+1)\varphi}$, respectively.

However, for a patch antenna with typical geometrical and EM parameters, the amplitude of the second term is always significantly smaller than the one of the first term. In fact, the amplitude of the two terms differs only in the order of the Bessel function and, for small values of the argument, the higher the order of the function, the lower its value. This aspect has been also verified through several full-wave simulations, whose results are not reported here for sake of brevity. Moreover, as shown in Fig. 91 for the case of a patch antenna working in the CP TM_{21} mode, increasing the dielectric permittivity of the substrate the first term becomes increasingly dominant. In the case of a circular polarized TM_{nm} mode we can thus consider only the term proportional to $e^{-j(n-1)\varphi}$ that corresponds to an EM field carrying an OAM of order n-1.

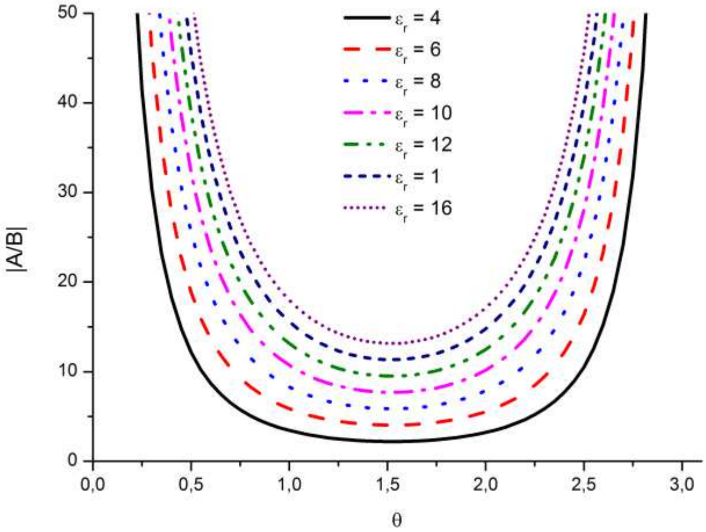

Fig. 38: Ratio between the amplitude of the terms A and B in the case of a circular patch antenna working in a CP TM_{21} mode for different values of substrate permittivity.

Therefore, for the first resonant mode of a circular patch antenna (TM_{11}) the OAM is equal to zero. However, for the higher order modes with $n > 1$, the radiated EM field is characterized by a non-zero OAM. This is confirmed by the phase patterns reported in Fig. 92, where we can observe that the electric fields produced by TM_{21} and TM_{31} modes have the rotating phase front expected by a non-zero OAM [21]. On the contrary, the TM_{11} mode has a phase pattern independent of φ, which corresponds to a zero OAM. Moreover, the conical radiation patterns of a circular patch antenna working at higher order modes [20] are also in agreement with the presence of an EM field with non-zero OAM, which has, as another peculiar aspect, an amplitude null in the propagation direction.

Finally, note that, reassessing equation (14)-(16) for a -π/2 phase shift between the two coaxial cables, we obtain a left-handed CP field with a dominant phase term $e^{j(n-1)\varphi}$ and, therefore, an OAM state with an opposite sign.

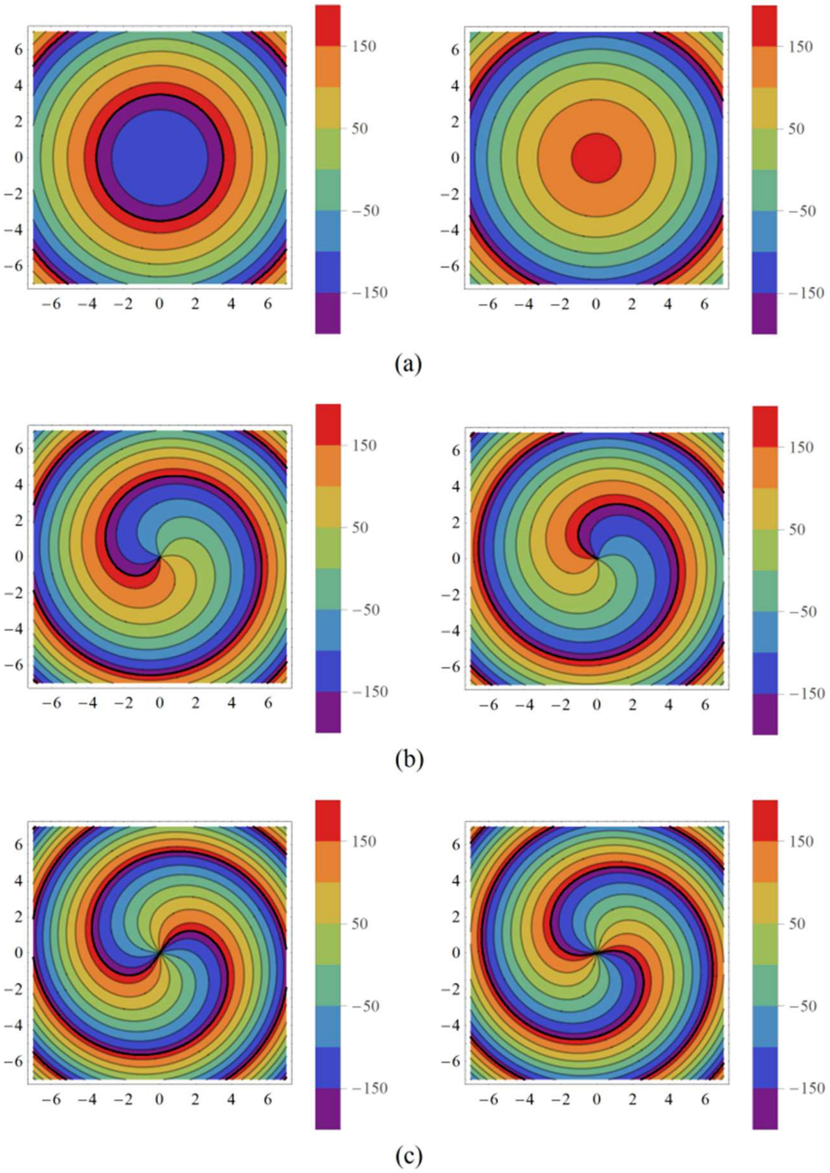

Fig. 39: Phase patterns (in degree) of the x (left) and y (right) component of the radiated electric field in the case of: (a) RHCP TM_{11} mode; (b) RHCP TM_{21} mode; (c) RHCP TM_{31} mode.

2.2 Validation through Full-Wave Numerical Simulations

As analytically shown in the previous Section, the CP TM_{nm} modes of a circular patch antenna radiate an EM field with OAM of order ±(n-1). Such a structure, even if simpler and more compact than those ones proposed in the literature, can be further simplified. In fact, circular polarization can be obtained also through a single coaxial feed. A possible solution consists of introducing a proper asymmetry in the geometrical structure in such a way that two degenerate modes are excited [22]-[23].

Therefore, in order to obtain a patch antenna with a single feed that generates OAM states, we have transformed the circular patch into an elliptical one, as shown in Fig. 93.

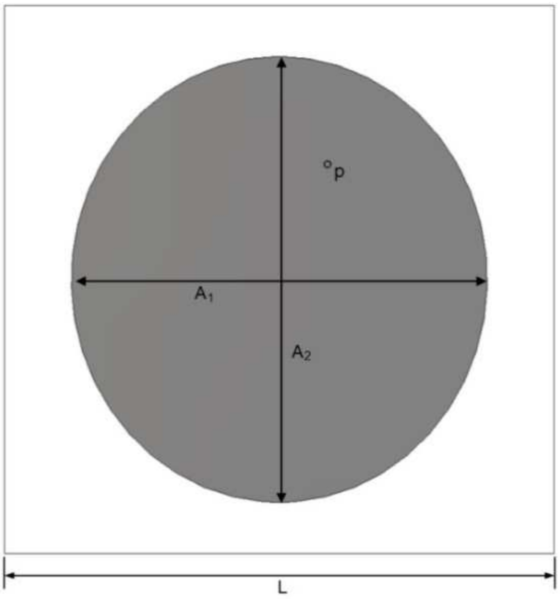

Fig. 40: Top view of the elliptical patch antenna. The inner conductor of the coaxial cable is connected to the point p (x = 8.75 mm; y = 21 mm). The origin of the reference system is at the shape centre. Antenna dimensions are: A_1 = 75,2 mm, A_2 = 81.6 mm, and L = 100 mm.

The elliptical metallic patch is placed on a square 0.787 mm thick Rogers Duroid^{TM} RT5870 ($\varepsilon_r = 2.33$, $\tan\delta = 0.0012$). The dimensions of the two main axes of the elliptical patch have been properly chosen to obtain two almost overlapped resonant frequencies and, therefore, a CP TM_{21} mode around 2.4 GHz. Moreover, the 50 Ω coaxial cable has been properly positioned to obtain a good impedance matching of the two degenerate modes. The main geometrical dimensions of the structure are reported in Fig 93.

Using the full-wave numerical solver CST Microwave Studio [24], we have simulated the radiating and matching properties of the proposed structure. From Fig. 94 we can see that the proposed antenna is well matched around two slightly different resonant frequencies, as required to generate a circular polarized TM_{21} mode. Furthermore, in order to verify the actual generation of a non-zero OAM, the phase patterns of the x and y components of the radiated electric field are shown in Fig. 95. As readily apparent, these phase patterns have a helical profile with a 2π phase change in one turn, corresponding to a phase term $e^{-j\varphi}$. Therefore, the proposed antenna effectively radiates a circular polarized EM field with an OAM of the first order. This result is also confirmed by the simulated phase of radiation patterns, reported in Fig. 96, that show a spiral variation with the azimuthal angle. Finally, please note that the 3-D directivity pattern, reported in Fig. 97, shows an amplitude null in the propagation direction, as expected due to the helical phase profile.

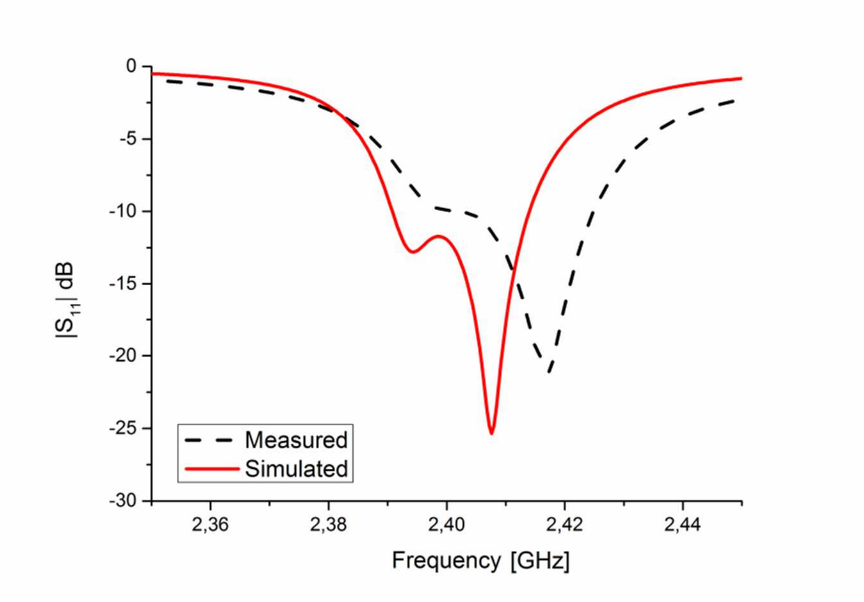

Fig. 41: Simulated (red-solid line) and measured (black-dashed line) reflection coefficient amplitude of the proposed elliptical patch antenna shown in Fig. 93.

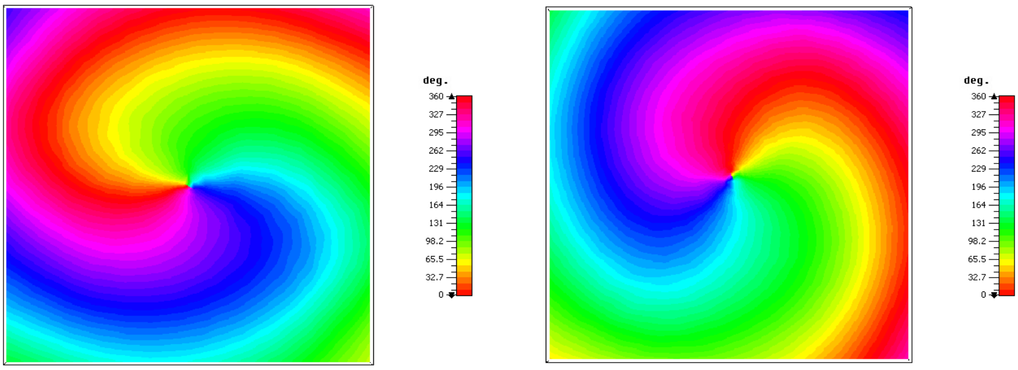

Fig. 42: Phase patterns at 2.4 GHz of the x (left) and y (right) component of the radiated E field by the elliptical patch antenna working in a RHCP TM_{21} mode.

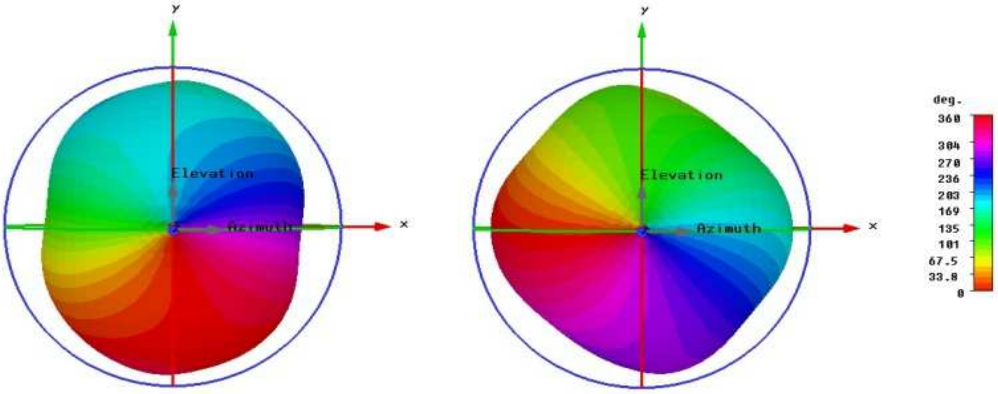

Fig. 43: Simulated Azimuth (left) and Elevation (right) radiation phase patterns at 2.4 GHz of the elliptical patch antenna, shown in Fig. 93, working in a RHCP TM_{21} mode.

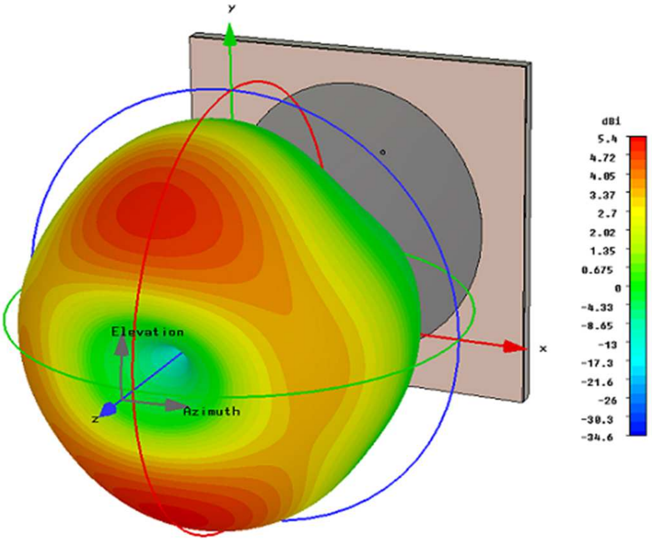

Fig. 44: 3-D directivity pattern at 2.4 GHz of the antenna shown in Fig. 93.

2.3 Experimental Realization and Measurements

The proposed antenna with the dimensions given in Fig. 93 has been manufactured with a LPKF Protomat-S milling machine. An SMA connector with characteristic impedance of 50 Ω has been used to feed the prototype antenna (see Fig. 98). Then, the matching and radiating properties have been measured by using a vector network analyzer and a near-field antenna measurement system.

The measured magnitude of the S_{11} parameter, reported in Fig. 94, is in good agreement with the simulated one. In particular, the antenna is well matched around 2.41 GHz and shows two almost overlapped resonant frequencies. The slight shift in frequency between the simulated and measured results, due to manufacturing tolerances, does not affect the antenna operation and the proof of concept we wanted to give. In fact, the far-field phase patterns of the elevation and azimuth components at 2.4 GHz, reported in Fig. 99, show the expected helical profile of the OAM of the first order.

These results, thus, confirm that an elliptical patch antenna, if properly designed, can be used to generate an EM field with non-zero OAM.

Fig. 45: Photograph showing the realized elliptical patch antenna with the dimensions given in Fig. 93.

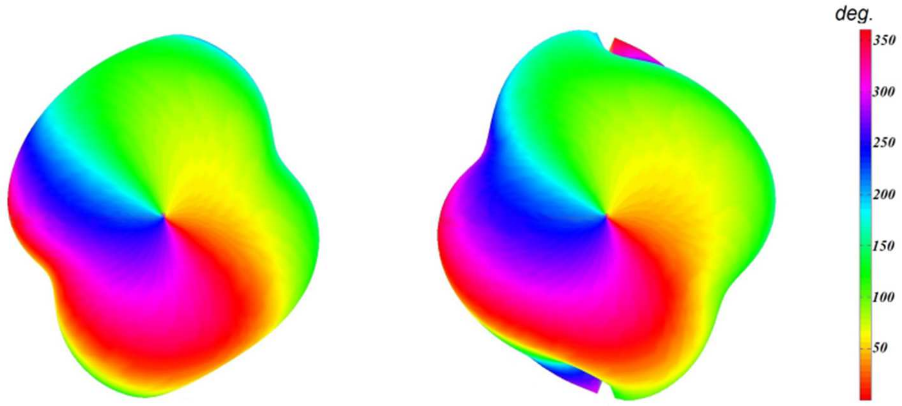

Fig. 46: Measured Azimuth (left) and Elevation (right) radiation phase patterns at 2.4 GHz of the prototype shown in Fig. 98.

2.4 Summary

In this Chapter, we have presented a novel approach to generate an EM field with non-zero OAM at microwave frequencies. At first, we have analytically studied the EM field produced by a circular patch antenna in order to show that a CP TM_{nm} mode generates an OAM of order ±(n-1). For this purpose, the circular patch antenna can be excited with two properly spaced coaxial cables with the same signal amplitudes but with a $\pm\pi/2$ phase shift.

Then, we have shown that an EM field with non-zero OAM can be also generated with a single coaxial feed by using an elliptical patch antenna. In fact, the geometrical asymmetry of this structure allows generating two orthogonal modes that produce a CP EM field. In particular, we have designed an elliptical patch antenna working in a RHCP TM_{21} mode. By using CST Microwave Studio, we have numerically demonstrated that this structure radiates a RHCP EM field with an OAM of the first order around 2.4 GHz.

Finally, we have realized and tested a prototype of the proposed elliptical patch antenna and the measured results validate the predicted characteristics. The final message is that a standard patch antenna, if properly designed, can be employed to generate OAM states. Compared to the other solutions already proposed in the literature, based on either antenna arrays or complex reflector antennas, the proposed one is cheaper, lighter, and more compact.

2.5 References

[1] M. Padgett, and L. Allen, “Light with a twist in its tail,” Contemp. Phys., vol. 41, pp. 275-285, 2000.

[2] J. P. Torres, and L. Torner, Twisted Photons: Applications of Light with Orbital Angular Momentum. Wiley-VCH, 2011.

[3] A. M. Yao and M. J. Padgett, “Orbital angular momentum: origins, behavior and applications,” Adv. Opt. Photon., vol. 3, pp. 161–204, 2011.

[4] Y.S. Jiang, Y.T. He, and F. Li, “Electromagnetic Orbital Angular Momentum in Remote Sensing,” PIERS Proceedings, Moscow, Russia, August 18-21, 2009.

[5] B. Thidé,H. Then, J. Sjöholm,K. Palmer, J. Bergman, T.D. Carozzi, Y. N. Istomin, N. H. Ibragimov, and R. Khamitova, “Utilization of photon orbital angular momentum in the low-frequency radio domain,” Phys. Rev. Lett., vol. 99, no. 8, pp. 087701-1–087701-4, Aug. 2007.

[6] S. M. Mohammadi, L. K. S. Daldorff, J. E. S. Bergman, R. L. Karlsson, B. Thide, K. Forozesh, T. D. Carozzi, and B. Isham, “Orbital angular momentum in radio—a system study,” IEEE Trans. Antennas Propag., vol. 58, pp. 565–572, 2010.

[7] A. Tennant, and B. Allen, “Generation of OAM radio waves using circular time-switched array antenna,” Electron. Lett., vol. 48, pp. 1365–1366, 2012.

[8] F. Tamburini, E. Mari, B. Thide´, C. Barbieri, and F. Romanato, “Experimental verification of photon angular momentum and vorticity with radio techniques,” Appl. Phys. Lett., vol. 99, pp. 204102-1-204102-3, 2011.

[9] F. Tamburini, E. Mari, A. Sponselli, F. Romanato, B. Thidé, A. Bianchini, L. Palmieri, and C. G. Someda, “Encoding many channels in the same frequency through radio vorticity: first experimental test,” New J. Phys., vol. 14, pp. 033001, 2012.

[10] M. Harris, C. A. Hill and J. M. Vaughan, “Optical Helices and Spiral Interference Fringes,” Optics Comm., vol. 106, pp. 161-166, 1994.

[11] M.W. Beijersbergen, R.P.C. Coerwinkel, M. Kristensen, and J.P. Woerdman, “Helical-Wavefront Laser Beams Produced with a Spiral Phaseplate,” Optics. Comm., vol. 112, pp. 321-327, 1994.

[12] O. Edfos, and A.J. Johansson, “Is orbital angular momentum (OAM) based radio communication an unexploited area?,” IEEE Trans. Antennas Propag., vol. 60, pp. 1126–1131, 2012.

[13] N. Uribe-Patarroyo, A. Fraine, D. Simon, O. Minaeva and A. Sergienko, “Object Identification Using Correlated Orbital Angular Momentum (OAM) States,” in Frontiers in Optics, Rochester, NY, USA, 2012.

[14] D. M. Pozar, “Microstrip antennas,” Proc. IEEE, vol. 80, pp. 79-91, 1992.

[15] Y.J. Wang, and C.K. Lee, “Compact and broadband microstrip patch antenna for the 3G IMT-2000 handsets applying styrofoam and shorting-posts,” Progress in Electromagnetics Research, vol. 47, pp. 75-85, 2004.

[16] F. Bilotti, and C. Vegni, “Design of polygonal patch antennas for portable devices,” Progress in Electromagnetics Research, vol. 24, pp. 33-47, 2010.

[17] M.T. Islam, M.N. Shakib, and N. Misran, “Broadband E-H shaped microstrip patch antenna for wireless systems,” Progress in Electromagnetics Research, vol. 98, pp. 163-173, 2009.

[18] M. Barbuto, F. Bilotti, and A. Toscano, “Design of a multifunctional SRR-loaded printed monopole antenna,” Int. J. RF Microw. CAE, vol. 22, pp. 552-557, 2012.

[19] A.G. Derneryd, “Analysis of the microstrip disk antenna element,” IEEE Trans. Antennas Propagat., vol. 27, pp. 660–664, 1979.

[20] J. Huang, “Circularly polarized conical patterns from cicular microstrip antennas,” IEEE Trans. Antennas Propagat., vol. 32, pp. 991–994, 1984.

[21] J. Courtial, D. A. Robertson, K. Dholakia, L. Allen, and M. J. Padgett, “Rotational frequency shift of a light beam,” Phys. Rev. Lett., vol. 81, pp. 4828–4830, 1998.

[22] Y.T. Lo, and W.F. Richards, “Perturbation approach to design of circularly polarized microstrip antennas,” Electron. Lett., vol. 17, pp. 383–385, 1981.

[23] B. Du, and E. Yung, “A single-feed TM21-mode circular patch antenna with circular polarization,” Microw. Opt. Technol. Lett., vol. 33, pp. 154–156, 2002.

[24] CST Studio Suite 2012, CST Computer Simulation Technology AG, Available at: www.cst.com.

Chapter 3

Horn antennas with integrated MTM-inspired filtering modules

Band-pass and band-stop filters are usually employed in the receiver front-end of communication systems in order to improve the performance and increase the signal-to-noise ratio. In fact, since wideband communication systems use a large portion of the electromagnetic spectrum, the performance of the receiver front-end is typically affected by the interfering signals generated by other services operating in a narrower portion of the same frequency band. On the other hand, narrowband receiving systems have to discriminate the desired signal from the out-of-band noise. Therefore, depending on the communication system and the relative operating environment, proper filtering modules with band-pass or band-stop characteristics should be inserted between the antenna and the receiver front-end, resulting in increased complexity, size, weight and cost of the overall system.

One possible solution to solve the problem is to employ a filtering antenna, or *filtenna*, which integrates the radiating element and the filter in a single module [1]-[7].

In the past few years, several configurations have been proposed to design both microstrip and horn antennas with a filtering behavior. In particular, for patch antennas a multitude of both band-pass and band-stop configurations (see, for instance, [4]-[7]) have been proposed. On the contrary, in the case of filtering horn antennas only few band-pass modules have been presented [1]-[3].

In this Chapter, in order to obtain proper horn filtennas with band-stop or band-pass operation, we introduce a novel approach, based on the use of MTM-inspired resonators. In particular, we show that, by properly placing a MTM-inspired resonator inside a standard horn antenna, the radiating and matching properties of the overall structure are affected by the strong resonance of the inclusion leading to a band notch or a band-pass behavior around its resonant frequency.

The structure of the Chapter is as follows. In Section 1, we introduce linear-to-circular polarization transformer technique; in Section 2, we present the design of a 2D linear-to-circular polarization transformer that consisting of complementary electrically small resonators etched on a metallic sheet in existing radiation systems to change their polarization and reduce impedance bandwidth of a standard horn antenna. Finally, in Section 3, we present a filtering module with an opposite behavior (a notched-band), which can be inserted inside horn antennas to limit their receiving properties around the operating frequency of a narrow-band interfering signal.

3.1 Linear-to-Circular Polarization Transformer

In the last years there has been a great interest in a physical phenomenon known as "enhanced transmission" through sub-wavelength single apertures drilled in a metallic plate, at both microwave and optical frequencies. As theoretically reported in [8], in the case of an electrically small circular aperture of radius a in a perfectly conducting metallic screen of zero thickness, transmission is negligible and goes as the fourth power of the ratio a/λ_0. In the last decade, however, several approaches have been proposed to overcome this limit. The first technique is based on the excitation of perturbed leaky-modes by corrugating the metallic surface around the hole with periodic grooves and properly choosing the corrugation period to obtain a reasonable coupling with the radiation impinging on the screen [9]. An alternative approach, exploiting again the properties of perturbed leaky-wave resonances, is proposed in [10]. In that setup, the extraordinary transmission is obtained by placing on the two sides of the aperture, MTM covers characterized by near-zero values of either permittivity or permeability, depending on the polarization of the impinging radiation. Better performances have been achieved by using conjugate-matched single-negative MTM bi-layers on the two opposite faces of the screen, allowing the reduction of the cover thickness. Then, in order to reduce the transverse dimensions of the cover, a new setup exploiting the resonances localized at the interface between conjugate-matched single-negative MTM has been proposed. In that case, the transverse extension of the cover is comparable to the hole dimension. Following this approach, a new setup has been recently proposed, consisting in a properly excited SRR placed in front of the aperture [11]. The physical reason behind the operation of this device is that the strong magnetic resonance of the SRR allows increasing the magnetic dipole representing the aperture [8], leading, thus, to the enhanced transmission phenomenon.

Recently, it has been shown that by placing two identical resonators at the two opposite faces of the aperture and connecting them through metallic strips [12], power extraction from the aperture can be further improved. Though any resonant element is in principle useful to achieve an efficient power transmission, sub-wavelength resonators represent the best candidates in order to keep the space occupancy of the whole structure at a minimum.

However, these setups consist of resonators that can be effectively excited by a single polarization only and, then, they cannot transmit the other polarization beyond the screen.

In this Section, we show that a new setup based on the circular-polarized electrically small antennas proposed in [13], can be used to change the polarization of a field propagating in a circular waveguide from linear to circular. The proposed setup can be considered as a linear-to-circular polarization transformer and can be used to adapt existing radiation systems to work in different environments and operate for different services.

3.2 A Combined Band-pass Filter and Polarization Transformer for Horn Antennas

3.2.1 DESIGN OF A PLANAR LINEAR-TO-CIRCULAR POLARIZATION TRANSFORMER

In previous Section, a linear-to-circular polarization transformer has been proposed based on the use of a MTM-inspired electrically small antenna. However, this setup is not planar, consists of different and geometrically orthogonal structures, involves the use of dielectric materials leading to an efficiency reduction, and can handle only low-power signals (i.e. the operation is limited to the receiving mode only). In order to overcome these issues, we propose here a new approach to design a planar and all-metallic polarization transformer inspired to the compact waveguide filter presented in [15] consisting of a complementary SRR drilled in a metallic sheet. However, since this resonator type inherently works for a single polarization only, in order to design a linear-to-circular polarization transformer, we need to replace it with an element showing different polarization properties.

In this regard, we propose the design of a different resonator using a complementary version of the one used in [16] to design a circularly polarized electrically small antenna. In particular, as shown in Fig. 43, we have drilled on a metallic sheet two mutually orthogonal meander-line slot dipoles. As well explained in [16], in order to obtain a circular polarization operation, the two dipoles are terminated with arrows that have slightly different dimensions in such a way that the phase shift between them is equal to $\pi / 2$.

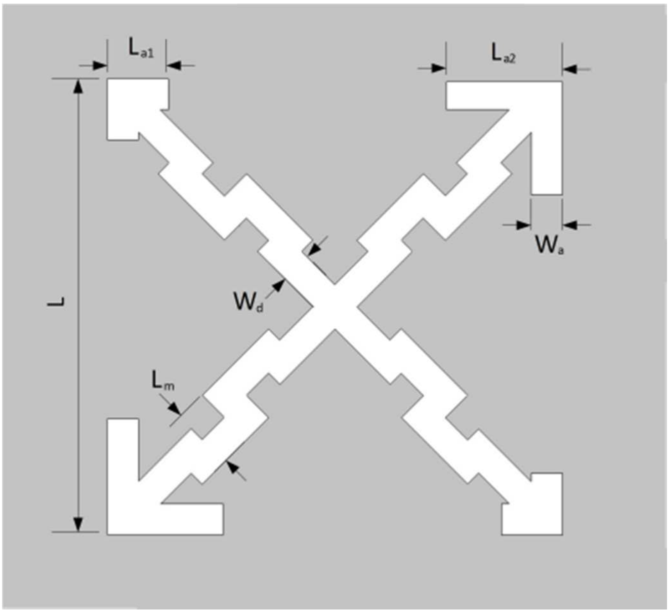

Fig. 47: Geometrical sketch of the proposed polarization transformer with dimensions: L = 5.8 mm, L_{a1} = 0.3 mm, L_{a2} = 0.9 mm, L_m = 0.8 mm, W_d = 0.4 mm, W_a = 0.4 mm.

In this way, a vertical or horizontal linearly polarized electromagnetic field impinging on one side of the screen can excite the complementary resonator etched on the screen. The two dipoles radiate on the other side of the screen, obtaining, thus, an emerging circularly polarized field beyond it.

In order to validate this idea, we have numerically simulated the behavior of the structure reported in Fig. 44, consisting of an open-ended linearly polarized rectangular waveguide (WR-62) capped with the proposed polarization transformer. The dimensions of the resonators are reported in Fig. 43.

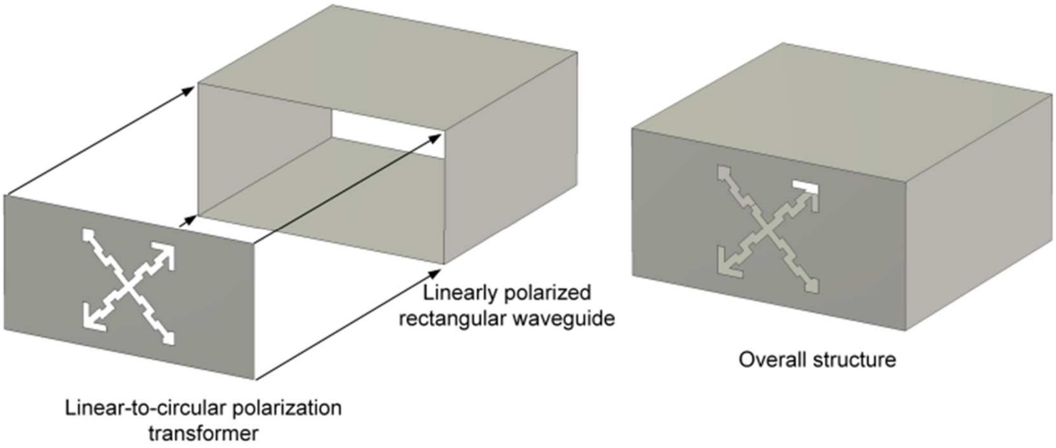

Fig. 48: Geometrical sketch of the proposed polarization transformer and its integration with a linearly polarized rectangular waveguide.

By using the full-wave simulator CST Microwave Studio, we have compared the matching and radiating properties of a regular open-ended rectangular waveguide with the ones of the structure shown in Fig 44. As shown in Fig. 45, the proposed setup exhibits a good impedance matching around the resonant frequency of the resonator and a narrower bandwidth compared to the one of a regular rectangular open-ended waveguide.

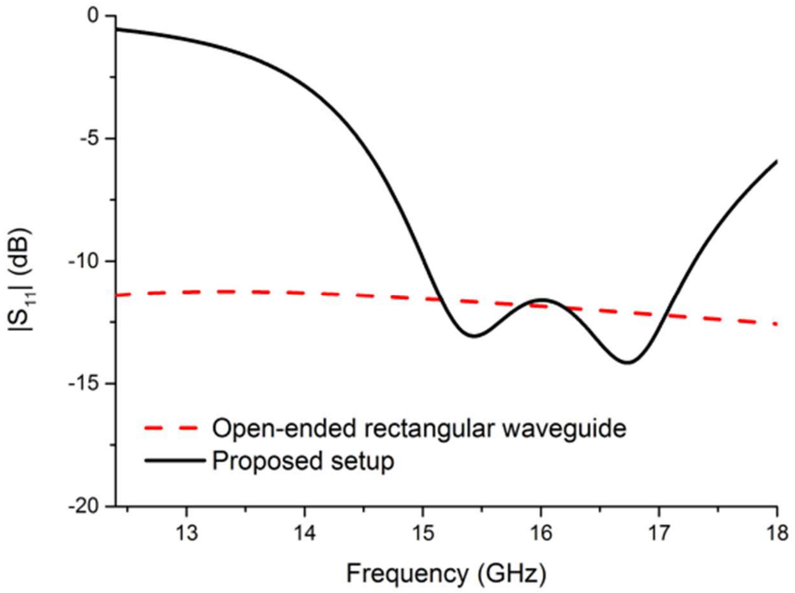

Fig. 49: Reflection coefficient amplitude of an open ended rectangular waveguide (dashed line) and of the structure shown in Fig. 44 (solid line).

Fig. 46 shows the simulated gain patterns on the two principal planes at the central frequency 15.75 GHz for both polarizations, respectively. The axial ratio in the main beam direction, shown in Fig. 47, is below 3 dB around 15.75 GHz with a bandwidth of about 625 MHz. These results confirm the effectiveness of the proposed structure to transform an impinging linear polarization into a circular one.

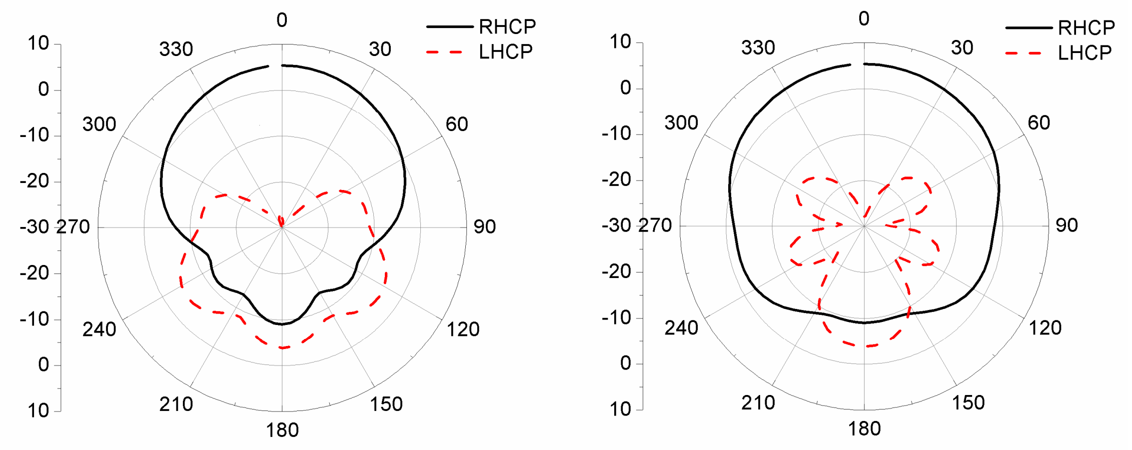

Fig. 50: Realized gain patterns at 15.75 GHz of the structure shown in Fig. 44: (left) φ = 0°; (right) φ = 90°.

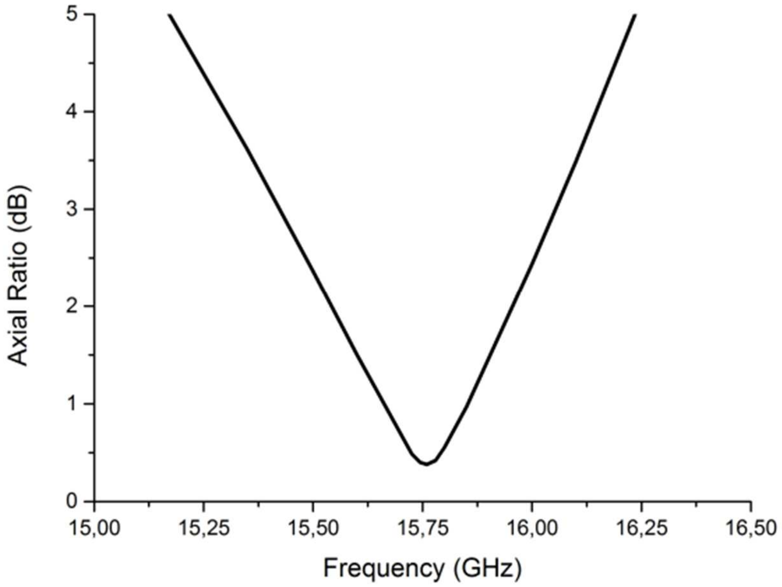

Fig. 51: Axial ratio for the main beam direction of the structure shown in Fig. 44.

3.2.2 DESIGN OF THE SELF-FILTERING CIRCULARLY POLARIZED HORN ANTENNA

In the previous Subsection, we have presented a novel linear-to-circular polarization transformer based on the employment of a complementary resonator. This setup, thanks to its compact size and the independence of its features from the surrounding environment, can be easily integrated in a regular radiation element to change its polarization properties. Moreover, as shown in Fig. 45, a regular waveguide capped by the proposed polarization transformer exhibits a narrow operation bandwidth. This feature, which is typically regarded as a limitation in most of MTM-inspired devices, can be useful to reduce the out-of-band noise in satellite receiving systems.

Exploiting this concept, we present in this section a self-filtering circularly polarized horn antenna that can be used as the feed of regular parabolas for narrowband satellite systems. The proposed structure is shown in Fig. 48, and consists of a WR-62 waveguide, a regular corrugated conical horn and the proposed polarization transformer placed between the waveguide and the horn.

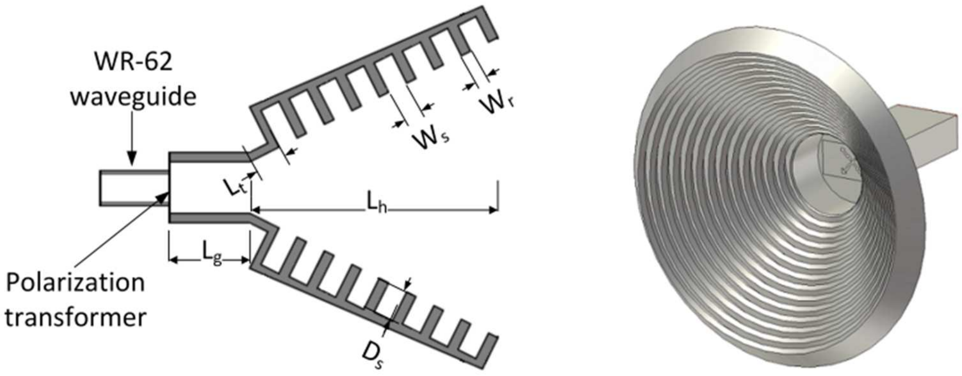

Fig. 52: Side view (left) and perspective view (right) of the filtering circularly polarized horn antenna. Corrugated horn dimensions: D_s = 6.3 mm, L_g = 33 mm, L_h = 25.6 mm, L_t = 5 mm, W_s = 1.3 mm, W_r = 1.3 mm.

The radiating and matching properties of this structure have been numerically evaluated by using CST Microwave Studio. The reflection coefficient amplitude as well as the axial ratio, shown in Figs. 49 and 50, respectively, is very similar to the ones presented in the previous Subsection, proving the independence of the inclusion from the environment. In fact, in order to maintain the AR below 3 dB, we used the following value for the length of one of the arrows: L_{a2} = 0.8 mm; while all other dimensions of the inclusion are those given in Fig. 42. In particular, the antenna is well matched only in a narrow frequency band around the resonant frequency of the complementary resonator. In this way, the unwanted signals are directly reflected back and do not reach the receiver, while the in-band signal is efficiently received by the antenna.

Moreover, the plot of the axial ratio (shown in Fig. 50), which is below 3 dB around 15.85 GHz, proves that the proposed antenna can be used in satellite systems requiring circular polarization. The radiation patterns on the principal planes at the central frequency of 15.85 GHz are reported in Fig. 51 and show that a right-handed circular polarized (RHCP) field is radiated with a maximum realized gain greater than 14 dBi.

Finally, the realized gain and the directivity of the proposed horn are shown in Fig. 52 as a function of frequency. This figure confirms that, due to the mismatch introduced by the polarization transformer, the proposed setup efficiently radiates/receives only in a narrow frequency band. Please note that, compared to the self-filtering horn antennas presented in the literature, the proposed one is less complex, lighter, and less expensive.

In fact, the combined band-pass filter and polarization transformer simply consists of a single metal sheet with a slot of suitable geometry.

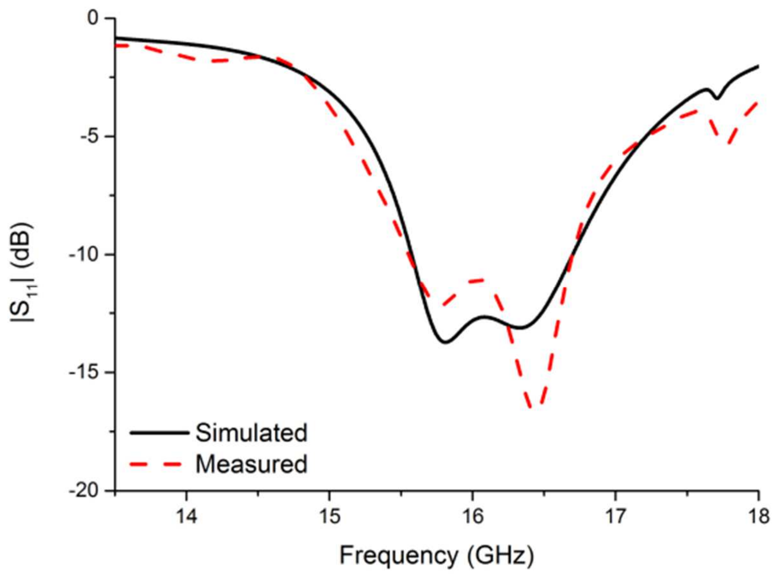

Fig. 53: Simulated and measured reflection coefficient amplitude of the self-filtering circularly polarized horn antenna shown in Fig. 48.

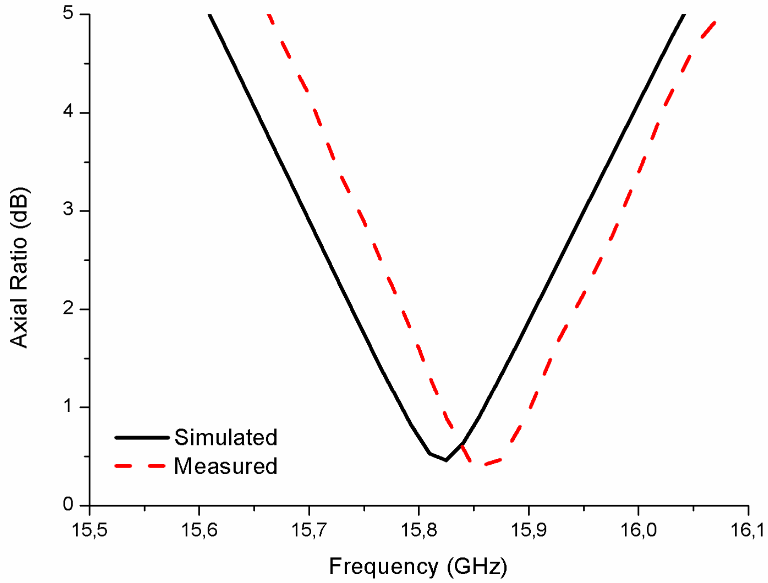

Fig. 54: Simulated and measured axial ratio for the main beam direction of the self-filtering circularly polarized horn antenna shown in Fig. 48.

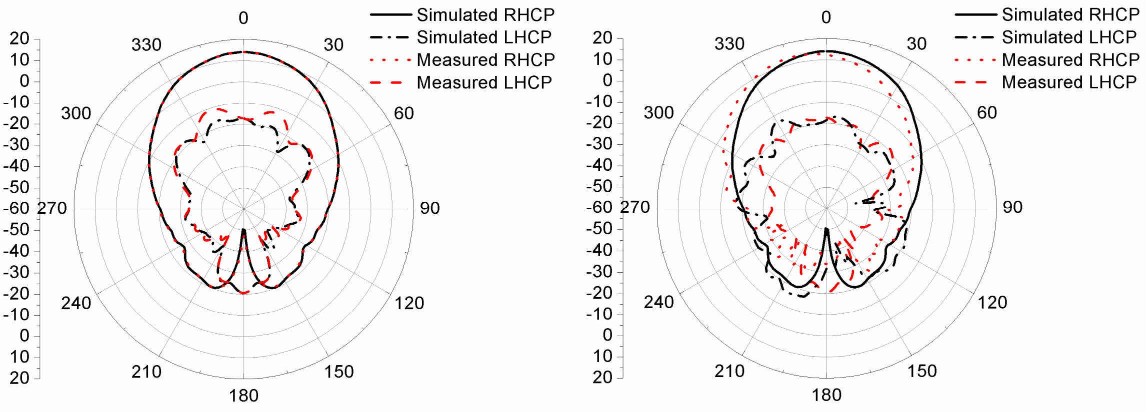

Fig. 55: Simulated and measured realized gain patterns at 15.85 GHz of the self-filtering circularly polarized horn antenna shown in Fig. 48: (left) φ = 0°; (right) φ = 90°.

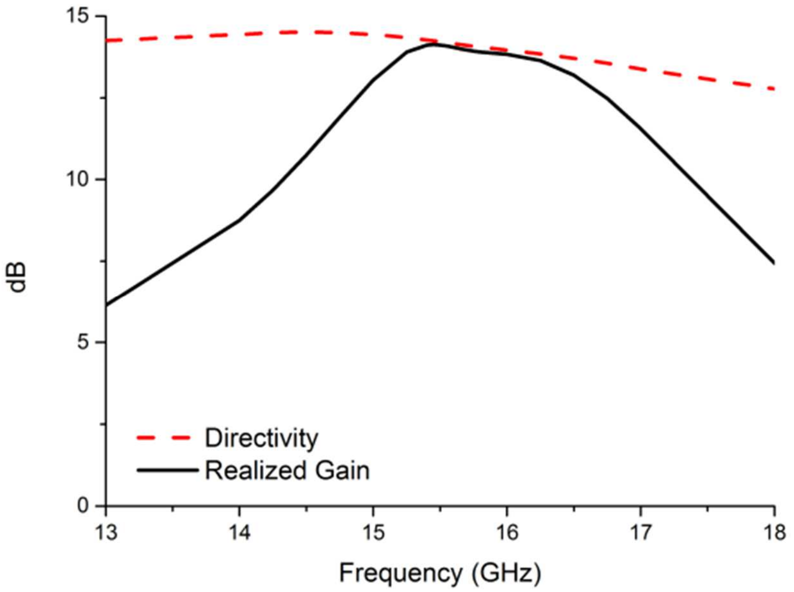

Fig. 56: Realized gain (solid line) and directivity (dashed line) of the self-filtering circularly polarized horn antenna shown in Fig. 48.

3.2.3 EXPERIMENTAL REALIZATION AND MEASUREMENTS

In order to validate the numerical results reported in the previous Subsection, we have realized the proposed polarization transformer and assembled the overall structure, as shown in Fig 53. In particular, a polarization transformer with the same dimensions reported in Subsection 2 has been realized on a 0.1 mm thick copper foil using the LPKF Protomat-S milling machine. This device has been inserted between a WR-62 coaxial-to-waveguide transition and a corrugated conical horn.

The matching and radiating properties, reported in Fig. 49 - Fig. 51, have been measured by using a vector network analyzer and the near field antenna measurement system Satimo StarLab. As predicted by the full-wave simulations, the measurements confirm that the antenna radiates a RHCP field, confirming the expected filtering behavior.

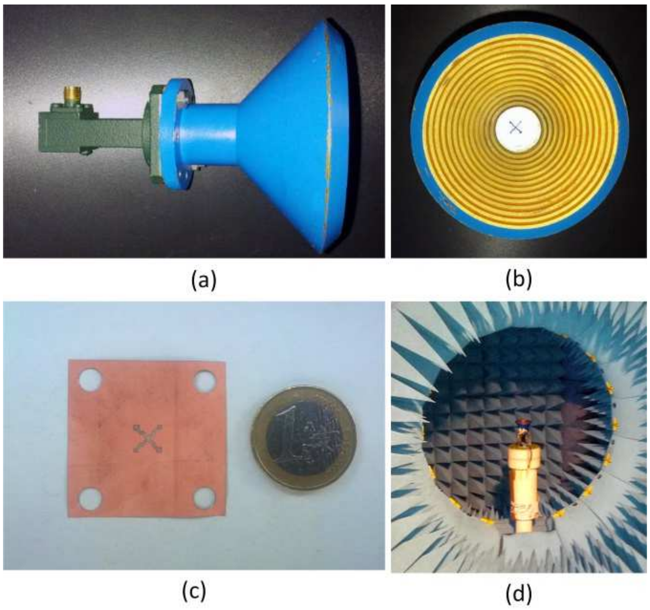
(a) (b) (c) (d)

Fig. 57: Photographs showing: (a) side view of the overall antenna structure consisting of a coaxial-to-waveguide transition, the proposed polarization transformer, and a corrugated conical horn; (b) front view of the overall antenna structure; (c) the realized polarization transformer; (d) the overall antenna structure in the Satimo StarLab.

3.3 Horn Antennas with Integrated Notch Filters

Both the designs proposed in the previous Sections incorporate a band-pass filter that allows reducing the out-of-band noise. However, some wideband communication systems suffer from the interference generated by narrowband services operating in a portion of the same frequency band. In this case, a notch filter rather than a band-pass filter would be needed

In this Subsection, in order to obtain proper horn filtennas with band-stop operation, we propose to use a single SRR placed inside a regular pyramidal horn. In this way, the radiating and matching properties of the overall structure are affected by the strong resonance of the SRR only around its resonant frequency – leading to a band notch – while they are almost unchanged in the rest of the operating frequency band. The dimensions of the SRR can be easily chosen to make the notched-band centered at the frequency of the interfering signal we want to suppress. Moreover, using two or more SRRs, we are able to suppress multiple interfering signals at different frequencies.

3.3.1 DESIGN OF A HORN FILTENNA WITH A SINGLE-BAND-STOP CHARACTERISTIC

3.3.1.1 Overview of the proposed structure

In the previous Sections, exploiting the inherent narrow bandwidth of MTM-inspired resonators, we have proposed radiating elements exhibiting a self-filtering behavior. However, as both approaches involve the insertion of a metallic screen orthogonal to the propagation direction of the electromagnetic field, they can be used only for microwave components exhibiting a band-pass behavior. The series resonance linked to the presence of connected electrically small antennas or complementary resonators, in fact, allows a complete transmission of the energy through the metallic screen in a narrow frequency band centered at the resonant frequency of the resonating structure.

In order to design a horn filtenna with band-stop characteristic, thus, we need to remove the metallic screen and design a proper resonant inclusion that stores/dissipates energy at a given frequency, leading to a band-notch in a narrow frequency range.

For this purpose, we have chosen the SRR that, due to its strong magnetic resonance, can significantly affects the antenna matching properties only around its resonant frequency, while at the other frequencies it weakly interacts with the electromagnetic field inside the horn, without affecting the radiating and matching properties of the overall system.

The entire structure, shown in Fig. 54, consists of a WR-90 waveguide (whose operating frequency range is 8.2 – 12.4 GHz), a regular pyramidal horn and the proposed filtering module. The latter consists of a SRR etched on one side of a Rogers Duroid^{TM} RT5870

(ε_r = 2.33, tan δ = 0.0012) dielectric substrate with a thickness of 0.787 mm. Following the design in [17], the dimensions of the SRR are properly chosen to obtain a resonant frequency at 10 GHz. In particular, the metallization and the capacitive gaps have a width of 0.5 mm, while all the other dimensions are reported in Fig. 54. Please note that the dielectric substrate has been properly shaped in order to facilitate the placement of the filter inside the horn antenna at the appropriate position.

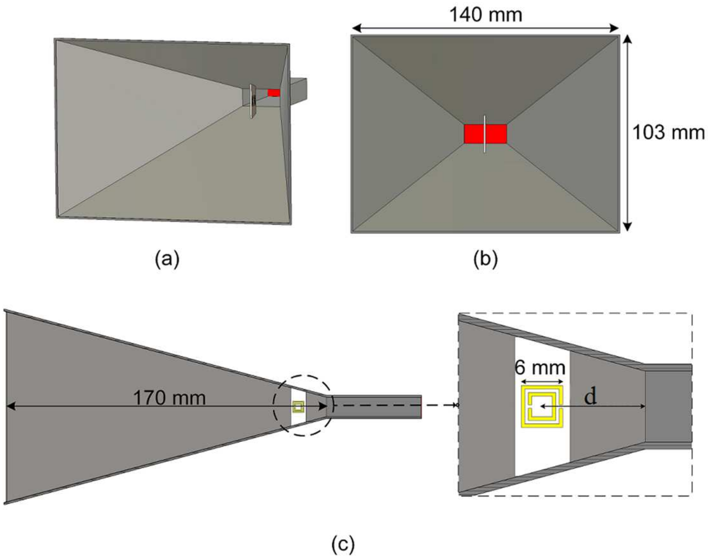

Fig. 58: Geometrical sketch of the proposed horn antenna with the notched-band filter: (a) perspective view; (b) front view; (c) side view.

3.3.1.2 Simulation results

The design of the proposed antenna has been carried out by using the full-wave simulator CST Microwave Studio. Considering the field distribution of the fundamental mode travelling through the waveguide and the horn, we expect that the frequency position of the notched-band depends mainly on the SRR dimensions and the relative permittivity of the dielectric substrate where the resonator is printed on. On the other hand, we expect that the distance *d* between the center of the resonator and the throat of the horn influences the magnitude of the reflection/transmission. In fact, when the SRR is further away from the throat of the horn, it intercepts a progressively lower portion of the impinging power and, thus, the expected reflection at the resonance is progressively lower. These expectations are confirmed by the graphs reported in Fig. 55 showing the frequency variation of the reflection coefficient amplitude at the input port for different values of *d*. The position of the reflection peak is quite stable with the variation of the distance *d*, while the amplitude of the peak is lower for larger values of *d*. In addition, we note that if the SRR is too close to the throat, due to the reactive effects of the discontinuity waveguide-horn, the amplitude of the reflection coefficient is higher in the whole monomodal operation frequency of the horn. Therefore, in order to make a wise design, we have chosen the distance d = 15 mm, which guarantees a strong mismatch in the notched-band and a good impedance matching in the rest of the frequency band. In this way, as reported in Fig. 56, the performance of the horn with and without the filtering module is similar over the whole frequency range, except for the notched part.

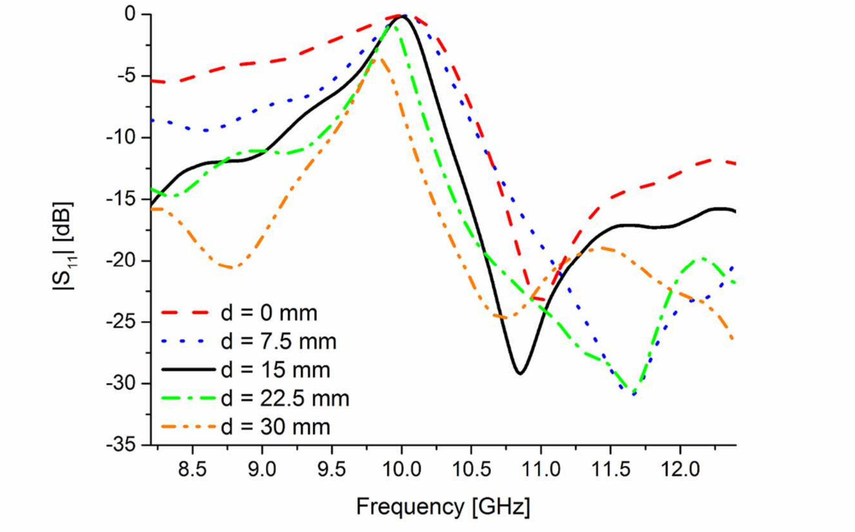

Fig. 59: Reflection coefficient amplitude at the input port of the structure shown in Fig. 54 for different positions of the SRR.

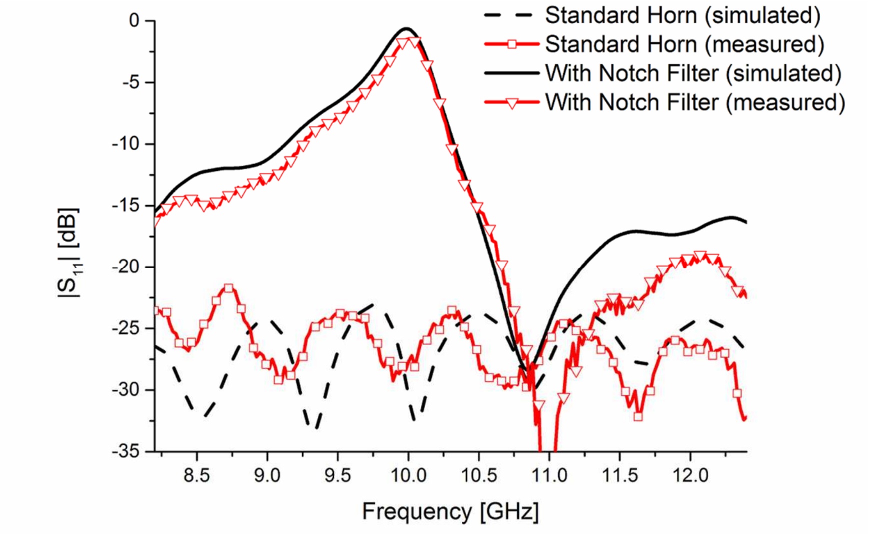

Fig. 60: Measured and simulated reflection coefficient amplitude at the input port of the structure shown in Fig. 54 for the case of d = 15 mm.

The expected filtering behavior of the proposed structure is also confirmed by the values of the broadside gain shown in Fig. 57 and Fig. 58. As expected, in fact, the realized gain is very low within a narrow frequency band around 10 GHz, due to the strong excitation of the SRR. An interfering signal falling in the same frequency range, thus, would not affect the performance of the receiver. On the contrary, in the rest of the frequency band, the radiating properties of the proposed structure are almost identical to the ones of the regular horn.

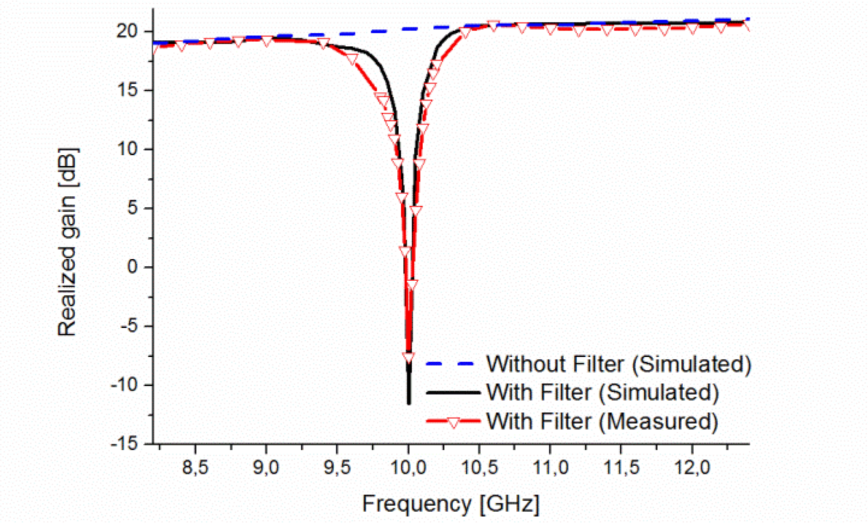

Fig. 61: Measured and simulated realized gain in the main beam direction of the proposed horn antenna with the notched-band filter and of the corresponding standard horn antenna.

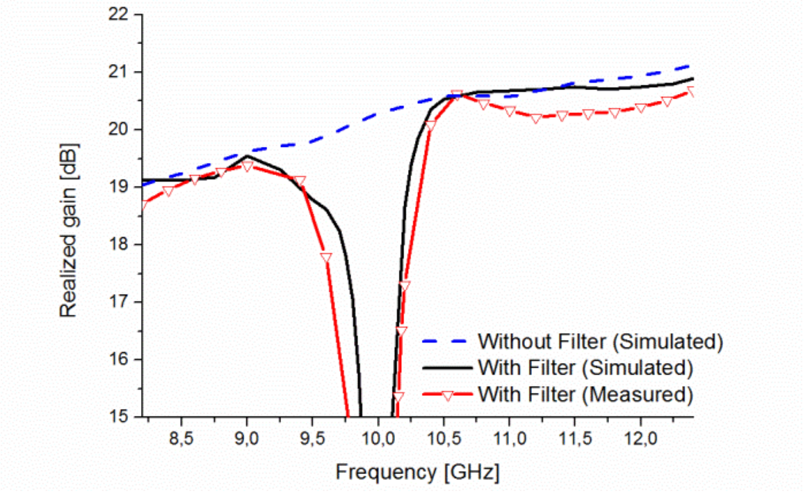

Fig. 62: Close-up of Fig. 57.

In Fig. 59, we also show the realized gain patterns at three sample frequencies. These results confirm that, at 10 GHz, the field is not simply deviated from the broadside direction, but is, indeed, not radiated by the antenna.

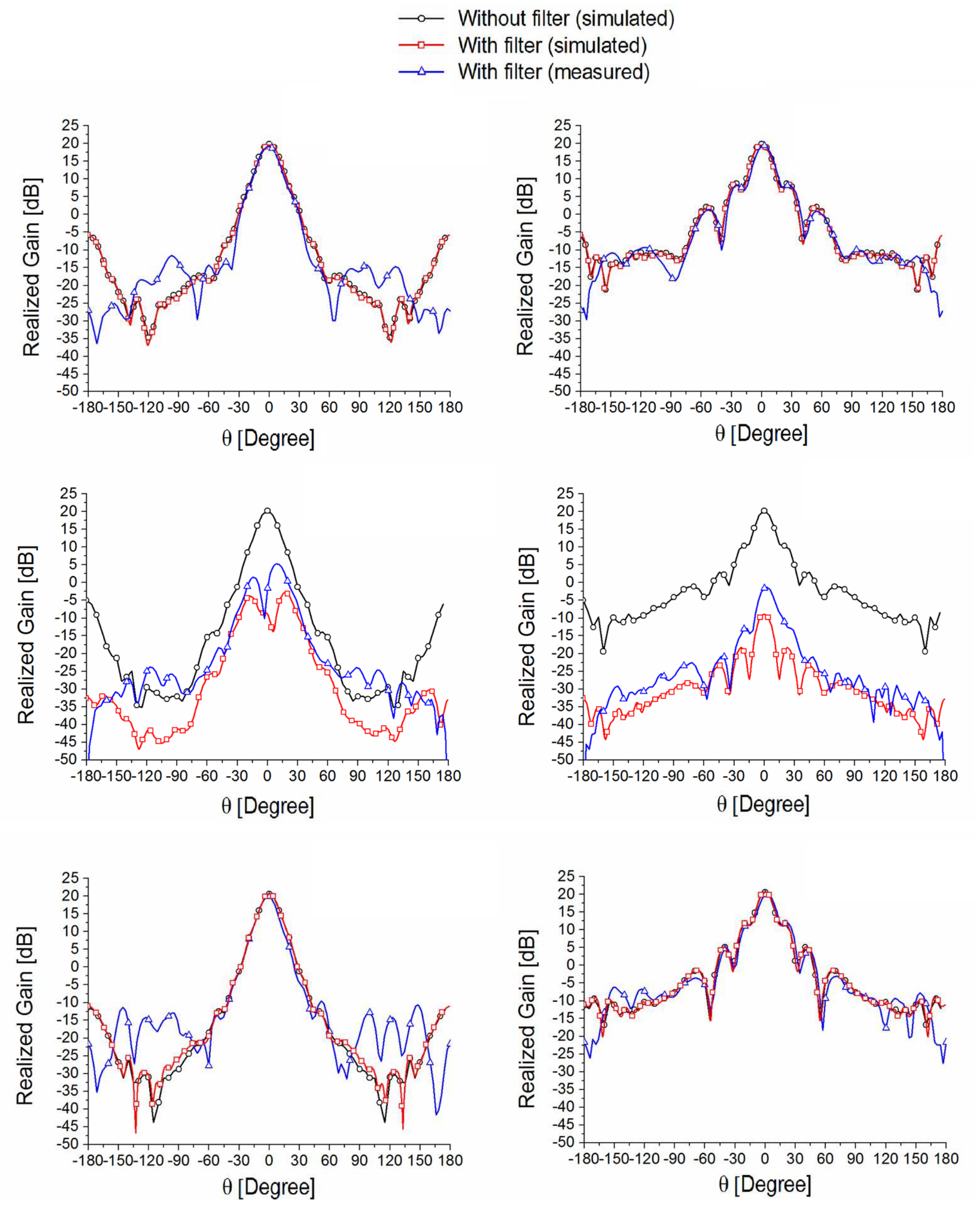

Fig. 63: Simulated and measured realized gain patterns of the proposed horn antenna with and without the notched-band filter on the E-plane (left column) and H-plane (right column) at: (first line) 9 GHz, (second line) 10 GHz and (third line) 11 GHz.

3.3.2 DESIGN OF A HORN FILTENNA WITH A DUAL-BAND-STOP CHARACTERISTIC

By properly designing and positioning a single SRR inside a horn antenna we can obtain a filtenna with a notched-band characteristic. However, many wideband communication systems require more than one notched-band. In order to obtain a horn filtenna with a dual-band behavior, we have etched two SRRs with slightly different dimensions on the same Rogers Duroid^{TM} RT5870 substrate (see Fig. 60) in order to have two almost independent resonant frequencies at 9.25 GHz and 10.75 GHz. The main geometrical dimensions of the structure are reported in Fig 60.

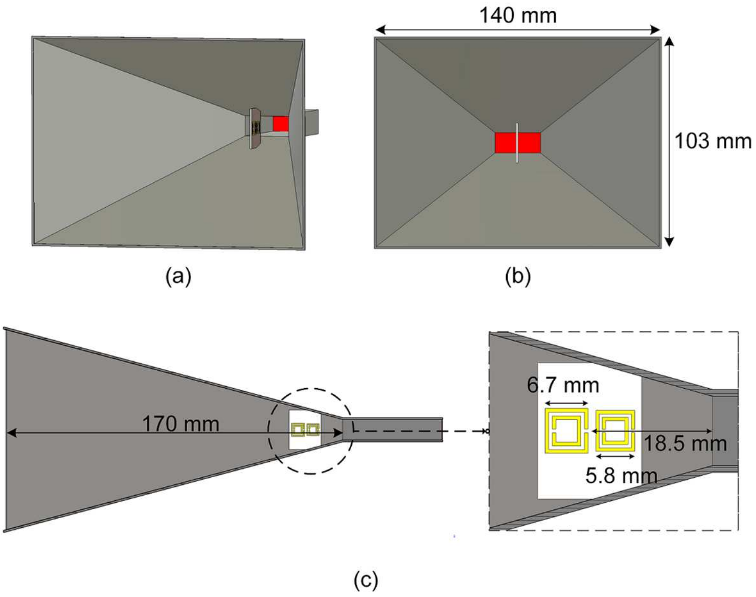

Fig. 64: Geometrical sketch of the proposed horn antenna with the dual-band-notch filter: (a) perspective view; (b) front view; (c) side view.

The simulated results of the matching (i.e. magnitude of the reflection coefficient at the input port) and radiating (i.e. broadside realized gain) properties of the dual-band structure, reported in Figs. 61-63, respectively, confirm the expectations.

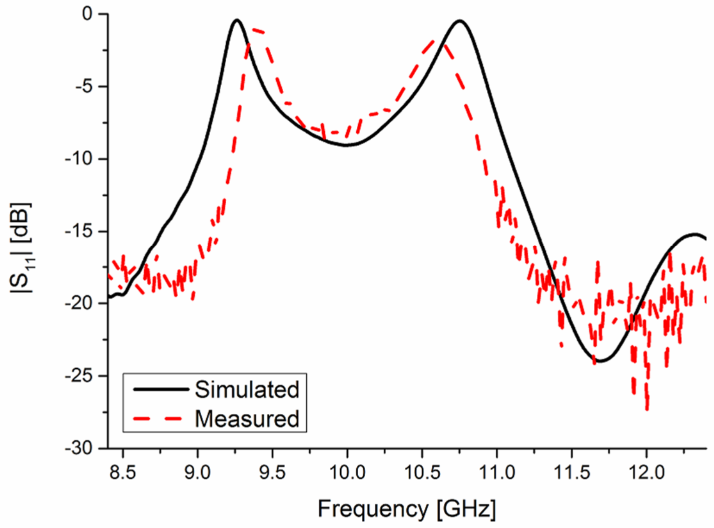

Fig. 65: Simulated and measured reflection coefficient amplitude at the input port of the horn filtenna with a dual band-stop characteristic.

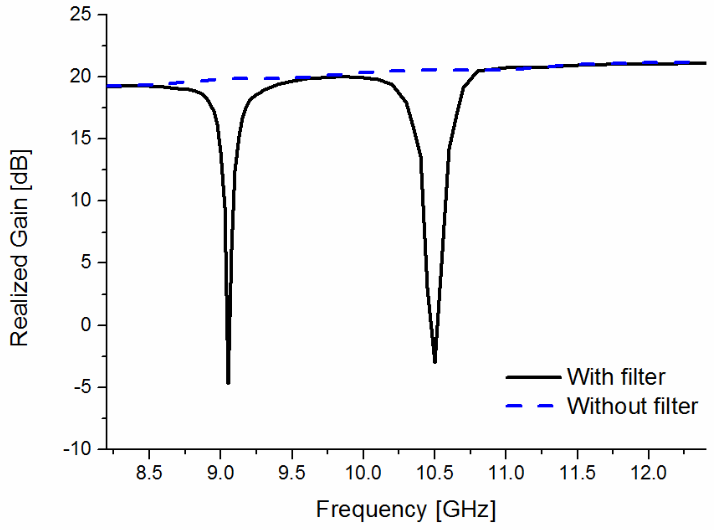

Fig. 66: Simulated realized gain in the main beam direction of the horn antenna with and without a dual-band-stop filter.

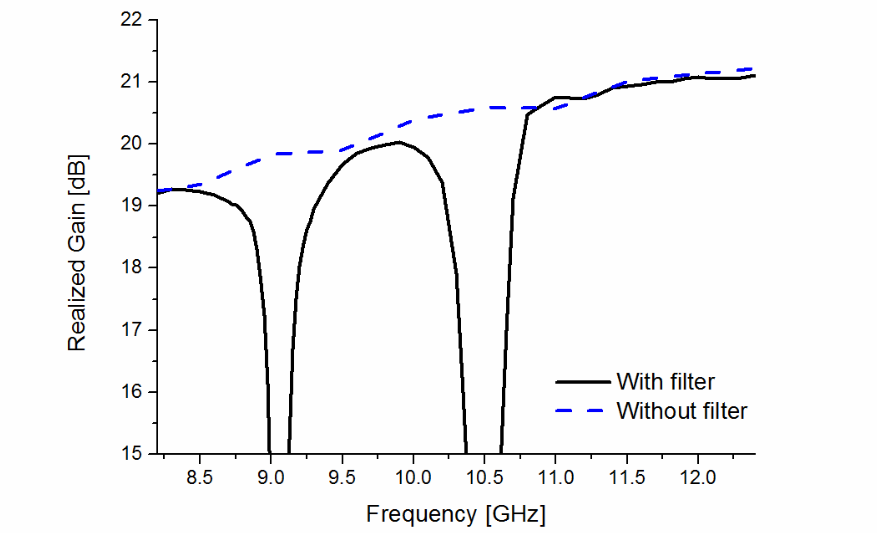

Fig. 67: Close-up of the simulated realized gain in the main beam direction of the horn antenna with and without a dual-band-stop filter.

3.3.3 EXPERIMENTAL REALIZATION AND MEASUREMENTS

In order to validate the proposed approach, the single-band filtering module shown in Fig. 54 has been manufactured with a LPKF Protomat-S milling machine. As shown in Fig. 64, the overall structure has been assembled by using standard foam to properly fix the SRR inside the horn. Finally, the performances of the radiating element have been tested by using a vector network analyzer and a near-field antenna measurement system.

As shown in Fig. 56, the measured amplitude of the reflection coefficient at the input port is in a good agreement with the simulated one. In particular, the antenna has a maximum mismatch at around 10 GHz, while in the rest of the operating bandwidth it exhibits a good impedance matching. The measured realized gain, reported in Fig. 57-58, has the same behavior of the simulated one, showing a minimum of -8 dB at around 10 GHz. In addition, the measured realized gain patterns, shown in Fig. 59, are again in a very good agreement with the simulated one, confirming the effectiveness of the proposed approach.

As a further verification of the previous results, we have also measured the transmission parameters of the setup shown in Fig. 65, where we have used the proposed filtering horn antenna and a standard horn antenna placed at a distance of 60 cm. As shown in Fig. 66, in this case we have a deep minimum of the transmission coefficients at around 10 GHz that, compared to the case of two standard horn antennas, confirms the filtering behavior enabled by the SRR. Moreover, by using two identical versions of the proposed antenna placed again at a distance of 60 cm, we have obtained a further reduction of the transmission due to the filtering behavior of both antennas.

Finally, we have also fabricated and measured the dual-band version simulated in Section 3. In particular, we have measured the reflection coefficient of the overall structure, reported in Fig. 61, which is, again, in a good agreement with the simulated one, confirming the dual-band behavior of the filtering module. These results confirm that, if properly designed, SRRs can be easily integrated inside a standard horn antenna to introduce notched-bands inside the operating bandwidth of the horn itself, without significantly increasing weight, cost, and space occupancy of the overall structure.

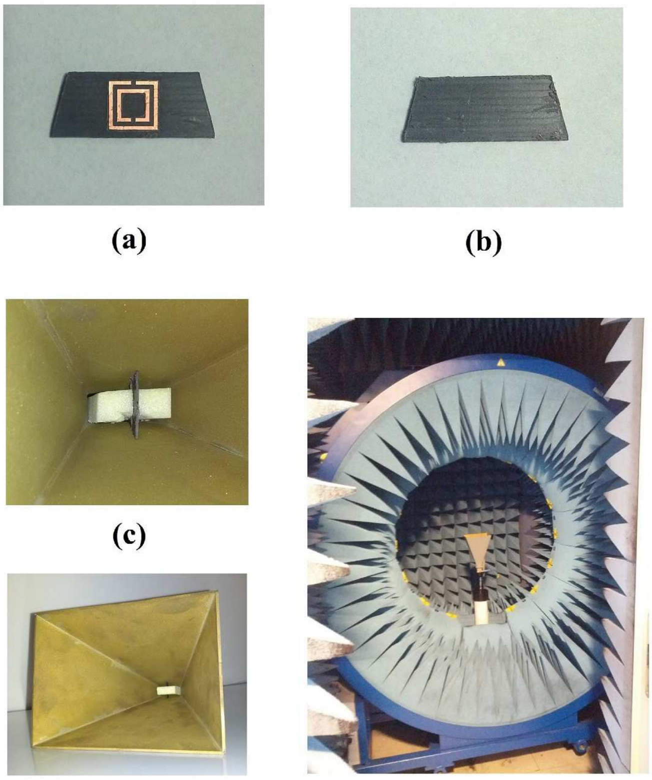

(a) **(b)**

(c)

(d) **(e)**

Fig. 68: Photographs showing: top (a) and bottom (b) views of the realized filtering module; (c) the filtering module fixed in the horn antenna; (d) perspective view of the proposed self-filtering horn antenna; (e) the proposed structure placed inside the near-filed measurement system.

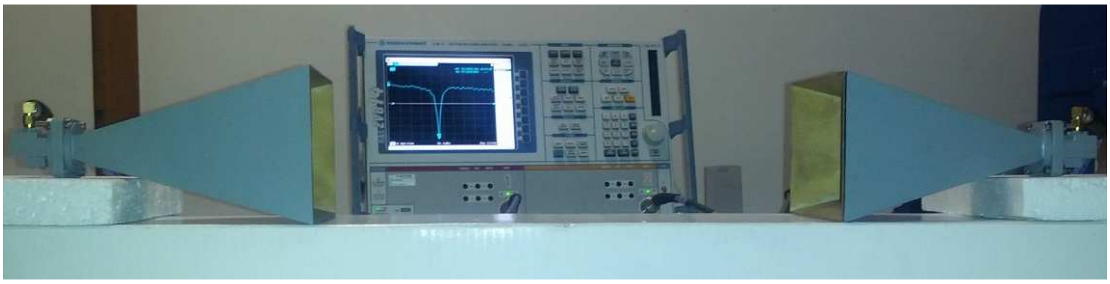

Fig. 69: Photographs showing the transmission measurement setup.

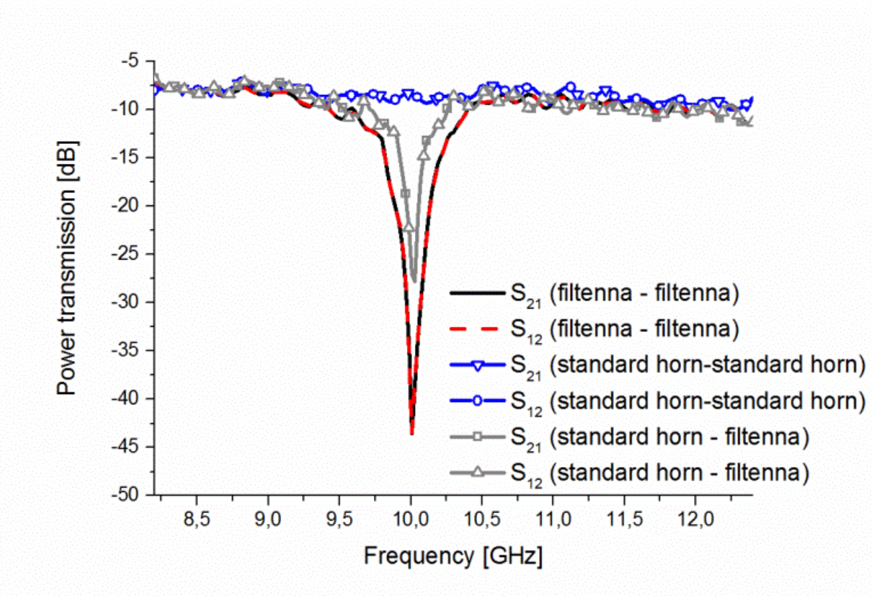

Fig. 70: Power transmission between two single-band filtering horn antennas, two standard horns and between a standard horn and the single-band filtering horn antenna, in the setup shown in Fig. 65.

3.4 Summary

In this Chapter, we have presented a novel class of horn antennas that also performs filtering operations. At first, a polarization transformer can be successfully used to design a self-filtering and circularly polarized horn antenna. In particular, we have inserted the proposed polarization transformer at the section connecting a WR-650 waveguide and a conical horn. By using CST Microwave Studio, we have numerically demonstrated that the overall structure radiates a left-handed circularly polarized electromagnetic field with a maximum realized gain greater than 17 dBi. Moreover, the reflection coefficient is below -10 dB only in a narrow frequency band around the resonant frequency of the resonating particle, which mainly depends on the particle dimensions.

Then, we have presented a circular polarized (CP) filtering antenna consisting of a regular conical horn and a planar and all metallic polarization transformer. The proposed linear-to-circular polarization transformer is obtained by using complementary electrically small resonators etched on a metallic sheet. This structure behaves both as a polarization transformer and a filter allowing to reduce the impedance bandwidth of the conical horn to avoid additional noise in satellite receiving systems. The proposed antenna, operating at X-band, exhibits a CP realized gain of 17.5 dBic.

Finally, we have proposed the design of filtering horn antennas with band-stop characteristics obtained through the use of electrically small magnetic resonators. In particular, a SRR etched on a Rogers Duroid^{TM} RT5870 dielectric substrate is inserted within the metallic flare of the horn at a proper distance from the throat. At around the resonant frequency of the SRR transmission is highly reduced and a single notched-band is obtained. In order to extend the result to dual-band operation, we have also presented the design of the filtering module made by two SRRs with different dimensions.

The validity of the proposed approach is verified through proper sets of full-wave simulations and experiments on fabricated prototypes. The obtained results prove that the proposed antenna can be employed in receiver front-ends of satellite systems to remove the necessity of external filtering modules. Moreover, we remark here that the proposed radiators can be employed in communication platforms, where structural and cost constraints require strong integration of different components. The proposed modules, in fact, allow for a dramatic reduction of the interfering signal power, besides having advantages such as reduced cost, weight, and space occupancy. Finally, the filtering modules can be thought of as a simple add-on to be designed and inserted into already operating horn antennas to suppress interference, when needed.

3.5 References

[1] B. Froppier, Y. Mahe, E.M. Cruz, and S. Toutain, “Design of a filtering antenna: application to the electromagnetic horn,” in IEEE AP-S Symp. Digest, Jun. 2003, vol. 2, pp. 1173-1176.

[2] G.Q. Luo, W. Hong, H.J. Tang, J.X. Chen, X.X. Yin, Z.Q. Kuai, and K. Wu, “Filtenna consisting of horn antenna and substrate integrated waveguide cavity FSS,” IEEE Trans. Antennas Propagat., vol. 55, pp. 92-98, 2007.

[3] F. Bilotti, L. Di Palma, D. Ramaccia, and A. Toscano, “Self-filtering low-noise horn antenna for satellite applications,” IEEE Antennas Wireless Propag. Lett., vol. 11, pp. 354-357, 2012.

[4] C. Yu, W. Hong, Z. Kuai, and H. Wang, “Ku-band linearly polarized omnidirectional planar filtenna,” IEEE Antennas Wireless Propag. Lett., vol. 11, pp. 310-313, 2012.

[5] X. Chen, F. Zhao, L. Yan, and W. Zhang, “A compact filtering antenna with flat gain response within the passband,” IEEE Antennas Wireless Propag. Lett., vol. 12, pp. 857-860, 2013.

[6] M. Naser-Moghadasi, R.A. Sadeghzadeh, T. Sedghi, T. Aribi, and B.S. Virdee, “UWB CPW-fed fractal patch antenna with band-notched function employing folded t-shaped element,” IEEE Antennas Wireless Propag. Lett., vol. 12, pp. 504-507, 2013.

[7] J.Y. Siddiqui, C. Saha, and Y. M.M. Antar, “Compact SRR loaded UWB circular monopole antenna with frequency notch characteristics,” IEEE Trans. Antennas Propagat., vol. 62, pp. 4015-4020, 2014.

[8] H. A. Bethe, “Theory of diffraction by small holes,” Phys. Rev., vol. 66, pp. 163-182, 1944.

[9] D. E. Grupp, H. J. Lezec, T. Thio, and T. W. Ebbesen, “Beyond the Bethe limit: tunable enhanced light transmission through a single sub-wavelength aperture,” Adv. Mat., vol. 11, pp. 860–862, 1999.

[10] A. Alù, F. Bilotti, N. Engheta, and L. Vegni, “Metamaterial covers over a small aperture,” IEEE Trans. Antennas Propagat, vol. 54, pp. 1632-1643, 2006.

[11] K. Aydin, A.O. Cakmak, L. Sahin, Z. Li, F. Bilotti, L. Vegni, and E. Ozbay, “Split-ring-resonator-coupled enhanced transmission through a single subwavelength aperture,” Phys. Rev. Lett., vol. 102, pp. 013904-1-4, 2009.

[12] D. Ates, A.O. Cakmak, E. Colak, R. Zhao, C.M. Soukoulis, and E. Ozbay, “Transmission enhancement through deep sub-wavelength apertures using connected split-ring resonators,” Opt. Expr., vol. 18, 3952, 2010.

[13] P. Jin, and R.W. Ziolkowski, “Multi-frequency, linear and circular polarized, metamaterial-inspired, near-field resonant parasitic antennas”, IEEE Trans. Antennas Propagat, vol. 59, pp. 1446-1459, 2011.

[14] CST Studio Suite 2012, CST Computer Simulation Technology AG, Available at: www.cst.com.

[15] N. Ortiz, J. D. Baena, M. Beruete, F. Falcone, M.A.G. Laso, T. Lopetegi, R. Marqués, F. Martin, J. Garcia-Garcia, and M. Sorolla “Complementary split-ring resonator for compact waveguide filter design,” Microw. Opt. Techn. Let., vol. 46, pp. 88–92, 2005.

[16] P. Jin, C.C. Lin, and R.W. Ziolkowski, “Multifunctional, electrically small, planar near-field resonant parasitic antennas,” IEEE Antennas Wireless Propag. Lett., vol. 11, pp. 200-204, 2012.

[17] F. Bilotti, A. Toscano, L. Vegni, K. Aydin, K. B. Alici, and E. Ozbay, “Equivalent-circuit models for the design of metamaterials based on artificialmagnetic inclusions,” IEEE Trans. Microw. Theory Tech., vol. 55, no. 12, pp. 2865–2873, Dec. 2007.

Chapter 4

Compact and multi-functional antennas based on MTM-inspired structures

The rapid development of wireless technologies, and their impact on the daily life, has increased the demand for communication devices that can operate using different communication standards. In antenna community, this trend results in an increased interest in compact and multi-functional antennas. In this regard, the recent introduction of MTM has allowed the design of numerous novel antennas characterized by enhanced performances and smaller dimensions with respect to the existing counterparts [1]-[14].

In this Chapter, we present the design of a compact antenna consisting of two orthogonal parasitic meandered monopoles excited by the near-filed coupling with a feeding bow-tie. The two parasitic radiators and the driven element are placed on two different faces of the same dielectric substrate and a coaxial probe excites the bow-tie through a metallic ground plane. In this way, the antenna has compact dimensions of $\lambda_0/6 \times \lambda_0/12 \times \lambda_0/75$ (excluding the ground plane) and shows a good impedance matching in the 2.4-2.485 GHz Wi-Fi band with an overall efficiency around 50%.

4.1 Design of a Compact Antenna by using Orthogonal Parasitic Meandered Monopoles

4.1.1 INTRODUCTION

Monopole antennas have been widely used in mobile communication systems due to their simple structure, omnidirectional radiation pattern and size reduction compared to the equivalent dipole antennas. However, the main dimension of a quarter-wave monopole ($\lambda_0/4$, where λ_0 is the free-space wavelength at the operating frequency) is often too high for modern communication systems, which are characterized by ever smaller available space for the radiating element. For this reason, several effective ways to reduce the antenna dimensions are proposed, such as the use of fractal or meandered structures [22], shorting pins [23] and MTM-inspired resonators [24]. However, as is evident by considering the well-known limits of electrically small antennas [25]-[27], the antenna bandwidth decreases with decreasing its size. Therefore, it is often difficult to simultaneously satisfy the requirements in terms of impedance bandwidth and overall dimensions.

In order to design a compact antenna with a good impedance matching in the 2.4 GHz Wi-Fi band, we propose here to use two orthogonal meandered printed monopoles with slightly different dimensions. In this way, we are able to merge the two independent resonances of the monopoles to achieve a wideband response.

However, although the meandered structure may seem the simplest solution to reduce the monopole size, it can lead to difficulties in the impedance matching to the source. In order to overcome this issue, we propose here to use a MTM-inspired solution [28]. In fact, MTMs concepts have been widely used to design several radiating structures [29]-[32]. Some of them [28], [31]-[32] are based on the employment of driven and parasitic elements that allow obtaining nearly complete impedance matching to the source and high radiation efficiency. Following this approach, although the two monopoles are the main radiating structures, in our case they aren’t connected to the feeding coaxial cable but act as parasitic resonators of a feeding bow-tie.

The structure of this Section is as follows. In Subsection 2, we present the design of a compact antenna based on the use of two meandered monopoles with the same dimensions. However, due to its narrow bandwidth, this structure cannot be used to cover the entire frequency spectrum of Wi-Fi systems. Therefore, in Subsection 3, we slightly change the dimensions of one of the monopoles in order to obtain two resonant frequencies that, properly merged, allow covering the 2.4-2.485 GHz frequency band.

4.1.2 ANTENNA DESIGN WITH EQUAL MEANDERED MONOPOLES

4.1.2.1 Antenna Structure

In order to show the benefit of using two slightly different monopoles in term of operating bandwidth, we first consider the design of an antenna with equal meandered monopoles. The structure, shown in Fig. 20-21, consists of a square ground plane and an FR4 substrate (ε_r = 4.3; tan δ = 0.025; thickness 1.6 mm) positioned orthogonal to it. Two orthogonal meandered monopoles connected to the ground are etched on one side of the dielectric substrate. On the other side, it is placed a bow-tie-like monopole connected to the inner conductor of a 50 Ω coaxial cable.

By properly co-designing the dimensions of the parasitic monopoles and the length of the driven bow-tie, we can tune the resonant frequency of the overall structure and obtain a good impedance matching. Moreover, thanks to the meandered structure, a compact antenna with overall dimensions of $\lambda_0/6 \times \lambda_0/12 \times \lambda_0/75$ has been obtained.

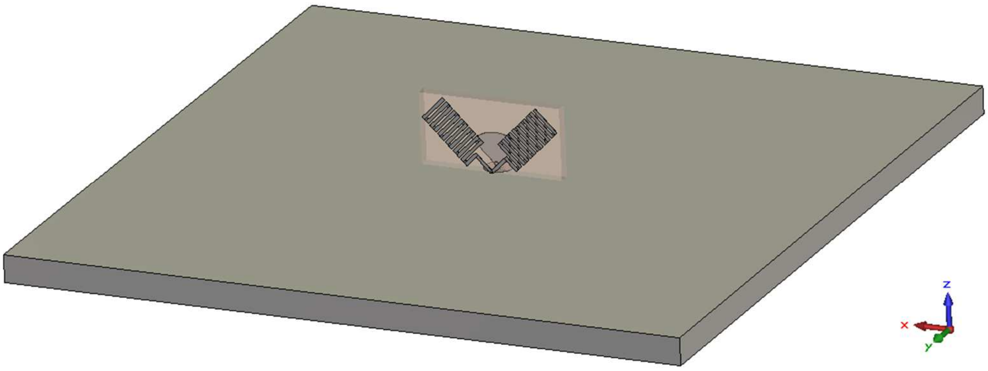

Fig. 71: Perspective view of the proposed antenna. The ground side is 10 cm.

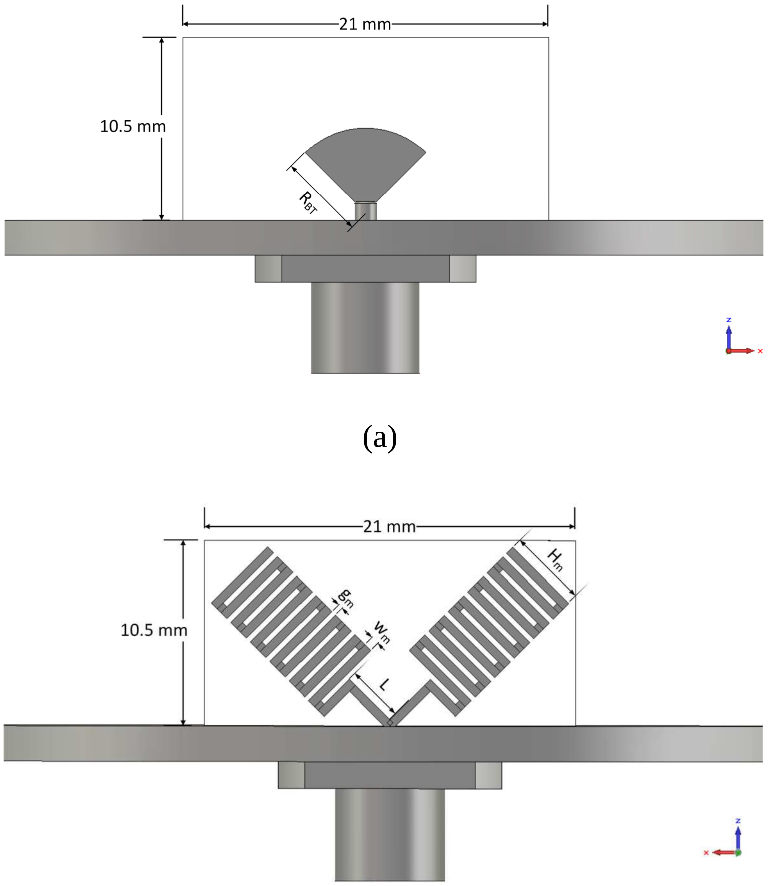

(a)

(b)

Fig. 72: Front view (a) and back view (b) of the proposed antenna with equal meandered monopoles. Antenna dimensions are: R_{BT} = 4.9 mm, H_m = 4.5 mm, g_m = 0.3 mm, w_m = 0.48 mm, L = 3 mm.

4.1.2.2 Simulation Results

The behavior of the structure presented in the previous subsection has been numerically evaluated by using the full-wave simulator CST Microwave Studio [17]. The reflection coefficient, reported in Fig. 22, show good impedance matching around 2.4 GHz. However, due to the identical size of the two monopoles, only one resonant frequency with a 2% -10 dB fractional bandwidth is present. Therefore, this antenna cannot cover the entire Wi-Fi band at 2.4 GHz.

For this reason, in the next Subsection we propose a modified structure with different monopoles lengths that shows a greater impedance bandwidth.

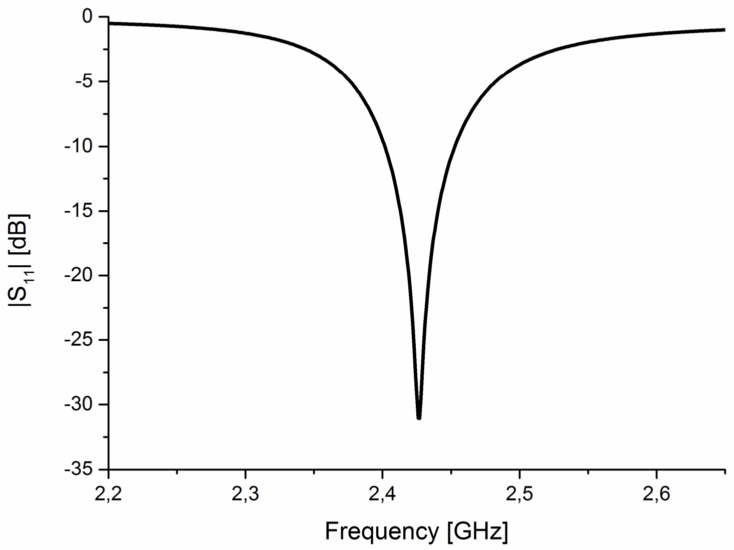

Fig. 73: Reflection coefficient amplitude of the proposed antenna with equal meandered monopoles.

For sake of completeness, in Fig. 23 we report also the radiation patterns at the resonant frequency of 2.425 GHz. The overall efficiency is around 65% in all the impedance bandwidth. Finally, the surface currents on the two meandered monopoles at 2.425 GHz, shown in Fig. 24, have approximately the same intensity, confirming the single frequency resonant behavior.

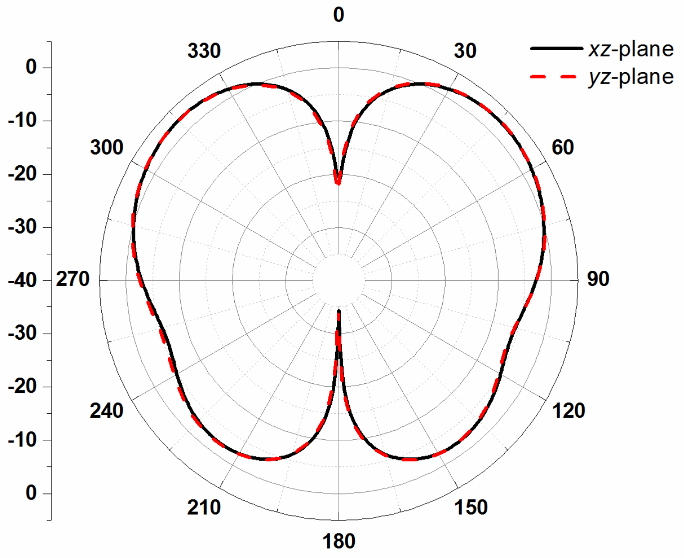

Fig. 74: Realized gain pattern at the resonant frequency (2.425 GHz) of the antenna with equal meandered monopoles.

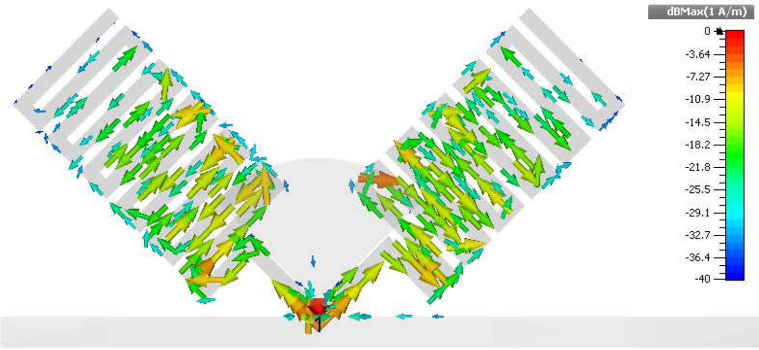

Fig. 75: Surface currents on the two meandered monopoles at the resonant frequency of the overall structure (2.425 GHz).

4.1.3 ANTENNA DESIGN WITH SLIGHTLY DIFFERENT MEANDERED MONOPOLES

4.1.3.1 Antenna Structure

In Subsection 2 we have presented the design of a compact antenna by using two parasitic meandered monopoles and a driven bow-tie. As shown through proper full-wave simulations, this antenna has a narrow operating bandwidth that doesn’t allow its employment as radiating element in 2.4 GHz Wi-Fi band. In order to enlarge its operating bandwidth and make it compatible with that application field, we propose here to use two slightly different meandered monopoles with different but close together resonant frequencies.

The resulting structure and the corresponding dimensions are shown in Fig. 25. In particular, the lengths of the two meandered monopoles differ for 5 mm, while all the other dimensions of the two monopoles are equal between them.

4.1.3.2 Simulation Results

The simulated reflection coefficient, obtained by using CST Microwave Studio, is shown in Fig. 26 and compared to the previous case. By properly co-designing the bow-tie and meandered monopoles, a good impedance matching is obtained. Moreover, due to the different dimensions of the monopoles, two slightly different resonant frequencies are readily apparent. In this way, the -10 dB fractional bandwidth grows from 2% to 3.5% and allows covering the entire 2.4-2.485 GHz band assigned to the Wi-Fi systems.

In particular, as can be seen from Fig. 27 and Fig. 28, the shortest meandered monopole resonates at 2.416 GHz, while the longest one resonates at 2.461 GHz. These frequencies correspond to the two negative peaks of the reflection coefficient. The radiation patterns at these resonant frequencies are shown in Fig. 29-30.

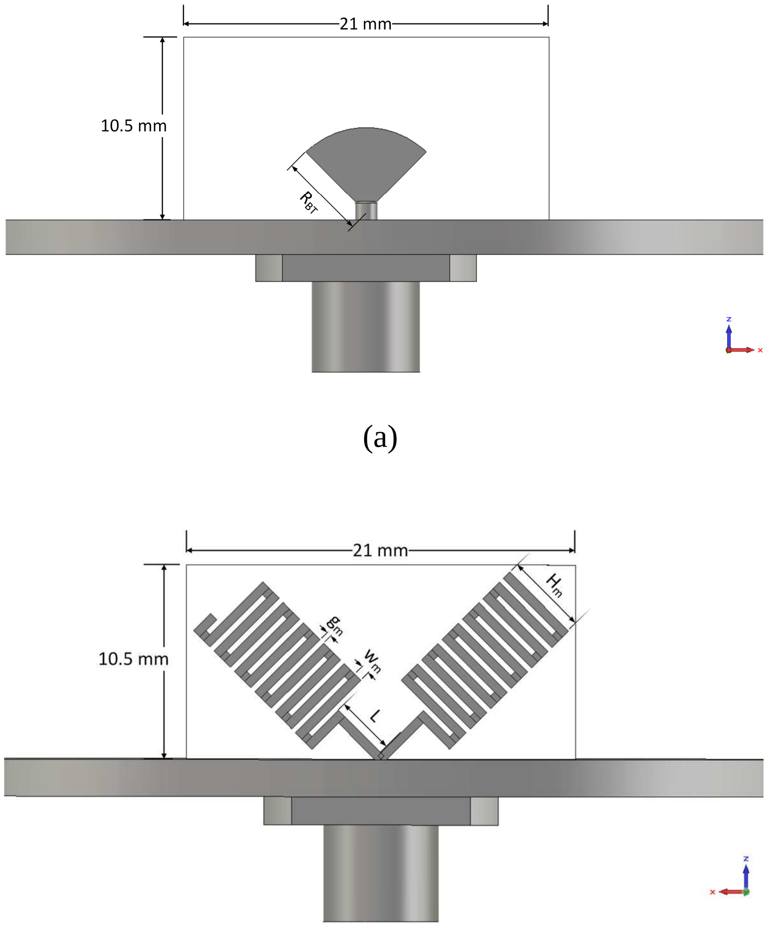

(a)

(b)

Fig. 76: Front view (a) and back view (b) of the proposed antenna with slightly different meandered monopoles. Antenna dimensions are: R_{BT} = 5 mm, H_m = 4.5 mm, g_m = 0.3 mm, w_m = 0.48 mm, L = 3 mm.

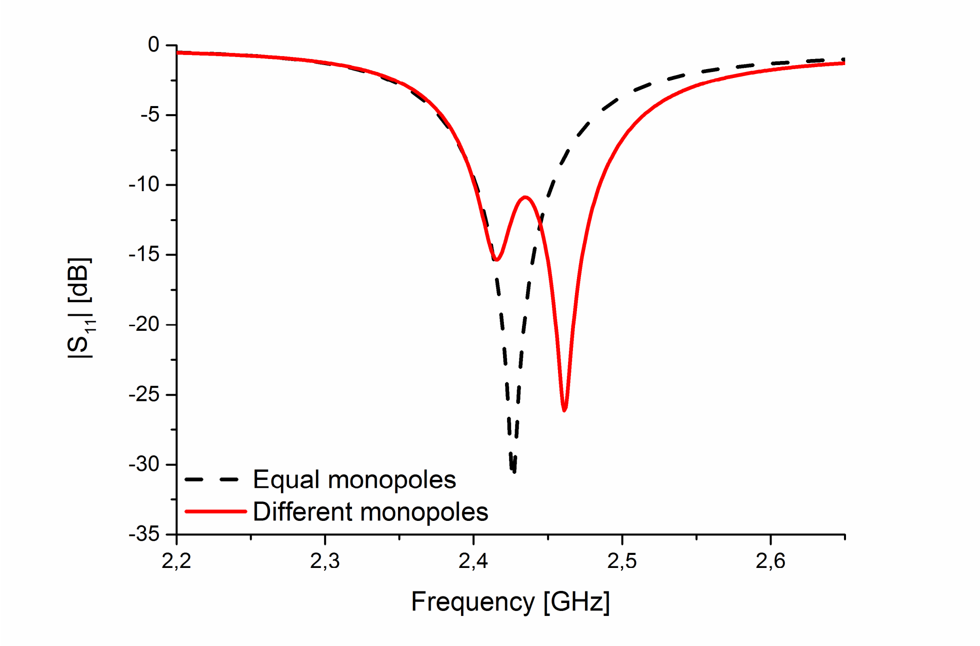

Fig. 77: Reflection coefficient amplitude of the proposed antenna with slightly different monopoles (red-solid line), compared to the one of the previous case (black-dashed line).

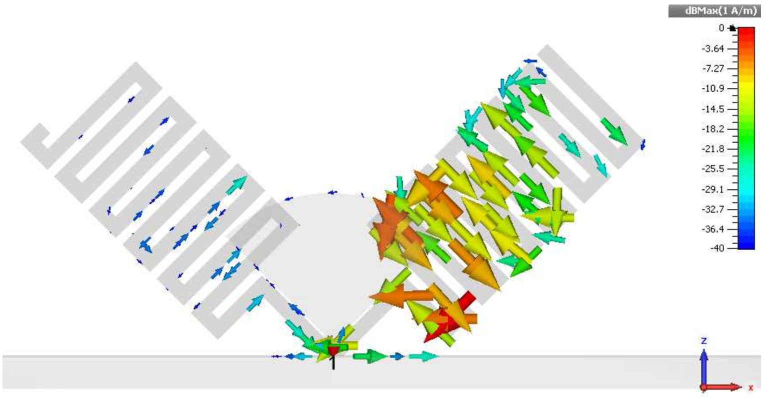

Fig. 78: Surface currents on the two meandered monopoles at the lowest resonant frequency of the overall structure shown in Fig. 25.

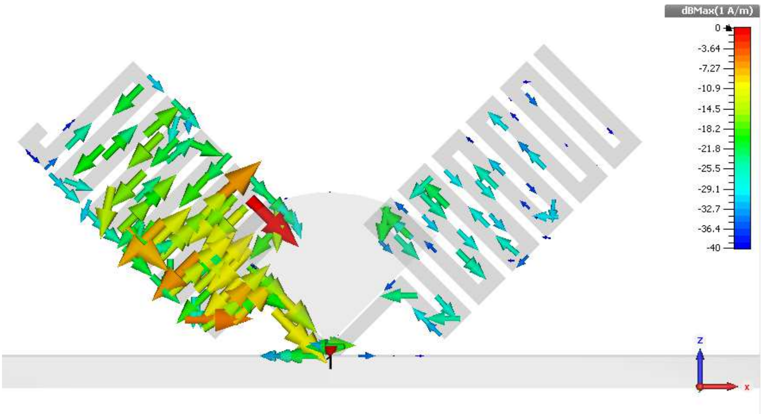

Fig. 79: Surface currents on the two meandered monopoles at the highest resonant frequency of the overall structure shown in Fig. 25.

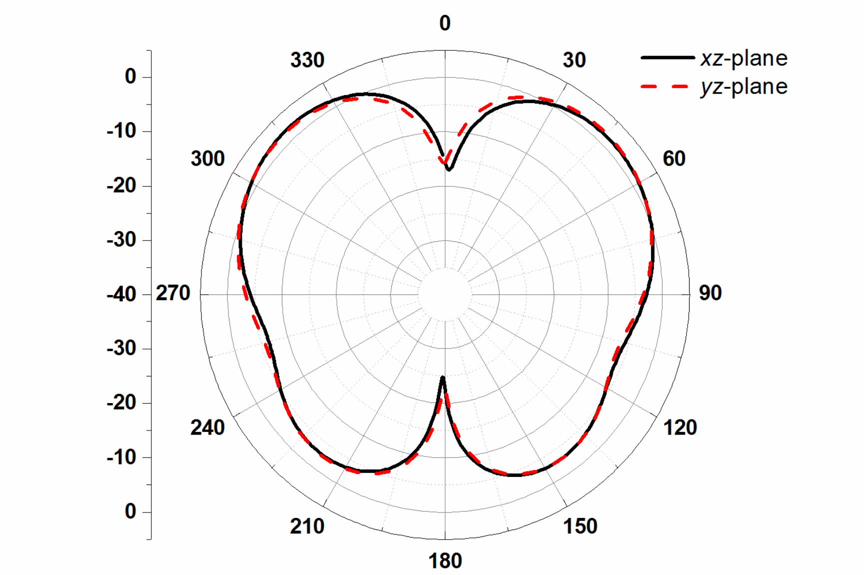

Fig. 80: Realized gain pattern at the lowest resonant frequency (2.416 GHz) of the antenna with slightly different monopoles.

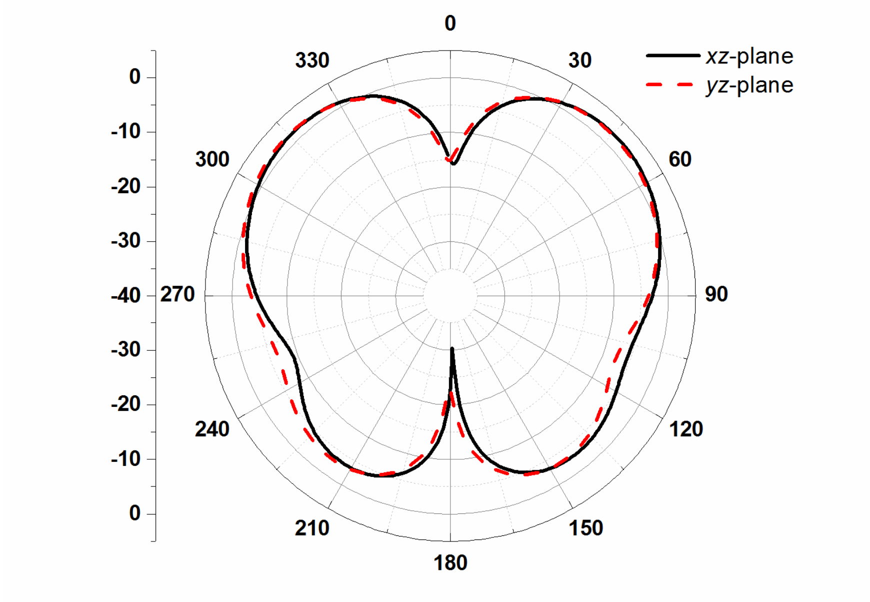

Fig. 81: Realized gain pattern at the highest resonant frequency (2.461 GHz) of the antenna with slightly different monopoles.

4.2 Summary

In this Chapter, we presented a compact antenna consisting of two orthogonal meandered monopoles that act as parasitic elements of a driven bow-tie. In particular, we have shown that by using two monopoles with slightly different dimensions, a greater impedance bandwidth can be obtained. Using this approach, we have presented a compact antenna operating in the 2.4 GHz Wi-Fi band with overall dimensions of $\lambda_0/6\times\lambda_0/12\times\lambda_0/75$.

4.3 References

[1] R.W. Ziolkowski and A.D. Kipple, “Application of double negative materials to increase the power radiated by electrically small antennas,” IEEE Trans. Antennas Propagat., vol. 52, pp. 2626-2640, 2003.

[2] R.W. Ziolkowski and A. Erentok, “Metamaterial-based efficient electrically small antennas,” IEEE Trans. Antennas Propagat., vol. 54, pp. 2113-2130, 2006.

[3] P. Jin and R.W. Ziolkowski, “Multi-frequency, linear and circular polarized, metamaterial-inspired, near-field resonant parasitic antennas,” IEEE Trans. Antennas Propagat., vol. 59, pp. 1446-1459, 2011.

[4] F. Qureshi, M.A. Antoniades, and G.V. Eleftheriades, “A compact and low-profile metamaterial ring antenna with vertical polarization,” IEEE Antennas Wireless Propag. Lett., vol. 4, pp. 333-336, 2005.

[5] A. Alù, F. Bilotti, N. Engheta, and L. Vegni, “Sub-wavelength planar leaky-wave components with metamaterial bilayers,” IEEE Trans. Antennas Propagat., vol. 55, pp. 882-891, 2007.

[6] F. Bilotti, A. Alù, and L. Vegni, “Design of miniaturized metamaterial patch antennas with µ-negative loading,” IEEE Trans. Antennas Propagat., vol. 56, pp. 1640-1647, 2008.

[7] J. Zhu, M.A. Antoniades, and G.V. Eleftheriades, “A compact tri-band monopole antenna with single-cell metamaterial loading,” IEEE Trans. Antennas Propagat., vol. 58, pp. 1031-1038, 2010.

[8] S. Tricarico, F. Bilotti, and L. Vegni, “Multi-functional dipole antennas based on artificial magnetic metamaterials,” IET Microw. Antennas Propag., vol. 4, pp. 1026-1038, 2010.

[9] F. Bilotti and C. Vegni, “Design of high-performing microstrip receiving GPS antennas with multiple feeds,” IEEE Antennas Wireless Propagat. Lett., vol. 9, pp. 248-251, 2010.

[10] K.B. Alici and E. Ozbay “Electrically small split ring resonator antennas,” J. Appl. Phys., vol. 101, pp. 08314-1-4, 2007.

[11] A. Alù, F. Bilotti, N. Engheta, and L. Vegni, “A conformal omni-directional sub-wavelength metamaterial leaky-wave antenna,” IEEE Trans. Antennas Propagat., vol. 55, pp. 1698-1708, 2007.

[12] F. Bilotti and C. Vegni, “On the employment of artificial magnetic metamaterials to effectively reduce the back-lobe of patch antennas,” Electromagnetics, vol. 48, pp. 513-522, 2008.

[13] J. Gemio, J. Parròn, P. de Paco, G. Junkin, J. Marin, and O. Menéndez, “A split-ring-resonator loaded monopole for triple band applications,” J. Electromagn. Waves and Applicat., vol. 24, pp. 241-250, 2010.

[14] V. V. Varadan and I. K. Kim, “Compact, multi band plasmonic resonator antenna,” Proc. of the IEEE/URSI Int. Symp. Antennas Propagat., Charleston, USA, 1-5 June 2009.

[15] F. Bilotti, A. Toscano, and L. Vegni, “Design of Spiral and Multiple Split-Ring Resonators for the realization of miniaturized metamaterial samples,” IEEE Trans. Antennas Propagat., vol. 55, pp. 2258-2267, 2007.

[16] F. Bilotti, A. Toscano, L. Vegni, K.B. Alici, K. Aydin, and E. Ozbay, “Equivalent circuit models for the design of metamaterials based on artificial magnetic inclusions,” IEEE Trans. Microwave Theory Tech., vol. 55, pp. 2865-2873, 2007.

[17] CST Studio Suite 2010, CST Computer Simulation Technology AG, www.cst.com.

[18] D.J. Roscoe, L. Shafai, A. Ittipiboon, M. Cuhaci, and R. Douville, “Tuneble dipole antennas,” Proc. of the IEEE/URSI Int. Symp. Antennas Propagat., vol. 2, pp. 672-675, 1993.

[19] S. Kawasaki, and T. Itoh, “A slot antenna with electronically tunable length,” Proc. of the IEEE/URSI Int. Symp. Antennas Propagat., vol. 1, pp. 130-133, 1991.

[20] J. L. Freeman, B. J. Lamberty, and G.S. Andrews, “Optoelectronically reconfigurable monopole antenna,” Electron. Lett., vol. 28, pp. 1502-1503, 1992.

[21] B. Schoenlineer, A. Abbaspour-Tamijani, L.C. Kempel, and G.M. Rebeiz, “Switchable low-loss RF MEMS Ka-band frequency-selective surface,” IEEE Trans. Microwave Theory Tech., vol. 52, pp. 2474-2481, 2004.

[22] S. R. Best, “On the performnace properties of the Koch fractal and other bent wire monopoles,” IEEE Trans. Antennas Propagat., vol. 51, pp. 1292-1300, June 2003.

[23] S. C. Pan and K. L. Wong, “Dual frequency triangular microstrip antenna with a shorting pin”, IEEE Trans Antennas Propagation, pp. 1889-1891, December 1997.

[24] M. Barbuto, F. Bilotti, and A. Toscano, “Design of a multifunctional SRR-loaded printed monopole antenna,” Int. J. RF Microw. CAE, vol. 22, pp. 552-557, 2012.

[25] R. C. Hansen, “Fundamental limitations in antennas,” Proceedings of the IEEE, vol. 69, pp. 170-182, February 1981.

[26] J. S. McLean, “A re-examination of the fundamental limits on the radiation Q of electrically small antennas,” IEEE Trans. Antennas Propagat., vol. 44, pp. 672-676, May 1996.

[27] R. Collin, S. Rothschild “Evaluation of antenna Q,” IEEE Trans. Antennas Propagat., vol. 12, pp. 23-27, January 1964.

[28] P. Jin and R. W. Ziolkowski, “Multiband extensions of the electrically small near field resonant parasitic Z antenna,” Microw. Antennas Propag., vol. 4, pp. 1016–1025, Aug. 2010.

[29] M. Barbuto, F. Trotta, F. Bilotti, and A. Toscano “A combined bandpass filter and polarization transformer for horn antennas,” IEEE Antennas Wireless Propag. Lett., vol. 12, pp. 1065-1068, 2013.

[30] J. Zhu, M. A. Antoniades, and G. V. Eleftheriades “A compact tri-band monopole antenna with single-cell metamaterial loading,” IEEE Trans. Antennas Propagat., vol. 58, pp. 1031-1038, April 2010.

[31] P. Jin, C. C. Lin, and R. W. Ziolkowski, “Multifunctional, electrically small, planar near-field resonant parasitic antennas,” IEEE Antennas Wireless Propag. Lett., vol. 11, pp. 200–204, 2012.

[32] M. Barbuto, A. Monti, F. Bilotti, and A. Toscano, “Design of a non-foster actively loaded SRR and application in metamaterial-inspired components,” IEEE Trans. Antennas Propag., vol. 61, no. 3, pp. 1219–1227, Mar. 2013.

Chapter 5

Mantle cloaking for co-site radio-frequency antennas

Modern communication systems are progressively handling an ever-increasing number of services, which require radiators to broadcast information across an ever broadening spectrum. Consequently, communication platforms, such as mobile communication towers, satellite payloads, aircrafts, and ship trees, host an ever-increasing number of antennas within a limited space. However, antennas cannot be packed together ad libitum in a small area, for at least two reasons: electromagnetic interference among different antennas dramatically limits their functionalities, and blockage effects significantly affect their electrical (e.g., impedance matching) and radiation properties (e.g., radiation pattern shape and realized gain)[1].

In this Chapter, we show that electromagnetic cloaking,[2]-[7] and in particular, mantle cloaking,[8]-[16] can be used to largely mitigate the issues related to antenna packing in overcrowded platforms. The proposed idea, which is demonstrated and validated both numerically and experimentally, allows placing different antennas in deep electrical proximity (i.e., antennas are nearly touching one another, with a separation of a small fraction of the operating wavelength), without affecting their operation. The proposed solution, which is based on the design of patterned metallic sheets surrounding the antennas, may revolutionize co-siting strategies for the design of complex radio-wave platforms, allowing more services in a reduced space.

Differently from cloaking techniques based on transformation electromagnetics,[2]-[4] which guide the impinging electromagnetic fields around the object to hide, preventing any interaction between the field and the object, scattering cancellation [6]-[7] is based on producing a destructive interference between the field scattered by the illuminated object and the one scattered by the cloaking cover placed around it. The latter technique, thus, is particularly appropriate to cloak objects with an electromagnetic functionality, such as antennas and sensors [8], especially wire antennas [12]-[16]. At microwave frequencies, scattering cancellation can be realized applying the mantle cloaking technique [7], based on patterned metallic sheets that synthesize the required surface impedance to support proper currents on the metasurface, which cancel the scattering from the object we want to hide.

We show that properly designed mantle cloaks, consisting of patterned metallic sheets placed around cylindrical monopoles, allow tightly packing the same antennas together in a highly dense telecommunication platform. Our experimental demonstration is applied to the relevant example of two cylindrical monopole radiators operating for 3G and 4G mobile communications. The two antennas are placed in close proximity, separated by 1/10 of the shorter operational wavelength, and, after cloaking, are shown to remarkably operate as if isolated in free-space. This result paves the way to unprecedented co-siting strategies for multiple antennas handling different services and installed in overcrowded platforms, such as communication towers, satellite payloads, aircrafts, or ship trees. More broadly, this work presents a significant application of cloaking technology to improve the efficiency of modern communication systems

5.1 Design mantel cloaks

In order to highlight the relevant potential of these concepts for radio-communication applications, we consider two closely spaced monopole antennas mounted on the same platform (see Figure 82)

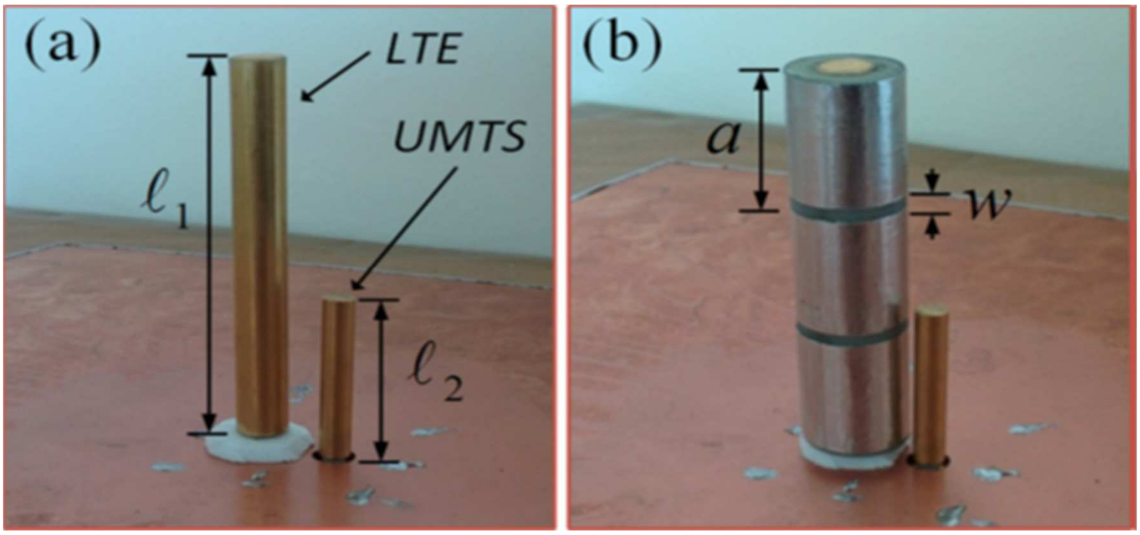

Fig. 82: Photograph of the fabricated system, consisting of two electrically close monopoles working for LTE and UMTS services, respectively, in both (a) uncloaked and (b) cloaked scenarios.

and operating in the Long Term Evolution (LTE) low band (790–860 *MHz*) and

UMTS services (1900–2200 *MHz)*, respectively. The two antennas are placed in extreme proximity of each other, with a separation distance equal to $d = \lambda_2/10$, being λ_2 the central wavelength in the UMTS band. The lengths of the two antennas and their radius are l_1 = 80 *mm*, l_2 = 35 *mm* and r_1 = 5 *mm*, r_2 = 3 *mm*, respectively. The two monopoles have been fabricated as brass cylinders drilled in the bottom face to allow the insertion of SubMiniature version A (SMA) connectors, whereas the ground plane consists of a double-sided printed circuit board (PCB) laminate (with dimensions 307 x 307 mm^2). In order to mitigate edge effects due to its finite dimensions, the two metallic sides of the PCB laminate have been short-circuited through a highly conductive metallic tape alongside the laminate perimeter and some vias placed around the SMA connectors. Finally, the spacing between the LTE monopole and the ground, needed to achieve impedance matching with the source, has been ensured with a spacer made of an electromagnetically transparent foam.

In the scenario depicted in Figure 82 (a), both monopoles are located in the near-field of each other. However, degradation effects caused by the presence of the UMTS antenna on the LTE are expected to be smaller, due to the electrically small dimension of the

UMTS radiator at the LTE operation frequencies. Conversely, the LTE antenna represents a strong scatterer for the UMTS monopole, due to its large electrical dimensions in the UMTS band. Therefore, in the following we explore an optimal mantle cloak for the LTE monopole to significantly reduce its electrical presence within the entire UMTS band.

The cloak, shown in Figure 82 (b), consists of a hollow cylinder made of vetronite (inner and outer radius are $r^{int}{}_1 = r_1$ and $r^{out}{}_1 = 2\ r_1$, respectively) and a metasurface consisting of three horizontal metallic strips, whose width is $a = 26.67\ mm$ and separation $w = 2.6$ mm. The metasurface design has been developed using the formulas in Refs. [9] and [10], and optimizing the scattering reduction and cloaking bandwidth [17].

The simple pattern of the metasurface and the high robustness of the design to fabrication tolerances allowed us to manually engineer the three metallic strips, using high-conductivity metallic tape.

5.2 Simulation and experimental results

The realized cloak may retrofit existing systems that can be easily added to removed without surface friction and without perturbing its original operation. As it can be appreciated in Figure 83, our simulations, conducted through a full-wave electromagnetic simulator [18] for an ideal transverse-magnetic plane wave excitation, confirm that the designed cloak allows reducing the overall LTE antenna scattering by 10 dB at 2050 MHz with a broad -3 dB fractional bandwidth of 20%.

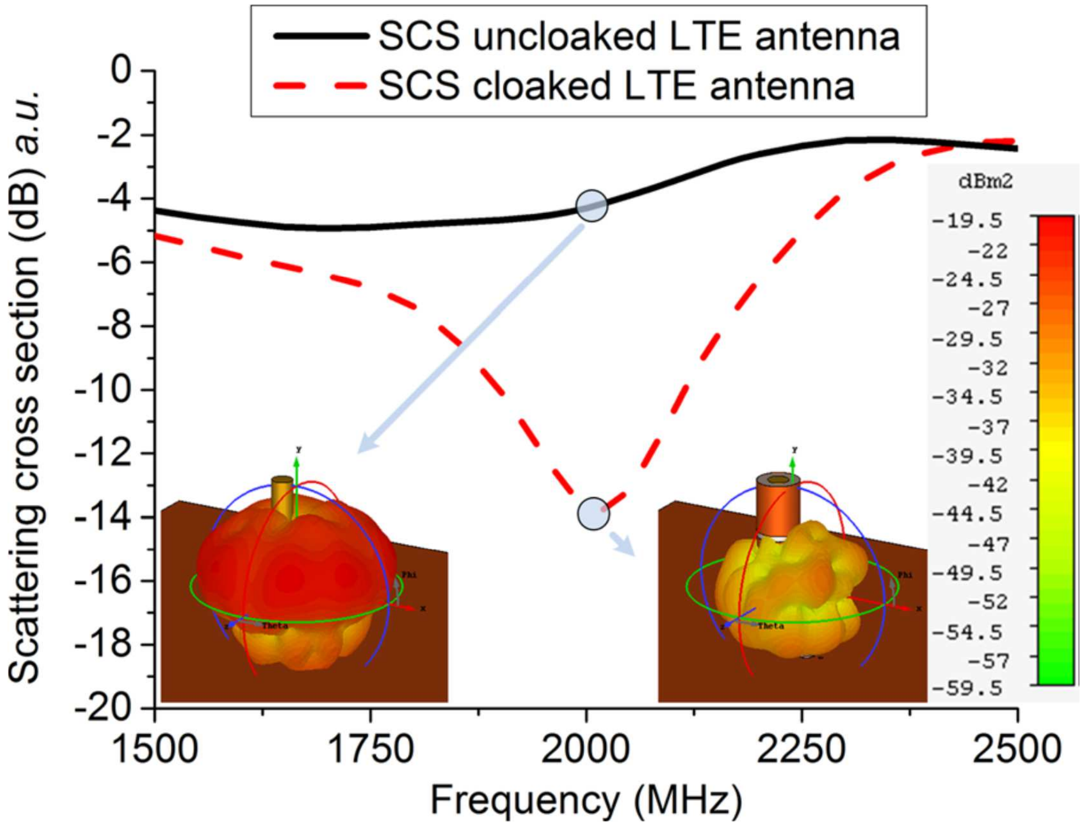

Fig. 83: . SCS of the uncloaked (continuous line) and cloaked (dashed line) LTE antenna for a plane wave excitation. In the insets, it is possible to appreciate the 3D bistatic scattering cross section of the antenna in the uncloaked (left) and cloaked (right) case. The scale used for the two scattering patterns is the same

This significant bandwidth performance, a necessity for practical communication scenarios, is ensured by the non-negligible thickness of the cloak, as discussed in Refs. [16] and [19]. The insets of the figure show the different scattering patterns in the two cases on the same scale

In Figure 84, we show the magnitude of the measured scattering parameters at the antenna feeds. We mark as “isolated” the scenario in which only one antenna is present on the platform. Conversely, “uncloaked” is the scenario in Figure 82 (a), in which both antennas are present, and “cloaked” refers to the scenario in Figure 82 (b), in which both antennas are present, and the LTE radiator is covered by the cloak described above.

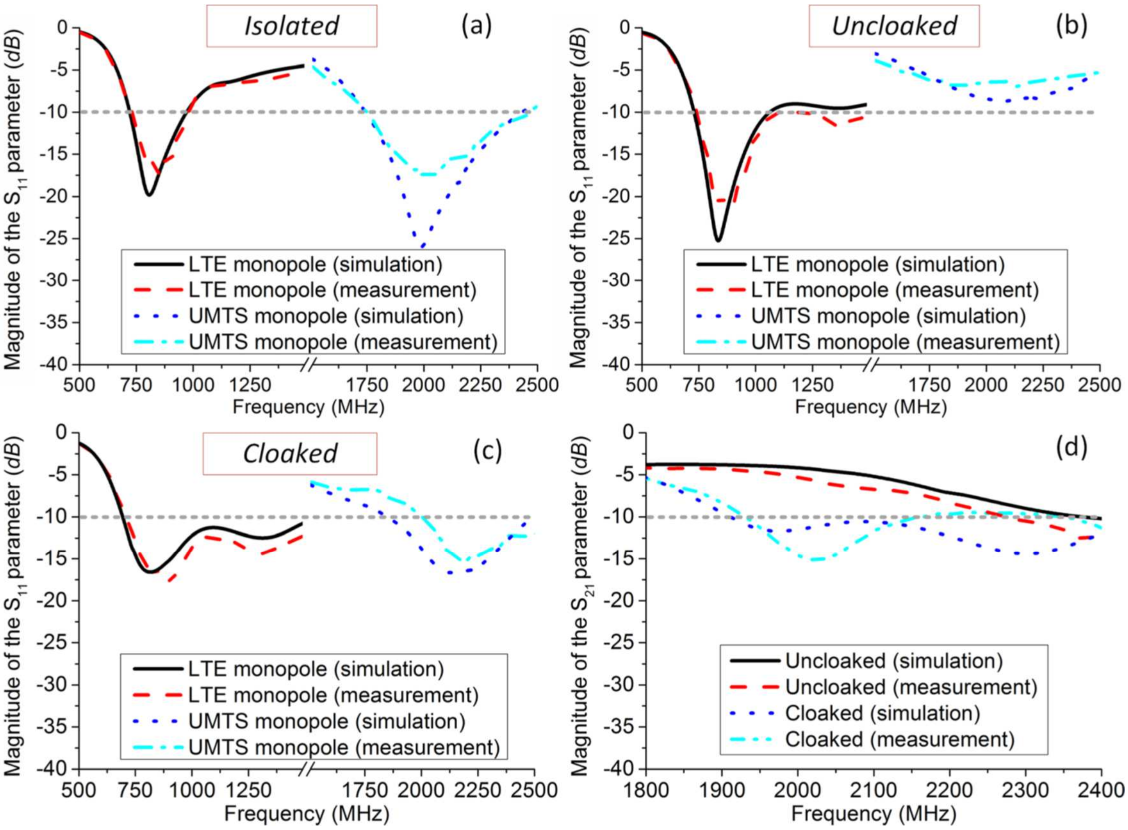

Fig. 84: (a)-(c) Magnitude of the reflection coefficient at the input ports of the monopoles shown in Figure 82 in the isolated, uncloaked, and cloaked scenarios, respectively. (d) Mutual coupling between the two monopoles in the uncloaked and cloaked scenarios. The horizontal line represents the commonly used matching threshold at - 10 dB.

While the antennas are well matched in the isolated case, in the uncloaked scenario, as expected, the interaction between the two antennas is responsible for a dramatic deterioration of the impedance matching properties at the UMTS monopole port (Figure 84 (b) dotted and dash-dotted lines), as well as a strong coupling coefficient within the UMTS frequency band (Figure 84 (d) continuous and dashed lines). Conversely, in the cloaked scenario, we observe a restoration of the original impedance matching features of the UMTS monopole (Figure 84 (c) dotted and dash-dotted lines), while also the mutual coupling between the two antennas is significantly reduced within the UMTS band (Figure 84 (d) dotted and dash-dotted lines). The second additional weak resonance around 1250 *MHz* in the LTE reflection coefficient, in both the uncloaked and cloaked scenarios, is given by the presence of the UMTS antenna, whose scattering cannot be neglected any longer at higher frequencies outside the LTE band.

However, this interaction does not affect the proper operation of the LTE monopole, because it occurs outside its operational bandwidth. These results prove that the realized mantle cloak is effectively able to recover the antenna impedance matching of the UMTS antenna despite the presence of the LTE antenna in very tight proximity. The LTE monopole is still properly working within its operating band, despite the presence of the surrounding cloak. This result has been achieved by designing the cloak to operate within the UMTS band while being almost transparent in the LTE one [17]

To further demonstrate the improvement offered by the designed mantle cloak, we show the measured radiation properties of the two antennas. In Figure 85, we show the farfield realized gain patterns of the UMTS antenna, measured with the Satimo StarLab system.

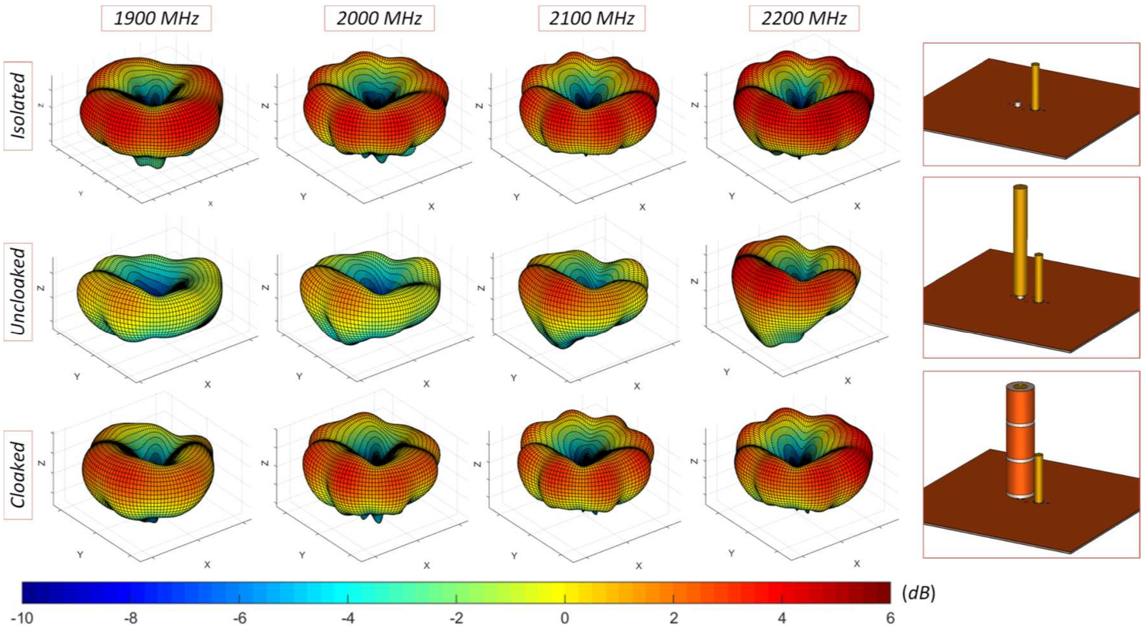

(a) (b)

Fig. 85: (a) Far-field measured realized gain patterns of the UMTS monopole at three frequencies around the cloaking frequency in the isolated, uncloaked, and cloaked cases; (b) Schematic view of the three considered scenarios (isolated, uncloaked, and cloaked).

Comparing the results to the isolated case, we observe a dramatic deterioration of the far field patterns in the uncloaked scenario, impacting the symmetry and exhibiting preferred radiation directions not expected in the isolated case. In the cloaked case, instead, the UMTS patterns are almost totally restored and show a good agreement with the isolated case. This is impressive, given the moderate loss of the vetronite spacer used in this design, which highlights the wideband non-resonant nature of the mantle cloaking technique.

Analogous considerations can be made inspecting the very near-field distribution around the antennas, as shown in Figure 86. Here near-field maps have been obtained with a raster scanning non-resonant E-field probe with both high spatial resolution and position accuracy (more details about this instrument can be found in Ref.[11]). The near-zone field plots are taken on a plane perpendicular to the axis of the monopoles, at approximately half the UMTS monopole height. The near-field distributions of the electric field in the cloaked case are almost identical to the ones of the isolated case, further proving the cloaking effect. As in the far-field measurements, the bare LTE monopole acts as a director to the UMTS antenna when they are placed in ultra-tight proximity.

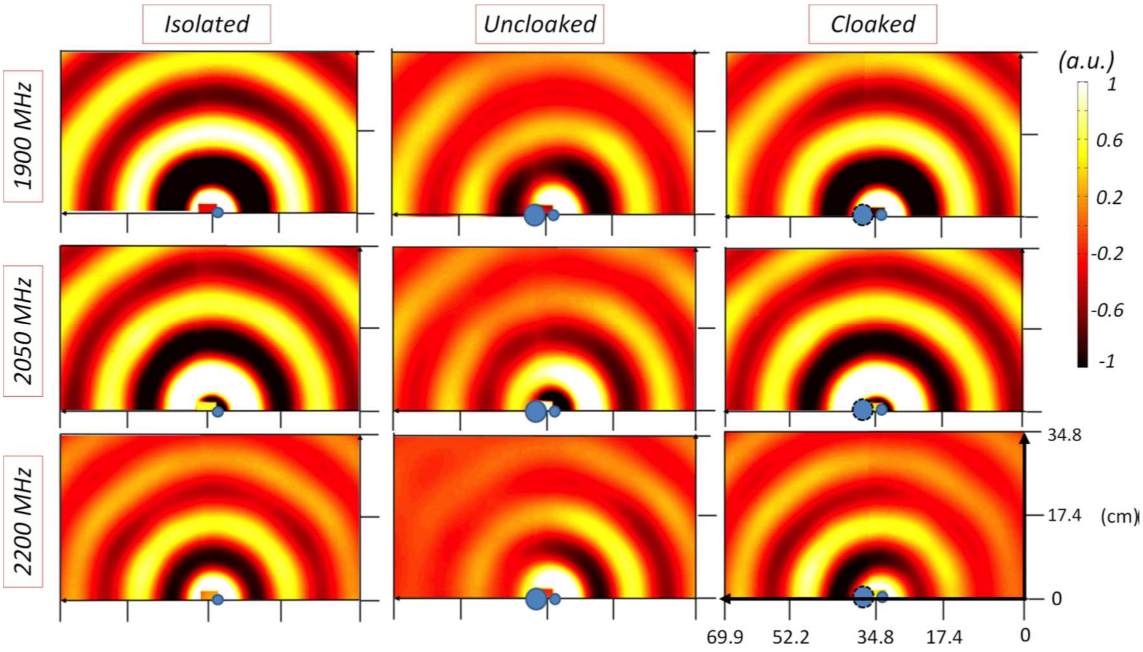

Fig. 86: Snapshot in time of the transverse electric field distribution on a plane perpendicular to the monopole axes at the two boundary frequencies in the isolated, uncloaked, and cloaked case. The blue circles show the position of the two monopole

The upper UMTS frequencies are mostly affected, where we see almost complete radiation blockage by the LTE monopole in the uncloaked case. In contrast, the cloakallows to completely suppress these effects in the near- and far-field. It is also worth noticing that the restoration effect achieved here is within a significantly wider range of frequencies compared to earlier solutions adopted in mantle cloaking designs [13]-[15].

Interestingly, since both antennas properly operate in both the isolated and the cloaked scenarios, the designed cloak is backwards compatible with pre-existing antenna systems. This design peculiarity has two important consequences:

a) there is no need to design the cloak and the LTE monopole together, making, thus, the cloak applicable to a pre-existing monopole with same radius;
b) the cloaked LTE antenna can be approached as much as needed to an already installed UMTS radiator without affecting its performance, i.e., the cloak functionality is totally independent of the type of excitation or distance to nearby antennas.

To conclude, we have experimentally demonstrated an extremely compact communication platform for mobile communications based on mantle cloaking, composed by two tightly packed monopole antennas operating in the low- LTE and UMTS bands, respectively. Rarely explored in typical cloaking demonstrations, we have shown here by standard near- and far-field techniques the potential of the mantle cloaking technique applied to mobile communication systems. In particular, by exploiting the peculiarities of the mantle cloaking technique, we have restored the operation of an UMTS antenna that was shown to be strongly affected by the nearby presence of an LTE radiator over a broad frequency range. This demonstration has been obtained using a simple and low-cost patterned metallic cover placed around the LTE antenna. Similar solutions can be employed for other multiple-antenna scenarios, enabling numerous degrees of freedom for the design of miniaturized satellite and terrestrial radio platforms.

5.3 Summary

In this Chapter, we show that properly designed mantle cloaks, consisting of patterned metallic sheets placed around cylindrical monopoles, allow tightly packing the same antennas together in a highly dense telecommunication platform. Our experimental demonstration is applied to the relevant example of two cylindrical monopole radiators operating for 3G and 4G mobile communications. The two antennas are placed in close proximity, and, after cloaking, are shown to remarkably operate as if isolated in free-space. This result paves the way to unprecedented co-siting strategies for multiple antennas handling different services and installed in overcrowded platforms, such as communication towers, satellite payloads, aircrafts, or ship trees.

5.4 References

[1] C. Balanis, Antenna Theory: Analysis and Design (Wiley & Sons, Hoboken, 2005), p. 468

[2] J. B. Pendry, D. Schurig, and D. R. Smith, Science 312, 1780 (2006).

[3] U. Leonhard, Science 312, 1777 (2006).

[4] D.-H. Kwon and D. H. Werner, Appl. Phys. Lett. 92, 113507 (2008).

[5] S. Tretyakov, P. Alitalo, O. Luukkonen, and C. Simovski, Phys. Rev. Lett.103, 103905 (2009).

[6] A. Alù and N. Engheta, Phys. Rev. E 72, 016623 (2005).

[7] A. Alù, Phys. Rev. B 80, 245115 (2009)0

[8] A. Alù and N. Engheta, Phys. Rev. Lett. 102, 233901 (2009).

[9] Y. R. Padooru, A. B. Yakovlev, P. Y. Chen, and A. Alù, J. Appl. Phys. 112, 034907 (2012).

[10] A. Monti, J. Soric, A. Alù, A. Toscano, and F. Bilotti, IEEE Trans. Antennas Propag. 63, 1775 (2015).

[11] J. C. Soric, P. Y. Chen, A. Kerkhoff, D. Rainwater, K. Melin, and A. Alù, New J. Phys. 15, 033037 (2013).

[12] J. C. Soric, R. Fleury, A. Monti, A. Toscano, F. Bilotti, and A. Alù, IEEE Trans. Antennas Propag. 62, 4220 (2014).

[13] A. Monti, J. Soric, A. Alù, F. Bilotti, A. Toscano, and L. Vegni, IEEE Antennas Wireless Propag. Lett. 11, 1414 (2012).

[14] H. M. Bernety and A. B. Yakovlev, IEEE Trans. Antennas Propag. 63, 1554 (2015).

[15] Z. H. Jiang, P. E. Sieber, L. Kang, and D. H. Werner, Adv. Funct. Mater.25, 4708 (2015).

[16] J. C. Soric, A. Monti, A. Toscano, F. Bilotti, and A. Alù, IEEE Trans. Antennas Propag. 63, 4827 (2015).

[17] See supplementary material at http://dx.doi.org/10.1063/1.4944042 for a more detailed description of the cloak design.

[18] See www.cst.com for CST Microwave Studio 2014.

[19] J. C. Soric, A. Monti, A. Toscano, F. Bilotti, and A. Alu, IEEE Trans. Antennas Propag. 63, 3235 (2015).

Publications

Journal Publications

1. M. Barbuto, F. Trotta, F. Bilotti, and A. Toscano, “Horn antennas with integrated notch filters,” *IEEE Transactions on Antennas and Propagation,* Vol. 63, No. 2, pp. 781-785, 2015.

2. M. Barbuto, F. Trotta, F. Bilotti, and A. Toscano, “Circular polarized patch antenna generating orbital angular momentum,” *Progress In Electromagnetics Research*, Vol. 148, 23-30, 2014.

3. M. Barbuto, F. Trotta, F. Bilotti, and A. Toscano, “A combined bandpass filter and polarization transformer for horn antennas,” *IEEE Antennas and Wireless Propagation Letters*, Vol. 12, pp. 1065-1067, 2013.

4. M. Barbuto, F. Trotta, F. Bilotti, A. Toscano, "Varying the operation bandwidth of metamaterial-inspired filtering modules for horn antennas," Progress In Electromagnetics Research - PIER C, Vol. 58, pp. 61-68, 2015.

5. M. Barbuto, F. Trotta, F. Bilotti, A. Toscano, "Design of a low-profile by using orthogonal parasitic meandered monopoles," Progress In Electromagnetics Research Letters, Vol. 55, pp. 23-29, 2015.

6. Alessio Monti, Jason Soric, Mirko Barbuto, Davide Ramaccia, Stefano Vellucci, Fabrizio Trotta, Andrea Alù, Alessandro Toscano, and Filiberto Bilotti " Mantle cloaking for co-site radio-frequency antennas " Appled Phisics Letters 108, 113502 (2016)

.

Conference Papers

1. D. Ramaccia, A. Verrengia, F. Bilotti, A. Toscano, A. Monti, M. Barbuto, F. Trotta, D. Muha, and S. Hrabar, “Experimental verification of broadband antennas loaded with metamaterials,” Proc. of the 2015 IEEE International Symposium on Antennas and Propagation and USNC/URSI National Radio Science Meeting, Vancouver, BC, Canada, 19-25 July, 2015.

2. M. Barbuto, D. Ramaccia, F. Trotta, A. Toscano, and F. Bilotti, “Conical horn antennas with enhanced functionalities through the use of metamaterial concepts,” Proc. of the 2014 European Conference on Antennas and Propagation (EuCAP 2014), The Hague, The Netherlands, 6-11 April 2014, (invited paper).

Biographical Note

April 28, 1972	Born, Rome, Italy
January 2012 – December 2016	PhD Student in Applied Electomagnetics

abrizio Trotta was born in Rome, Italy, on April 28, 1972. He received the Laurea in electronic engineering from “Roma Tre” University, Rome, Italy, in 2003. In 2011, he started his PhD research program at the Department of Applied Electronics of “Roma Tre” University. From 1998 to 2003 he was RF Engineer at Siel Elettronica S.p.A., Rome, Italy. Since 2003 he is Antenna and unit system Engineer at Elettronica S.p.A., Rome, Italy. His current research interests include in the field of mechanical and electrical design broadband microwave components and radiating elements; multifunctional phased array antennas; broadband metamaterials based on non-Foster circuits, miniaturized microwave and composite material devices. He is author of more than 20 papers in international journals and conference proceedings, co-author of a book and 1 patent.

Appendix 1

(Italiano)

1. Verifiche sperimentali aggiuntive sui NIC prototipali

Le necessarie verifiche aggiuntive sono state sostenute per individuare e cercare di eliminare le cause che alimentano il fenomeno dell'auto-oscillazione, fenomeno che si genera nei dispositivi attivi BJT del circuito.

In questa fase del progetto si è cercato di ottenere sia il corretto dimensionamento dei valori nominali associati ai componenti SMD impiegati per la polarizzazione dei dispositivi attivi, sia una compensazione di tipo sperimentale sulle componenti parassite associate al PCB. Questa attività è stata suggerita e motivata dopo aver osservato i risultati ottenuti a valle di una serie di analisi effettuate sul modello circuitale ADS del circuito NCI prototipale.

Più precisamente, inserendo sul modello ADS i possibili elementi parassiti - ipotizzati e supportati da alcune prove sperimentali dedicate effettuate sui primi due prototipi - è stato possibile riprodurre il comportamento anomalo ti tipo oscillante a centro banda, inizialmente non previsto nel modello simulativo iniziale (Figura 1).

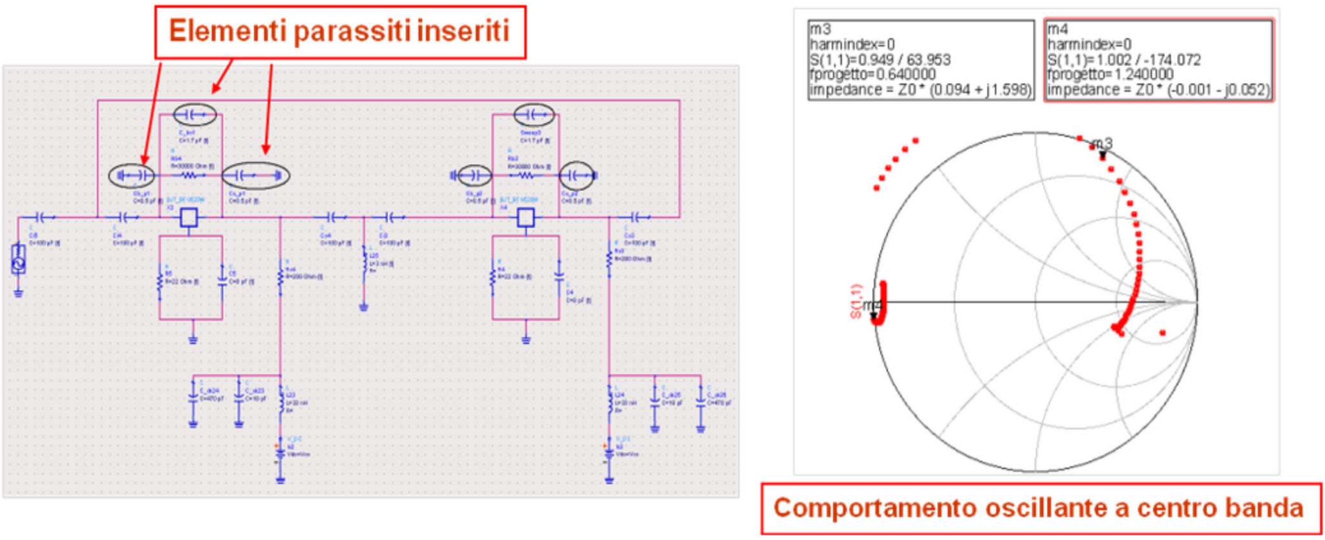

(*a*)

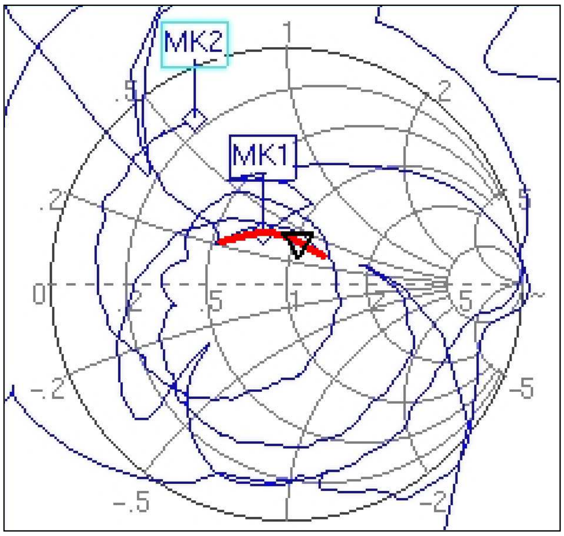

Caratterizzazione Prototipo: Comportamento oscillante a centro banda

(*b*)

Figura 1: (*a*) Modello circuitale con componenti parassite; (*b*) Misure $S_{11}(f)$ prototipo

Dal modello di simulazione numerica, comprensivo di parassiti e realizzato con ADS, si cercato di analizzare il malfunzionamento sul modello e di trovare una soluzione implementativa semplice per compensarlo, cercando di eliminare l'innesco delle auto-oscillazioni nei due dispositivi attivi, agendo anche sulla polarizzazione dei dispositivi attivi inizialmente prescelta.

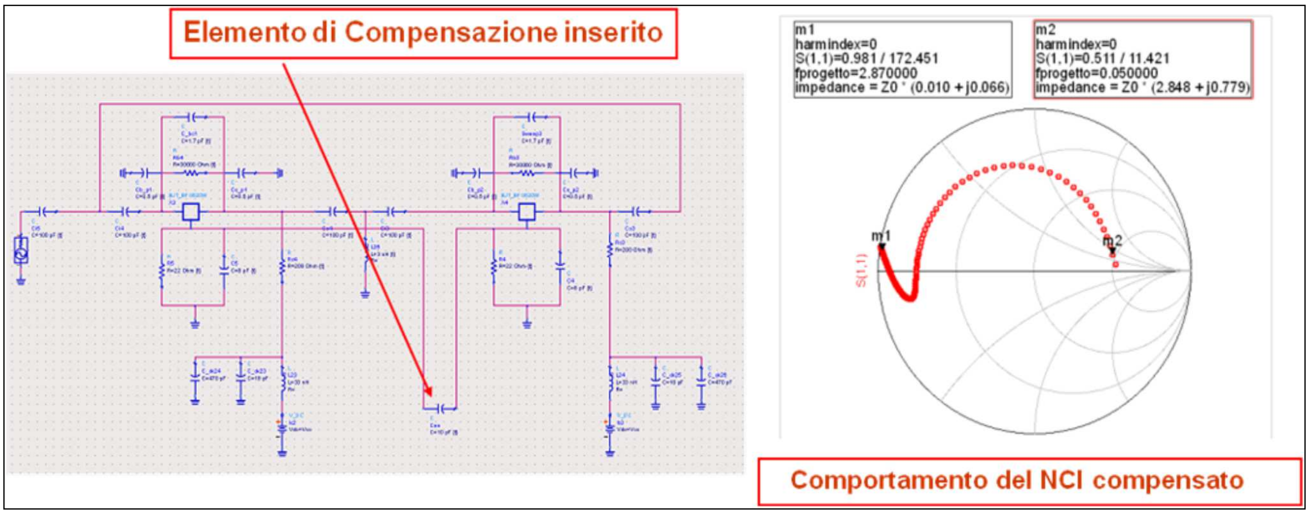

Figura 2: Modello circuitale con componenti parassite e capacità di compensazione

Con riferimento alla Figura 2 introducendo un componente capacitivo di compensazione (valore nominale di $C_{ee} = 10\ pF$ tra i due emettitori dei BJT), si è giunti ad osservare che tale componente consente di eliminare il malfunzionamento presente a centro banda e permette di riottenere sulla carta di Smith, il comportamento tipico dell'$S_{11}(f)$ in frequenza di un dispositivo NCI.

Considerando ora la soluzione PCB stampata riportata in Figura 3, realizzata per implementare e compattare le dimensioni dell'HW associate allo schema circuitale NCI prescelto.

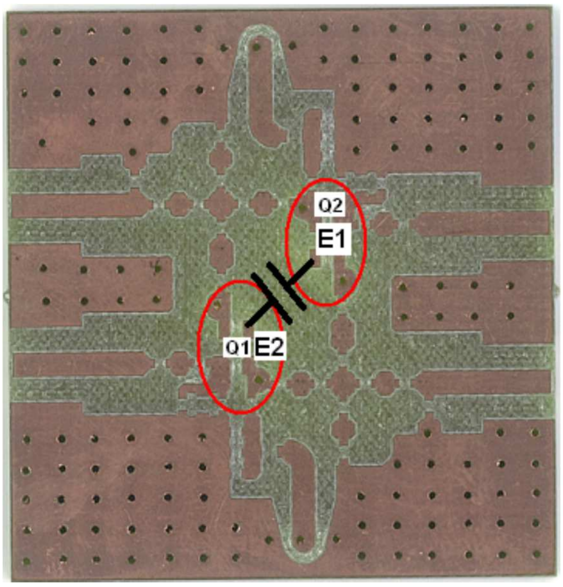

Figura 3: Modello circuitale con componenti parassite e capacità di compensazione

Come possiamo osservare tale soluzione non permette l'integrazione del componente SMD aggiuntivo C_{ee}. Infatti, la posizione assoluta tra le due piazzole indicate con E1 ed E2 (rispettivamente Emettitore del BJT Q1 e Q2) non consente una saldatura diretta del componente SMD a SOT standard prescelto a causa dell'eccessiva distanza lineare che c'è tra le due piazzole.

Si è dunque considerata la soluzione dell'integrazione a componente classico discreto a reofori, ovvero l'uso di un condensatore a tecnologia ceramica.

Tali condensatori sono realizzati con reofori filari sufficientemente lunghi e quindi tali da consentire una saldatura a stagno diretta sulle piazzole E1 ed E2. Il condensatore ceramico saldato e adattato sul circuito in oggetto, introdurrà inevitabilmente sia componenti parassite induttive dovute alla lunghezza eccessiva del reoforo, sia componenti capacitive intrinseche che non possono essere considerate trascurabili.

Per le prove sperimentali è stato dunque selezionato un set di possibili valori nominali capacitivi necessario per l'individuazione della corretta scelta della capacità C_{ee} di retroazione. Il valore nominale minimo preso in considerazione è di 2.2 *pF*, quello massimo di 47 *pF* (Figura 4).

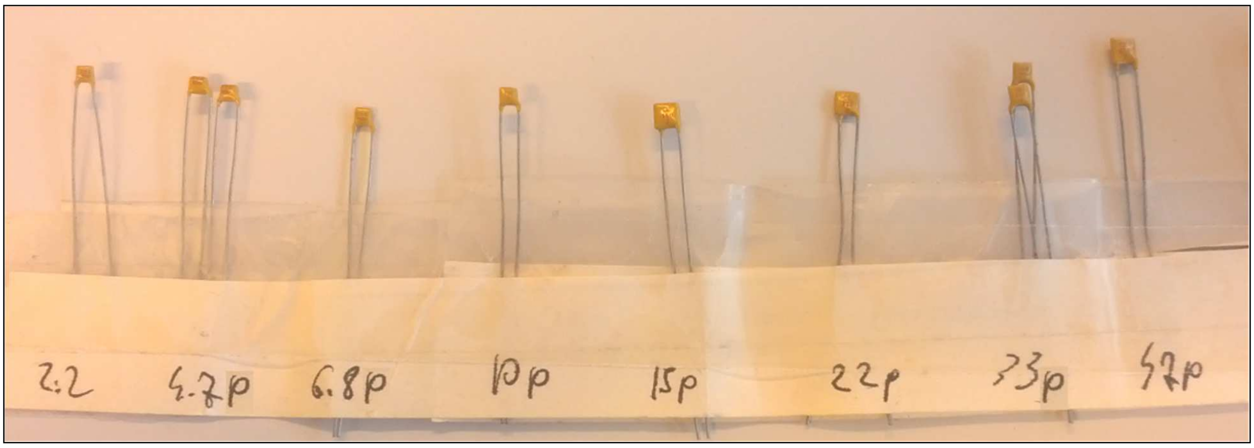

Figura 4: Valori nominali capacitivi prescelti per l’analisi sperimentale di compensazione componenti parassite

Nella Figura 5 è riportato il circuito NCI modificato in presenza del condensatore C_{ee} integrato e saldato sulle piazzole E1 ed E2 dei due BJT.

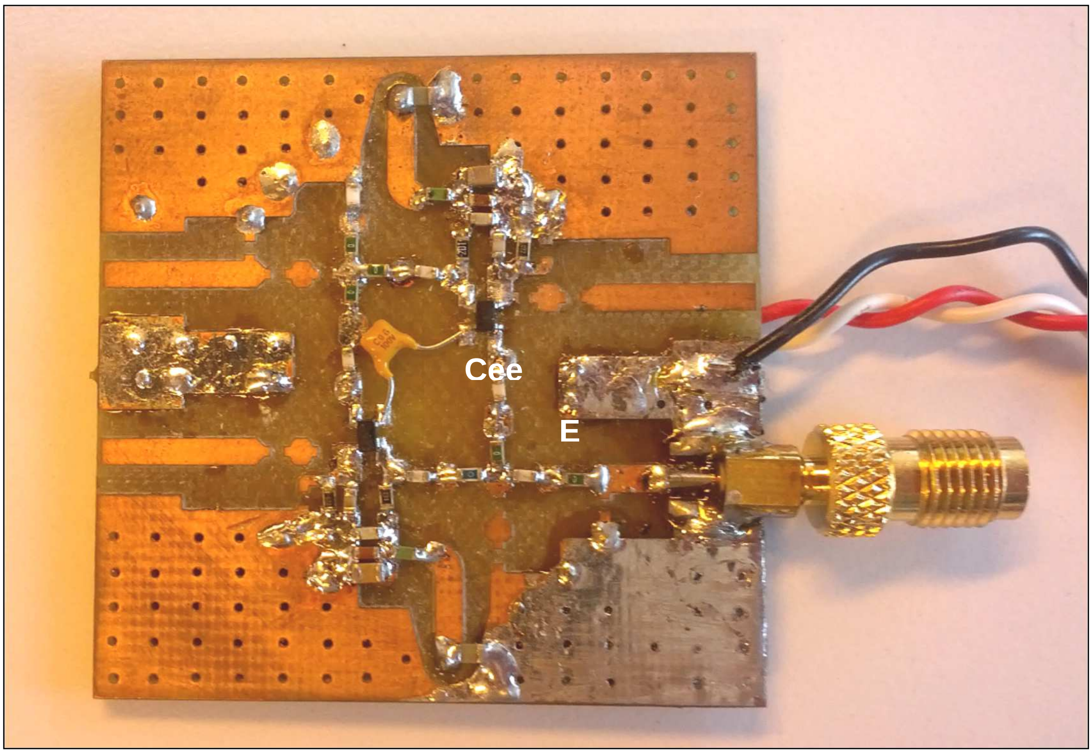

Figura 5: NCI modificato in presenza del condensatore C_{ee}

Sono state quindi eseguite delle attività di caratterizzazione in termini di return loss $S_{11}(f, C_{ee})$ al variare sia della capacità C_{ee}, sia del punto di lavoro dei dispositivi attivi.

Analizzando i dati ottenuti dalle caratterizzazioni, si è ritrovato che la miglior condizione in termini di stabilità si ottiene inserendo un C_{ee} il cui valore nominale compreso tra i 10 ed i 22 *pF*, ovvero un valore nominale convergente con quello stimato dal modello circuitale.

Gli andamenti sulla carta di Smith delle curve in frequenza ottenuti dalle caratterizzazioni sperimentali sul coefficiente di riflessione, non presentano ancora un'appropriata convergenza se confrontati con i risultati attesi dal modello simulativo circuitale ADS.

L'ipotesi ad oggi avanzata è che il modello circuitale ADS presenta comunque dei limiti e non risulta sufficientemente robusto ed accurato per poter individuare e quantificare tutte le componenti parassite associate alla soluzione prototipale realizzata.

2. Finalizzazione di un efficace ed efficiente modello simulativo full-wave non lineare

Considerando i risultati sperimentali ottenuti e le relative conclusioni riportate nel precedente paragrafo, l'attività in oggetto si è anche focalizzata nella ricerca di un efficace ed efficiente modello simulativo full-wave non lineare, in grado d'individuare e quantificare le componenti parassite intrinseche e/o distribuite associate alla soluzione circuitale definitiva.

In sintesi, con il circuitale ADS, si è stati in grado di analizzare in tempi rapidi

- fattibilità della soluzione circuitale prescelta,
- unbalance prestazionale in funzione della tolleranza percentuale dei componenti SMD,

Il modello si è dimostrato inadeguato, mostrando la non convergenza tra risultati simulati e dati sperimentali, soprattutto nel caso in cui le componenti parassite non sono tutte individuate e correttamente dimensionate.

Con il modello ADS è stato comunque possibile introdurre e dimensionare il corretto valore nominale della capacità Cee , ovvero gestire il problema della stabilità del dispositivo.

CST MWS nel dominio del tempo è sicuramente il modello più efficace, in quanto:

- CST MWS è un risolutore numerico 3D full-wave e quindi per definizione considera nel modello CAD-EM tutte le componenti parassite e non;
- l’interfaccia CAD-3D facilita la realizzazione e la generazione dei file CAD per la costruzione del PCB.

Le criticità sono associate principalmente ai tempi di calcolo richiesti, troppo onerosi per fornire i risultati con un solo “single run” di simulazione. Non risulta quindi uno strumento efficiente per l’analisi parametrica/ottimizzazione dei valori SMD nominali utilizzati (problema delle tolleranze dei componenti).

La ricerca di un modello simulativo alternativo più efficiente ed efficace per il NCI in oggetto si è dunque focalizzata su un simulatore dedicato per strutture PCB planari, e ad oggi è un attività ancora aperta.

3. Varianti previste sul PCB per essere sviluppato su singolo strato

Per questa attività si è cercato prima di tutto di realizzare lo schema circuitale del NCI in oggetto in tecnologia PCB singolo strato per minimizzare le componenti parassite.

La scelta del singolo strato ci permette di eliminare i due collegamenti elettrici “critici” presenti tra i due layer della soluzione PCB prototipale in prossimità del collettore e della base dei due transistor (ovvero i quattro vias indicati nelle zone cerchiate rosse di Figura 5). In questa porzione del PCB sono state ipotizzate e localizzate le componenti parassite sul segnale RF responsabili della non corretta convergenza del modello circuitale.

Questa attività ha generato un differente layout che varrà impiegato per la realizzazione di una seconda soluzione HW NCI più compatta e caratterizzata dal minimo impiego di componenti spare (inizialmente inseriti per la verifiche sperimentali). L’obbiettivo è quello di ridurre al minimo il numero di componenti e l’ingombro geometrico.

Nella Figura 6 è riporta l’immagine della nuova soluzione PCB proposta per il prototipo

NCI definitivo.

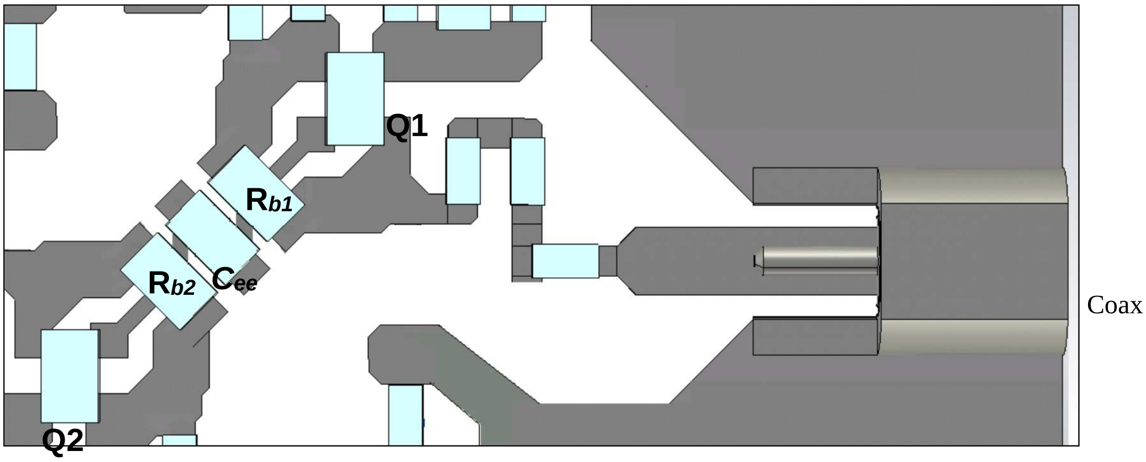

Figura 6: Soluzione CAD per il NCI modificato su laminato singolo strato

Nell’immagine è evidenziata la soluzione di sbroglio adottata in corrispondenza della zona critica. L’inserimento delle resistenze Rb1 ed Rb2 sul lato TOP del PCB sopporta la realizzazione dello soluzione NCI inizialmente proposta su un singolo strato del supporto dielettrico.

In pratica il collegamento tra le resistenze di collettore e base dei transistor non è più eseguito tramite il passaggio di vias metallizzati.

Come anticipato in precedenza lo schema elettrico definitivo è stato semplificato per integrare il minimo numero di componentistica SMD. Sono state quindi eliminate alcune componenti di by-pass, mentre è stata data la possibilità di inserire il controllo in tensione sui valori nominali associati alle capacità C_1 e C_3 mediante dispositivi varicap (Figura 7).

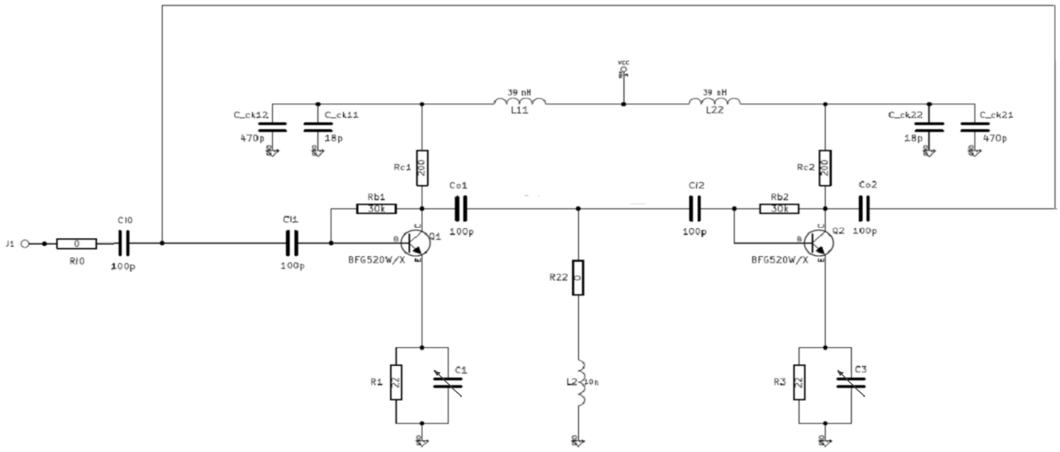

Figura 7: Schema circuitale NCI su laminato singolo strato

I risultati ottenuti dimostrano che circuiti attivi di tipo non-Foster possono essere utilizzati con successo per superare il funzionamento a banda stretta di un elemento radiante, che è una delle principali limitazioni dei componenti elettricamente corti. La soluzione NIC su PCB singolo strato proposta può essere dunque una compatta soluzione a basso costo e ad alta integrazione facilmente integrabile su un elemento radiante stampato di tipo SRR.

4. Analisi di possibili soluzioni circuitali NIC alternative ed eventuale realizzazione

L’attività inerente la ricerca di possibili soluzioni alternative circuitali NIC è stata focalizzata alla possibilità di realizzare il circuito mediante un dispositivo integrato compatto, in grado di integrare due Amplificatori Operazionali (A.O.)

La realizzazione mediante A.O. è in effetti quella più affidabile da realizzare anche se non è quella più conveniente in termini di costi. Supponendo che l’operazionale sia ideale, la classica configurazione invertente (Figura 8) può essere considerata NIC resisitivo, la cui impedenza d’ingresso vista dal generatore risulta:

$$R = \frac{v_s}{i_s} = -R_3 \cdot \frac{R_2}{R_1}$$

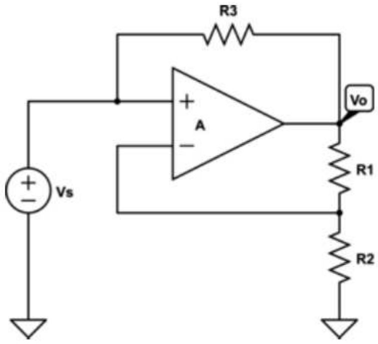

Figura 8: NCI ad A.O. in configurazione invertente

In letteratura sono presenti delle applicazioni in cui risulta molto utile la realizzazione di un dispositivo NIC di tipo *floating*, detto anche *FNIC*, in quanto è possibile realizzare dei collegamenti di carico di tipo serie. La Figura 9 ci mostra come implementare un *FNIC* utilizzando due A.O.

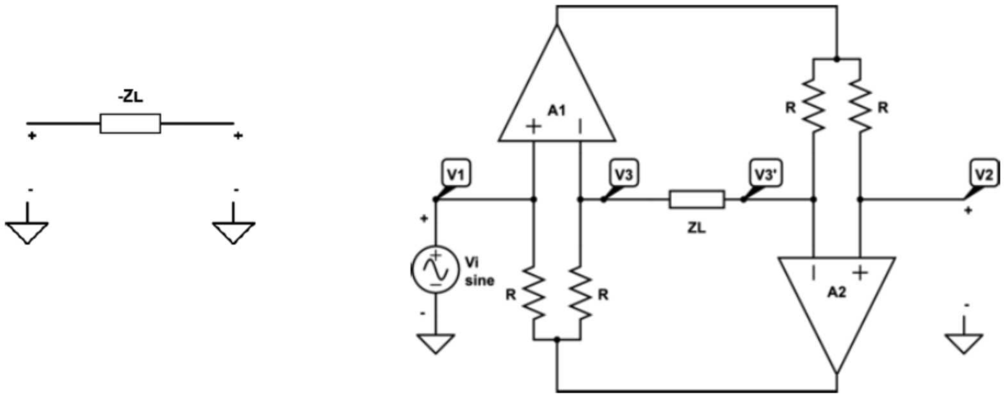

Figura 9: FNIC ad A.O. in configurazione floating

Dove, se poniamo l'uscita v2 aperta, l'impedenza vista dal generatore si dimostra essere idealmente nulla perchè su Z_L non può circolare corrente (v3=v3') .

Per implementare la soluzione *FNIC* è stato individuato il seguente dispositivo **dell'ANALOG DEVICE: ADA4817-2**. E' un dispositivo a basso costo che integra, su un singolo case a 16 pin, due operazionali ad alto slow rate con guadagno ad anello aperto unitario su una banda di circa 1 *GHz*. Di seguito un estratto dal DS del dispositivo

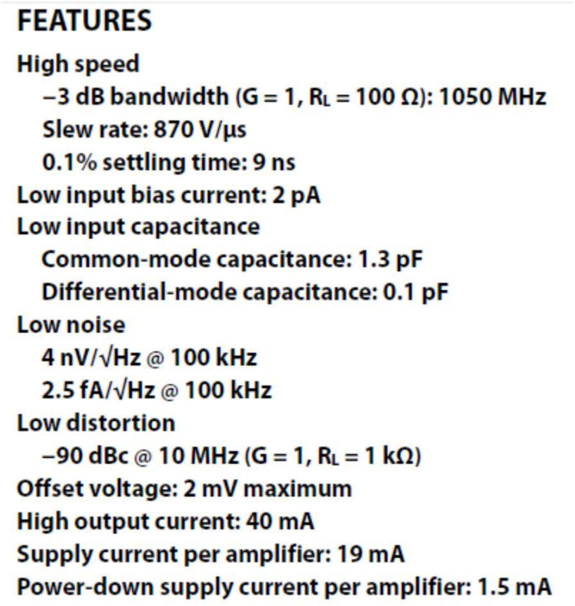

FEATURES

- **High speed**
  - **−3 dB bandwidth (G = 1, R_L = 100 Ω): 1050 MHz**
  - **Slew rate: 870 V/μs**
  - **0.1% settling time: 9 ns**
- **Low input bias current: 2 pA**
- **Low input capacitance**
  - **Common-mode capacitance: 1.3 pF**
  - **Differential-mode capacitance: 0.1 pF**
- **Low noise**
  - **4 nV/√Hz @ 100 kHz**
  - **2.5 fA/√Hz @ 100 kHz**
- **Low distortion**
  - **−90 dBc @ 10 MHz (G = 1, R_L = 1 kΩ)**
- **Offset voltage: 2 mV maximum**
- **High output current: 40 mA**
- **Supply current per amplifier: 19 mA**
- **Power-down supply current per amplifier: 1.5 mA**

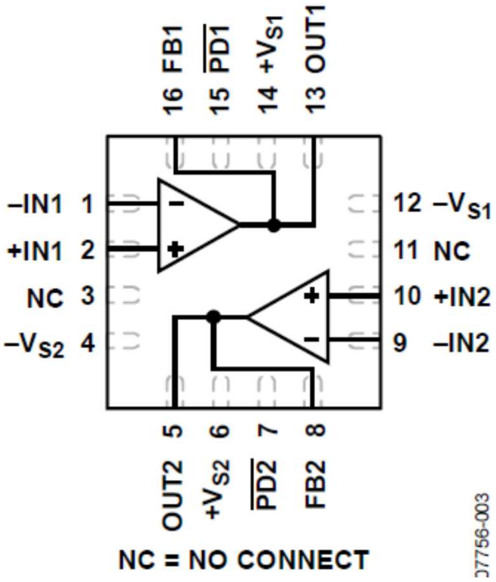

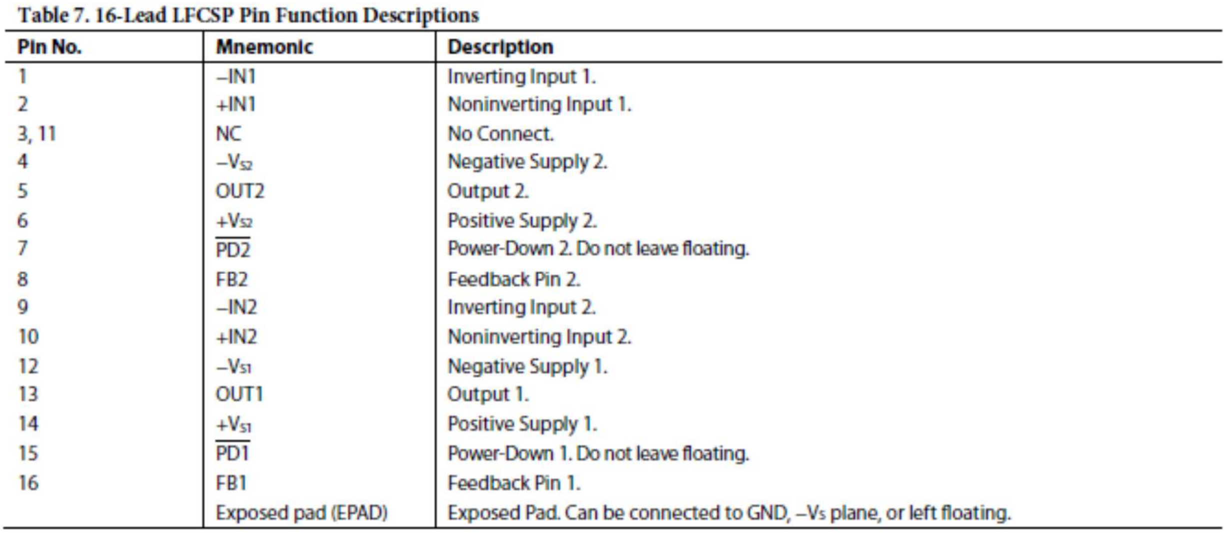
Table 7. 16-Lead LFCSP Pin Function Descriptions

Pin No.	Mnemonic	Description
1	–IN1	Inverting Input 1.
2	+IN1	Noninverting Input 1.
3, 11	NC	No Connect.
4	–V_{S2}	Negative Supply 2.
5	OUT2	Output 2.
6	+V_{S2}	Positive Supply 2.
7	$\overline{PD2}$	Power-Down 2. Do not leave floating.
8	FB2	Feedback Pin 2.
9	–IN2	Inverting Input 2.
10	+IN2	Noninverting Input 2.
12	–V_{S1}	Negative Supply 1.
13	OUT1	Output 1.
14	+V_{S1}	Positive Supply 1.
15	$\overline{PD1}$	Power-Down 1. Do not leave floating.
16	FB1	Feedback Pin 1.
	Exposed pad (EPAD)	Exposed Pad. Can be connected to GND, –V_S plane, or left floating.

Figura 10: Doppio A.O. dell’Analog Device per la realizzazione dell’FNIC

In generale, amplificatori operazionali ad alta velocità presentano la criticità nel pilotare carichi capacitivi. Questo è particolarmente vero se il guadagno ad anello chiuso è prossimo all’unità (dove il margine di fase è più basso).

La difficoltà nasce dal fatto che la capacità di carico C_L forma un polo con la resistenza di uscita, *Ro*, dell'amplificatore operazionale. Il polo introdotto può essere descritto dalla seguente equazione:

$$f_P = \frac{1}{2\pi R_O C_L}$$

Se questo polo risulta troppo vicino al punto di crossover a guadagno unitario, il margine di fase degrada. Come suggerito dal fornitore, se la capacità di carico è elevata è necessario utilizzare un resistore (RSNUB) all'uscita dell'amplificatore, come mostrato in Figura 11.

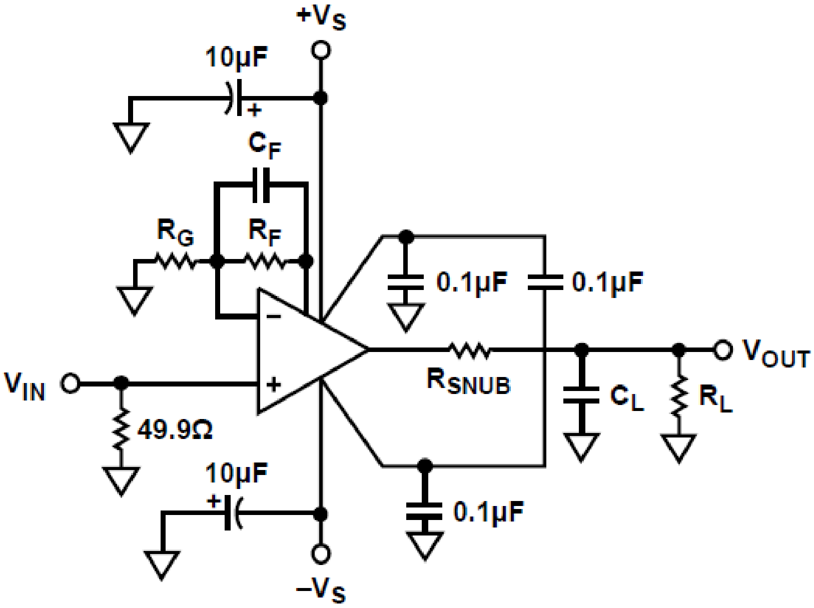

Figura 11: Doppio A.O. dell'Analog Device per la realizzazione dell'FNIC

Aggiungendo la piccola resistenza serie RSNUB, si crea uno zero che annulla il polo introdotto dal carico capacitivo. Valori tipici per RSNUB può variare da 10 Ω a 50 Ω.

La Figura 11 mostra anche un altro modo per ridurre l'effetto del polo creato dal carico capacitivo, ovvero posizionando un condensatore C_F nel circuito di retroazione parallelo al resistore di retroazione. Valori tipici condensatore possono variare da 0,5 a 2 *pF*.

Notiamo quindi che anche per la soluzione alternativa proposta ad operazionali doppi, il circuito di polarizzazione può risultare più complesso di quello a NIC realizzato.